Investigation and improvement of the performance of THz Coherent Undulator Radiation source driven by a photocathode RF gun

Siriwan Krainara

Abstract

The terahertz (THz) region of the electromagnetic spectrum is a rich zone for various fields of research and industrial applications. Several types of efficient THz radiation sources have been developed to fulfill specific requirements. At the Institute of Advanced Energy, Kyoto University, a THz Coherent Undulator Radiation (THz-CUR) source is driven by a compact accelerator using a photocathode radio-frequency (RF) gun, which generates an electron beam with a fixed energy of 4.6 MeV and a bunch charge higher than 100 pC. For the generation of high-intensity THz-CUR, an electron bunch is compressed to less than the radiation wavelength by means of passing it through a chicane magnet before going through an undulator. The main purpose of the development of the THz-CUR source is to generate intense quasi-monochromatic and tunable THz-CUR in the low-frequency region (< 1 THz). This region particularly draws attention to the study of the vibrational or rotational modes of the molecules for materials science. In 2016, the first commissioning successfully generated quasi-monochromatic THz-CUR; however, some of the important properties of THz-CUR were not measured. The impact of the quality of the electron beam on THz-CUR generation had also never been studied in the high bunch charge region. In consequence, the work in this thesis was conducted to investigate the properties of THz-CUR, to study the effects on the generation of radiation, and to present a potential method for improving the performance of the THz-CUR source.

Several experiments were conducted to measure the total radiation energy, spatial distribution, peak power, and power spectrum as functions of the bunch charge and the magnetic field of the undulator. The total radiation energy and peak power in a micro-pulse of THz-CUR reached ~1 μJ and 20 kW, respectively, with a bunch charge of 160 pC at 0.16 THz. At a bunch charge of 60 pC, the frequency could be varied from 0.16 to 0.65 THz by controlling the undulator field. We also found the limitations on the generation of THz-CUR from our source: saturation of the radiation energy occurred, and the radiation power spectrum at a frequency of 0.65 THz could not be observed at a bunch charge of 160 pC. Due to the low beam energy and the high bunch charge, the space-charge effect strongly occurs and causes degradation of the electron beam quality. We then studied the space-charge effect on the degradation of the quality of the electron beam, which affects to the generation of THz radiation. This study provides a better understanding of the behavior of the electron beam,

which can play an important role in enhancing the power of the THz-CUR. As a result of the study, it was found that the impact of the electron beam quality on the enhancement of THz-CUR power depended not only on the bunch length but also on the energy spread and emittance. That is, for high-quality electron beam at a bunch charge of 160 pC, the peak radiation power could be increased to more than 100 kW at a radiation frequency of 0.16 THz.

In order to mitigate the space-charge effect and improve the quality of the electron beam, manipulation of the transverse/longitudinal laser distribution was proposed. The laser transverse profile was changed from Gaussian to truncated-Gaussian profile by clipping using an aperture before illuminating the cathode. As for the longitudinal laser distribution, laser pulse was shaped as a flat-top beam and the pulse width was enlarged by using laser pulse stacking. The electron bunch length and the total energy of THz-CUR were examined under different conditions of the laser's shape. The effectiveness of bunch compression in obtaining a short bunch length suggested that the manipulation of transverse/longitudinal laser distribution allows us to decrease the space-charge force in an electron bunch. Under the present conditions of our source, the use of a 10 ps full-width at half-maximum (FWHM) flat-top laser pulse with truncated-Gaussian transverse profile would be a good candidate for improving the source performance.

For the THz-CUR propagation from the THz window to the user station, the transport beamline must be carefully designed because the emitted THz-CUR in the low-frequency region propagates with a large amount of diffraction. Using the optical design reported in this thesis, the simulated result of the intensity transmission ratio was higher than 60% over the whole frequency range of the THz-CUR generated from our source.

Acknowledgements

Foremost, I would like to sincerely express my deepest gratitude to my supervisor, Professor Hideaki Ohgaki for giving me the opportunity to study at Kyoto University and to work under his supervision. I would like to take this opportunity to thank for his guidance and support. I have learned many things from his professional experience. His critical comment and valuable suggestion lead me to improve and to complete my work. This thesis would not have been possible without the encouragement, kindness, and support from him.

I am sincerely indebted to Assistant Professor Heishun Zen, who has been always willing to answer, to discuss, and to help any technical problems associated with experiment, calculation, and simulation. I have an indefinite appreciation for his guidance throughout this work. He taught me a lot about the experiment and data analysis. During the experiment, he gave me a lot of suggestions and spent his lengthy valuable time for helping me.

I would like to thank Associate Professor Toshiteru Kii for his help, the support of the computer program, and always giving me useful comment and suggestion during our group meeting.

I would like to thank Prof. Kazunari Matsuda and Prof. Yasuyuki Shirai for the meaningful discussion, comments, and suggestions.

The work in this thesis would never have been possible without the financial support from the Ministry of Education, Culture, Sports, Science, and Technology in Japan (MEXT), for which I am extremely grateful.

I would like to express special gratitude to the secretary, Ms. Yumiko Nagaya for her help and excellent administrative assistance since the beginning of my study at Kyoto University.

I would like to give a special thank Dr. Sikharin Suphakul for teaching me to the basic in running GPT simulation and THz-CUR source. I would like to give a big thank Dr. Watcharkorn Ketren for providing me the helps and encouragement.

I am very thankful Mr. Chatani Shuya for the contribution and discussion on the system of laser pulse stacking.

I am grateful to my friends whom I met in Ohgaki-lab and in Japan for their help and being good friends during my study.

Additionally, I would like to thank all of my friends in Thailand and my colleagues at Synchrotron Light Research Institute for all their supports.

I do not know how to thank, my life partner, Mr. Sudjakom Jummun and his family for always encouraging me, supporting me, listening to me, and being beside me throughout the happy and hard times. I love and appreciate very much.

Last but not least, I want to send the biggest gratitude to my family, my father Anaek, my mother Phonthip, two sisters, and nephew-nieces who stand behind and motivate me. They always support me spiritually throughout my life.

Contents

List of Figures

List of Tables

Chapter 1

Introduction

1.1 Motivation

Recently, thanks to the rapid evolution of ultrashort pulse laser technology based on solid-state lasers, intense THz pulses are now widely available [1, 2]. As a consequence, research undertaken to study nonlinear phenomena driven by the intense THz pulse has rapidly evolved [3]. Initially, the rectification of ultrashort near-infrared laser pulses can generate the wideband THz pulses. However, in order to allow studying more detailed information of nonlinear phenomena, a narrowband intense THz pulse is more suitable than wideband one because it provides a sharp resonance at a certain frequency. Moreover, a high THz radiation power in a narrow-bandwidth is preferable than a broadband pulse for some applications such as THz irradiation [4], and pump-probe spectroscopy [5, 6]. That the reason why the narrowband THz sources based on the ultrashort-pulse near-infrared lasers have been developed promptly [7]. On the other hand, the accelerator-based THz sources such as Free Electron Lasers (FELs) [8] are also good candidates to be used for nonlinear THz spectroscopy. Nowadays, coherent radiations generated from an ultrashort high-energy electron bunch draw attention to generate intense THz pulses via coherent undulator radiation (CUR) source and superradiance THz FELs [9, 10]. They can possibly generate megawatt (MW)-class THz pulses, continuously tuned wavelength, and narrow-bandwidth. However,

the lacks of FEL facilities are to require a large space and high cost for construction and operation. Therefore, a small-scale accelerator for THz radiation generation has been proposed.

At the Institute of Advanced Energy (IAE), Kyoto University, a compact accelerator-based THz-CUR source has been developed to provide intense quasi-monochromatic THz pulse, which covers the frequency range lower than 1 THz [11]. The intensity of the coherent radiation increases with the square of the number of radiating electrons per bunch, N^2 when an electron bunch length is shorter than the radiation wavelength. The photocathode RF gun used as an electron source can generate a bunch charge up to 1 nC with the electron beam energy of 4.6 MeV [12]. According to the low-energy source and high charge, the electron beam is easily perturbed by the space-charge force in a short electron bunch. It causes to degrade the electron beam qualities, e.g., bunch lengthening, energy spread, and emittance growth. This would result in the limitation of THz-CUR generation. Regarding the mitigation of the space-charge force, the increase of electron beam energy is one of a potential way and be helpful to enhance the radiated power. However, our source has a limitation of RF power, and also the THz-CUR project is targeting a compact system, so using an additional acceleration tube cannot be an acceptable means of increasing the electron energy. Another potential method for mitigating the space-charge effect is to manipulate the transverse/longitudinal laser distribution. Since the source using a photocathode as an electron source, the properties of the generated electron beam relate to laser cathode excitation. Many studies [13-17] reported that the technique of shaping the laser distribution can also be used to reduce the space-charge effect. Therefore, to eliminate the problem addressed above, the impact of the drive laser pulse shape before illuminating the cathode on the mitigation of space-charge force is needed to be studied for improving the performance of our source. The degradation of electron beam qualities would be improved for achieving higher radiated power. In order to serve high power THz-CUR for the applications, the transport beamline has to be carefully designed to allow transferring the radiation with the high-intensity transmission ratio to the user station.

1.2 Background of THz radiation and its applications

Electromagnetic spectrum is composed of radio wave, microwave, infrared, visible light, ultraviolet, x-rays, and gamma-rays. The kinds of electromagnetic spectrum can be determined by wavelength, frequency, and energy. The part of the radiation spectrum sandwiched in between microwaves and an infrared light wave, is called the “terahertz gap” [1]. This gap falls the frequency of 0.1 - 10 THz region. The wavelength of terahertz radiation ranges from approximately 0.03 - 3 mm known as "sub-millimetre". THz radiation has good penetrability on a dielectric material and non-polar liquids such as clothing, paper, wood, plastic, and ceramics but cannot pass through water or metal material. Since Terahertz radiation has low photon energy and is non-ionized radiation, it is interesting instead of using x-rays to prevent a risk to living tissue [18]. The radiation in the THz region has great attention in the past two decades due to its unique characteristics and broad applications [19].

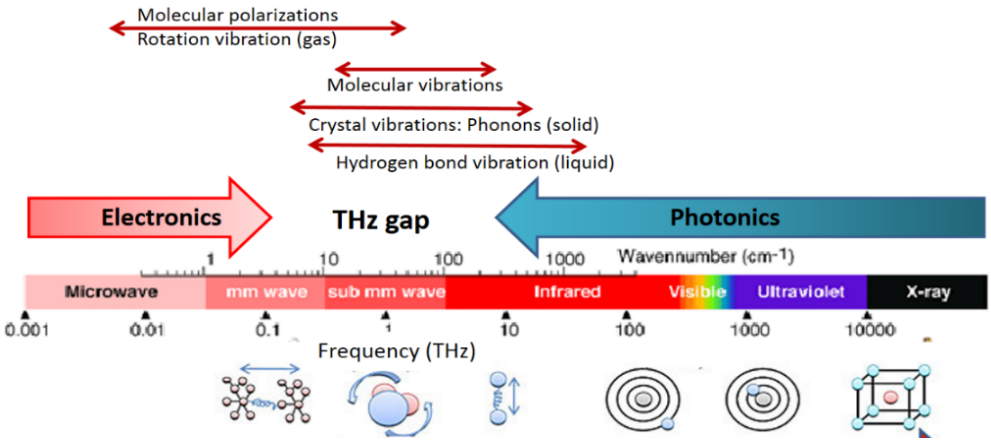

Figure 1.1: THz radiation characteristics.

THz technology can fulfill and be enormous attention to the requirements in a variety of fields [1] such as medical diagnostics, non-invasive imaging, material research, sensing, quality control, telecommunications, security, and basic science as summarized some examples in Fig. 1.2 [4, 42, 50-58]. Recently, applications in THz region can be largely categorized into three areas containing THz Imaging, THz spectroscopy, and THz Communication. THz imaging has drawn attention on industrial applications such as medical examination, discrimination drug, checking of hazardous materials and assay devices, and security scanning. Hence it is suitable for nondestructive and non-invasive inspection of THz imaging [20, 21]. Also, the terahertz radiation is an attractive zone for molecular

spectroscopy because it has the potential for exciting rotational and vibrational modes of the molecule and for observing the intermolecular vibrations in some chemicals and organic molecules. Consequently, it can be able to provide new information or methods of material analysis such as THz time-domain spectroscopy (THz-TDS) technique and pump-probe experiment [22, 23]. Regarding THz communication, the communication devices that operate in the THz frequency range can deliver the data with high-speed faster than those used in the frequency range of gigahertz [24, 25].

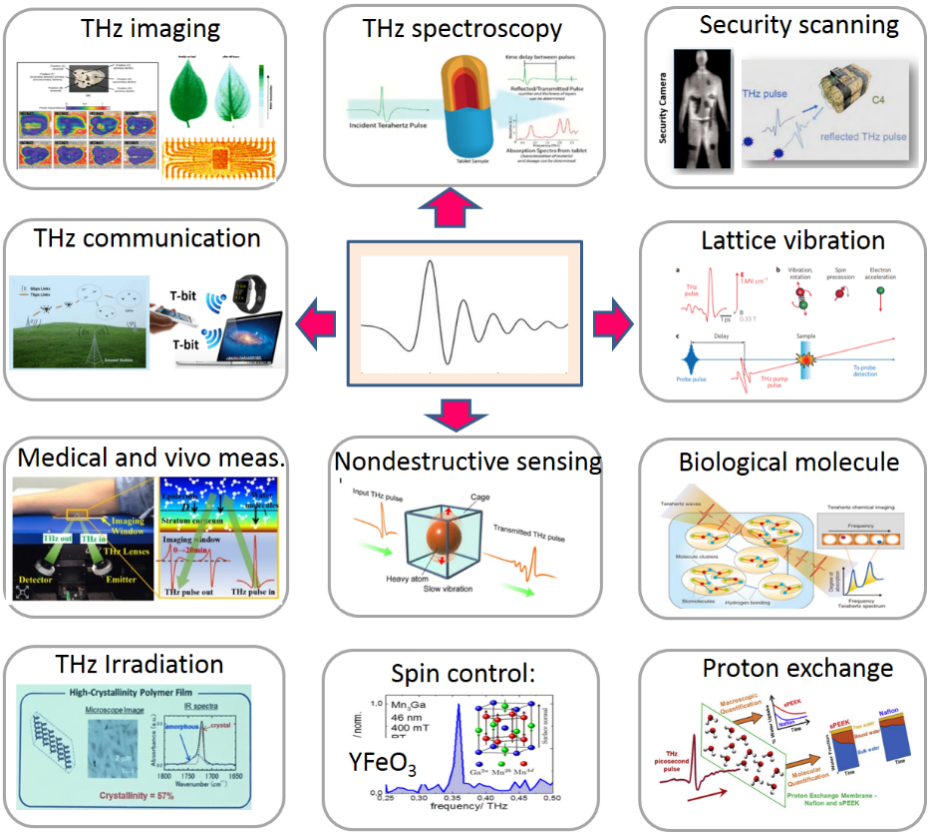

Figure 1.2: THz applications.

1.3 Review of the existing THz sources around the world

Several types of efficient THz sources in current use have been developed for supporting the applications mention above [26]. The sources to produce the radiation THz are summarized in Fig. 1.3 [27, 28], for example, Schottky diodes, IMPATT diode, InGaAs RTDs, BWOs, quantum cascade lasers, optically pumped solid state devices, and free electron devices (FELs). At present, most of the THz radiation sources are based on the nonlinear interaction of optical laser pulses with crystals. However, the disadvantages of the

method mentioned contain the low level of power generated and the limitation of the tunability of frequency or wavelength [8]. While FELs facilities are capable of providing high power and tunability THz radiation and also obtaining the polarization of THz radiation. According to the study of the dynamical processes by pump-probe techniques, the pulse length of FEL in the picosecond (ps) range is more suitable [29].

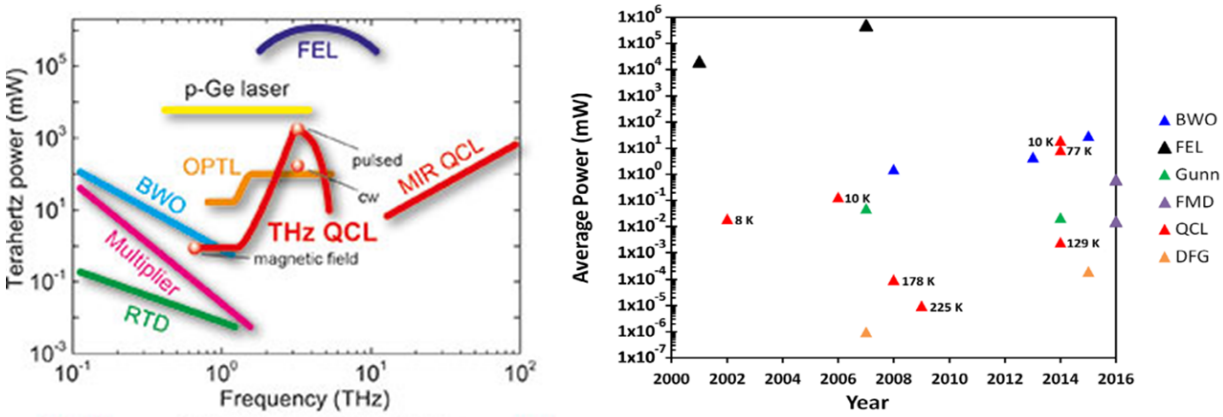

Figure 1.3: (left) available sources of high power THz radiation for different frequencies [25] and (right) the average power of the respective sources in the region between 1 - 5 THz [1].

Free-electron lasers (FELs)

In essence to produce THz radiation in FELs, there are many techniques of accelerator developed to produce the high power THz radiation when a relativistic electron beam passing through not only an undulator but also any structure [31-33], for example *Synchrotron radiation* (emission from electrons passing through a bending magnet), *Transition radiation* (emission from electrons crossing a non-uniform dielectric material), *Cerenkov effect* (emission from electron moving through a dielectric material), *Smith-Purcell effect* (emission by injecting electron beam close to an optical grating), and *bremsstrahlung* (radiation produced by deceleration of electrons). The most frequently used one is the magnetic undulator to generate *undulator radiation*, originally proposed under the condition of an electron bunch shorter than that of the radiation wavelength. These features make "Coherent Undulator Radiation" particularly interesting as a high power, tunable and narrow-bandwidth THz radiation source. The heart component of the FEL system is the undulator, which is produced by using either permanent magnets or electromagnets. The conversion of the electron beam energy into coherent electromagnetic radiation takes place in undulator. FELs can be operated as an oscillator, or as a seed FEL amplifier (Fig. 1.4).

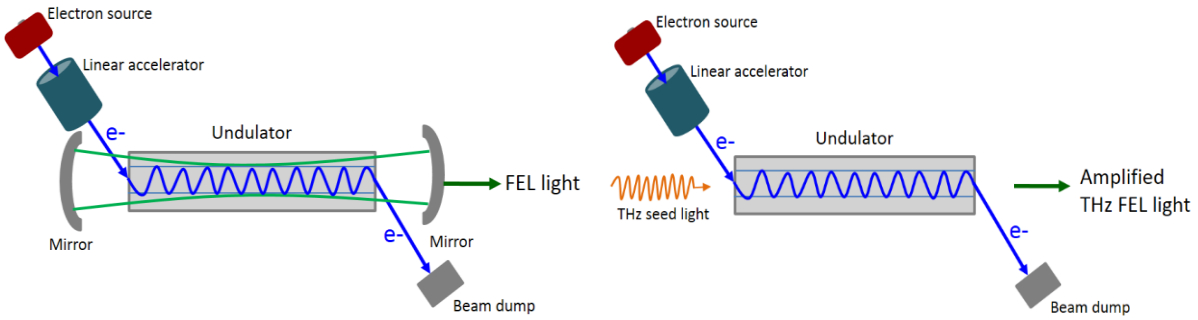

Figure 1.4: Schematic layout of (left) FEL oscillator and (right) seed THz FEL amplifier.

In undulator-based FEL, most of FEL-based THz sources are operated in oscillator mode, using an optical cavity to retain the radiation in the undulator device. When the FEL operated as an amplifier, the seed light must be provided for increasing the power in the THz region. The FEL-based THz source including a seed light is attractive to amplify THz radiation power. An injection seeded terahertz parametric generator (is-TPG) using LiNbO3 or MgO:LiNbO3 crystal is required to produce the seed light [30]. For the superradiant THz FEL source, the electrons can be emitted coherently in phase under the condition if the electron bunch is shorter than the radiation wavelength. Using this technique, the system does not require the input radiation or mirrors.

Regarding a high power THz radiation, FEL facilities-based THz sources, for example, for example, SLAC [34], ELBE [35], Novosibirsk THz FEL [36], AREAL, FLUTE [37] have been developed to meet the requirement in the infrared range, and to fulfill into the THz region. A challenge for this source is to reduce the size of FEL facility to a compact accelerator system. Nowadays, the compact accelerators have been developed in many facilities that have the ability of continuity tuning to the THz radiation regime. Their peculiar feature could possibly produce the THz radiation with the power in the megawatt (MW) region.

Compact accelerator-based THz radiation source using photocathode RF gun

The THz coherent radiation sources using photocathode RF guns have been developed and started running in some facilities, for example, Tsinghua University [38], NSRRC [39], PITZ [40], and SPARC-LAB [41]. Most of the coherent THz radiation sources mentioned concentrate on providing high power THz radiation in a frequency ranging from 0.5 to 5 THz.

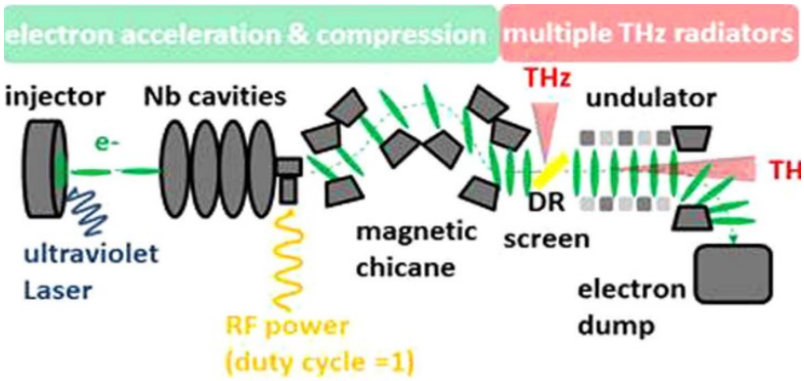

Figure 1.5: Schematic of superradiant THz sources at TELBE [10, 42].

As for frequencies lower than 0.5 THz (narrow-band THz radiation), the super-radiant undulator radiation source of TELBE in Fig. 1.5 [10, 42], has been developed operating with a high electron beam energy of 40 MeV. This source provides THz radiation (0.1–3 THz), with maximum radiation energy of 100 μJ and a high repetition rate in MHz. Another system is a high repetition rate THz source based on a 3.5-cell superconducting radio frequency (SRF) photo-injector at Peking University, which provides THz pulses (0.24–0.42 THz) with macro-pulse energy of 0.89 μJ [43]. In contrast to the systems described above for generating high power THz radiation, a compact system of low-energy source using only 1.6-cell photocathode RF gun can be arranged with no subsequent acceleration. Some proposals have been found in the literature [44, 45].

1.4 THz-CUR system at the Institute of Advanced Energy (IAE), Kyoto University

A compact accelerator source of 4.6 MeV electron energy has been developed since 2013 [46] for generating THz radiation. The first commissioning of a recently developed compact accelerator of THz-CUR source was completed for THz generation in 2016 [47]. In order to keep it compact and low in construction and operation costs, the system has no additional acceleration tube, and the electron beam energy is fixed at 4.6 MeV [48]. Figure 1.6 gives the overview of THz-CUR machine. Our THz source is a compact system with a total length of 3.7 meters. This system will be described in detail in the next Chapter. The aim is to produce intense quasi-monochromatic THz-CUR in the frequency range of 0.1 to 1 THz. This frequency range is attractive for the study of the lattice vibration of molecules for materials science or the precession of spin for the magnetic material. It is revered as a powerful tool to

control and improve the properties of materials such as biological or magnetic materials. The machine parameters of our source are listed in Table 1.1.

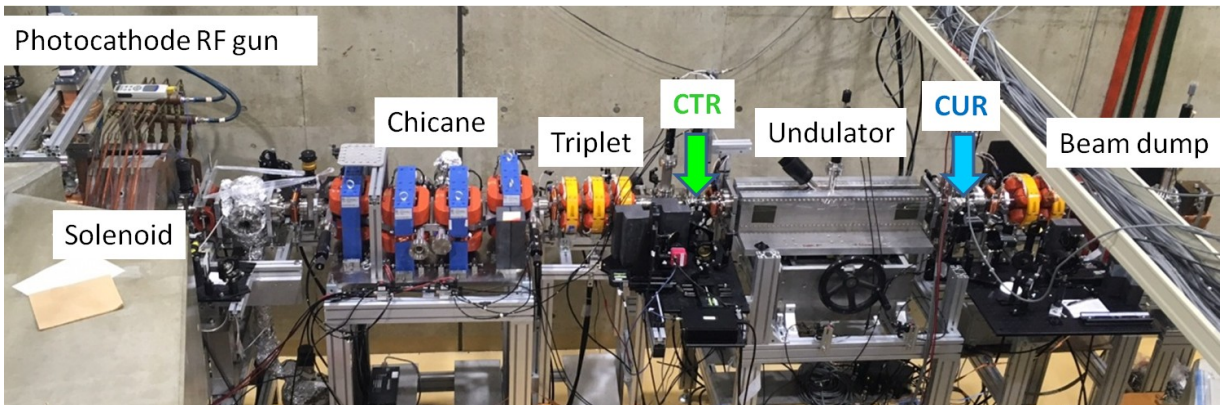

Figure 1.6: Actual machine of a compact accelerator based THz-CUR source at Kyoto University [48].

Table 1.1: Machine parameters of THz-CUR source at Kyoto University.

Parameters	Value
Laser cathode excitation	
Laser energy	< 200 μJ
Wavelength	266 nm
rms. laser size @cathode	0.5 mm
Laser pulse width	5.8 ps-FWHM
Longitudinal profile	Gaussian
Electron beam	
Beam energy	4.6 MeV
Energy spread	< 3 %
Normalized Emittance	5 mm-mrad
Bunch charge	< 200 pC
Undulator specification	
Max. magnetic field	0.43 Tesla
Number of period	10 periods
Period length	70 mm

The electrons were generated by injecting a UV laser with a wavelength of 266 nm to a cathode. The laser pulse duration was measured as 5.8 ± 0.2 ps in full-width at half-maximum (FWHM) with Gaussian distribution [49]. The transverse laser size at the cathode surface was measured as 0.5 mm in root-mean-square (rms) with Gaussian transverse distribution. An

electron bunch was compressed by a bunch compressor chicane before passing through a planar undulator. The electron beam with 4.6 MeV energy and the energy spread of 1.3% could be obtained by using the RF power of 9 MW and the laser pulse energy of 20 μJ for generation of a bunch charge of 50 pC [46]. Some numerical and experimental studies on the electron beam properties were carried out.

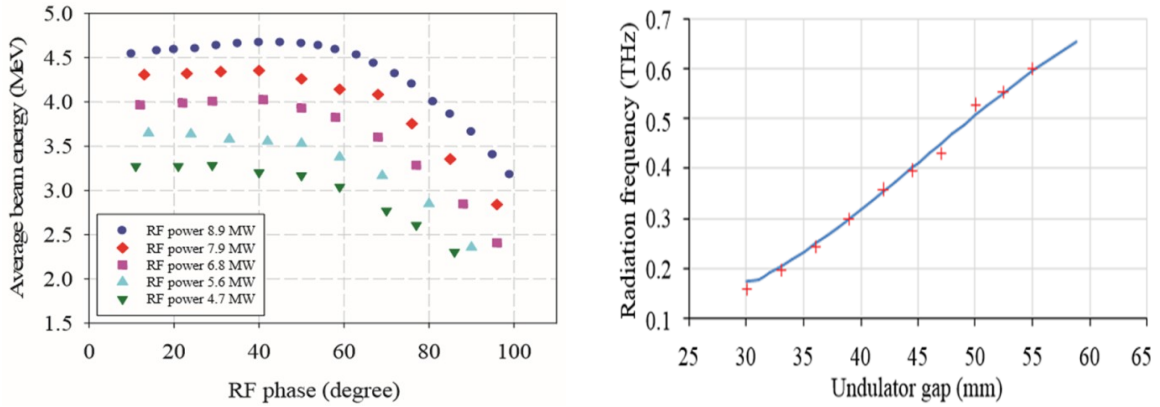

Figure 1.7: (left) Measurement results of the beam energy dependence on the RF powers and the RF phases [12] and (right) Central frequency of the CUR at different undulator gaps [47].

Figure 1.7(left) presents the investigation of electron beam energy by changing the driven RF power and the laser injection phase. The bunch charge had the maximum at 1.4 nC at a laser energy of 350 μJ. The beam emittance was measured by the quadrupole scan method at the bunch charge of 50 pC to be 5.0 and 7.5 mm-mrad in the horizontal and vertical direction, respectively. The estimated bunch length was less than 1 ps at the bunch charge of 50 pC. Due to the strong space-charge effect, the electron bunch with high charge could not be compressed enough by the magnetic chicane. It is needed more investigation for better understanding of the behavior of electron beam.

The study in [47] demonstrated that this system could generate radiation in a frequency range of 0.17–0.55 THz (Fig. 1.7(right)) with a bandwidth of approximately 10%, but the absolute value of the intensity was not measured. In order to study the radiation properties in more depth, the absolute or total radiation energy and the peak radiated power need to be measured and investigated.

1.5 Research objectives

In this thesis, the characteristics of THz-CUR at Kyoto University were investigated, and the mitigation of the space-charge effect in low energy electron bunch was studied in order to improve the performance of THz-CUR source. The main goals of this research are as follows:

1. To investigate the characteristics of THz-CUR at Kyoto University.
2. To study a potential method for optimizing the beam dynamics and for better understanding the behavior of electron beam disturbed by the space-charge effect.
3. To improve the performance of THz-CUR source by mitigating the space-charge force in an electron bunch.
4. To design the THz transport line for the applications.

1.6 Summary of the thesis

According to the research objectives mentioned above, this thesis is devoted to improving the performance of THz-CUR source for user applications.

Chapter 1 gives the introduction of THz radiation and **Chapter 2** describes THz-CUR source at Kyoto University. The theories involved with the study in the thesis and the important components of THz-CUR are explained in detail.

Chapter 3: This chapter is devoted to presenting the experiments and the properties of THz-CUR including the total radiation energy, spatial distribution, and power spectrum. Based on the measured results, the limitation of the generation of THz-CUR from our source was encountered. Due to the influence of the space-charge forces causing the degradation of electron beam qualities, the saturation of the radiation energy occurred, and the radiation power spectrum at a 0.65 THz frequency could not be observed at the bunch charge of 160 pC. The effects of bunch lengthening, energy spread, and emittance growth and the influence of the phase error on the generation of THz radiation are also presented.

Chapter 4: According to the measurement, the THz-CUR energy obviously was saturated at the high bunch charge region. It may be caused by the influence of the space-charge force in a short electron bunch, which results in the degradation of the electron beam quality. For a better understanding of the behavior of the electron beam to improve the source performance further, the investigation of electron beam quality is needed. The electron beam properties

such as bunch length, beam size, and energy spread were measured as a function of bunch charge and compared with the simulation result.

Chapter 5: The method of manipulation of the transverse/longitudinal laser distribution is proposed to mitigate the space-charge effect for improving the performance of our THz-CUR source. The electron bunch can be effectively compressed with the chicane magnet when changing the transverse distribution from Gaussian to the truncated-Gaussian profile, and also enlarging the laser pulse width before illuminating a cathode. Thus, the bunch form factor can be increased.

Chapter 6: The examinations of the transverse truncated-Gaussian distribution, as well as the enlargement of the laser pulse width to generate the higher radiated power of THz-CUR, have been performed experimentally. This chapter reports the successful mitigation of the space-charge effect by using the truncated-Gaussian laser profile and enlarging the laser pulse width. However, the radiation power did not meet the value as expected. The limitations of transverse and longitudinal laser distribution in our source to improve electron beam quality are presented.

Chapter 7: In this chapter, the calculation result of THz radiation propagation to THz user station is presented. The total length of transport beam line from THz window to THz user station is about 18 meters. Since long wavelength has a large amount of diffraction, the beam propagating along beam line needs to be carefully designed to keep the beam size small for a high transmission ratio. According to the optical design reported in this chapter, the intensity of transmission would be obtained higher than 60% for the whole range of 0.16-0.65 THz frequency.

Chapter 8: This chapter presents the thesis conclusions with recommendations and contains the suggestions for future improvement of THz-CUR system at Kyoto University.

1.7 References

[1] S. S. Dhillon, *et al.*, "The 2017 terahertz science and technology roadmap", *J. Phys. D Appl. Phys.* **50**, 043001 (2017).

[2] K. Tanaka, *et al*., "Nagai, M. THz Nonlinear spectroscopy of solids", *IEEE Trans. Terahertz Sci. Technol.* **1**, pp. 301–312 (2011).

[3] K. Tanaka, *et al.*, "THz Nonlinear spectroscopy of solids", *IEEE Trans. Terahertz Sci. Technol* **1**, pp. 301–312 (2011).

[4] H. Hiromichi, *et al.,* "Polymer Morphological Change Induced by Terahertz Irradiation", *Sci Rep.* **6**, 27180 (2016).

[5] I. Lundholm, "Terahertz radiation as a pump and probe for studying low frequency vibrations in proteins", PhD thesis, University of Gothenburg (2015).

[6] M. B. Johnston, *et al*., "Pump-Probe Spectroscopy at Terahertz Frequencies", book: Terahertz Spectroscopy and Imaging, pp 251-271 (2012).

[7] H. Minamide, "Development of high-power terahertz-wave sources for finding novel applications", *IEEE Trans. Terahertz Sci. Technol.* 5, 1104–1109 (2015).

[8] T. Ping, *et al*., "Terahertz radiation sources based on free electron lasers and their applications", *Sci. China. Inf. Sci.* **55**, Issue 1 (2012).

[9] S. D. Mitri, *et al*., "Coherent THz Emission Enhanced by Coherent Synchrotron Radiation Wakefield", *Sci. Rep*. **8**, 11661 (2018).

[10] B. Green, *et al*., "High-Field High-Repetition-Rate Sources for the Coherent THz Control of Matter", *Sci. Rep*. **6**, 22256 (2016).

[11] S. Krainara, *et al*., "Properties of THz coherent undulator radiation generated from a compact accelerator source at Kyoto University", *Review of scientific instrument*: Publication after revision (2019).

[12] K. Damminsek, *et al*., Electron beam properties from a compact seeded terahertz FEL amplifier at Kyoto University, in *Proc. of* FEL, Daejeon, Korea, 23–28 August 2015, pp. 85–88 (2015).

[13] B. L. Beaudoin, *et al.*, "Longitudinal bunch shaping of picosecond high-charge MeV electron beams", *Phys. Plasmas* **23**, 103107 (2016).

[14] H. Kim, *et al*., "Longitudinal laser pulse shaping for low-emittance electron-beam generation", *J. Korean Phys. Soc.* **54**, pp. 381–385 (2009).

[15] J. Yang, *et al*., "Low-emittance electron-beam generation with laser pulse shaping in photocathode radio-frequency gun", *J. Appl. Phys.* **92**, 1608 (2002).

[16] F. Zhou, *et al.*, "Impact of the laser spatial distribution on the LCLS photocathode gun operation", *Phys. Rev. ST Accel. Beams* **15**, 090701 (2012).

[17] T. Miyajima, *et al.*, "Low emittance electron beam transportation in compact ERL injector", in *Proc. of* IPAC, Dresden, Germany, 15–20 June 2014, pp. 3104–3106 (2014).

[18] A. I. McIntosh, *et al.*, "Terahertz spectroscopy: a powerful new tool for the chemical sciences?", *Chem. Soc. Rev.* **41**, pp. 2072–2082 (2012).

[19] V. Sharma, *et al.*, "Terahertz Technology and Its Applications", IEEE International Conference on Advanced Computing & Communication Technologies (ICACCT), pp. 175–178 (2011).

[20] P. Garbacz, "Terahertz Imaging - Principles, Techniques, Benefits and Limitations", Maintenance problems **1-2016**, pp. 81-92, (2016).

[21] L. Yu, *et al.*, "The medical application of terahertz technology in non-invasive detection of cells and tissues: opportunities and challenges", *RSC Adv.* **9**, pp. 9354-9363 (2019).

[22] M. Theuer, "Terahertz Time-Domain Spectroscopy Systems for Fundamental and Industrial Applications", Cuvillier (2009).

[23] G. A. Blake, "Microwave and terahertz spectroscopy", Encyclopedia of Chemical Physics and Physical Chemistry: Fundamentals, 1063 (2000).

[24] M. J. Fitch and R. Osiander, "Terahertz Waves for Communications and Sensing", *Johns Hopkins Apl Technical Digest* **25**(4), pp. 345-355 (2004).

[25] T. Nagatsuma, *et al.*, "Challenges for Ultrahigh-Speed Wireless Communications Using Terahertz Waves", *Terahertz Science and Technology* **3**(2), pp. 55-65 (2010).

[26] G. P. Gallerano and S. Biedron, "Overview of terahertz radiation sources", in *Proc.* of FEL, Trieste, pp. 216–221 (2004).

[27] "Instant imaging with terahertz lasers", https://compoundsemiconductor.net/article/97378-instant-imaging-with-terahertz-lasers.html.

[28] "Project novelty", https://www.flash-project.eu/index.php?id=27

[29] M. C. Hoffmann and J. A. Fülöp, "Intense ultrashort terahertz pulses: generation and applications", *J. Phys. D: Applied Physics* **44**(8), 083001, pp. 17 (2011).

[30] K. Murate and K. Kawase, "Perspective: Terahertz wave parametric generator and its applications", *J. Appl. Phys.* **124**, 160901 (2018)

[31] K. Nakajima, "Novel efficient THz undulator using a laser-driven wire", Light: Science & Applications **6**, e17063 (2017).

[32] A. A. Ponomarenko, *et al.*, "Terahertz radiation from electrons moving through a waveguide with variable radius, based on Smith–Purcell and Cherenkov mechanisms", *Nucl. Instrum. Methods Phys. Res* **309**, pp. 223-225 (2013).

[33] A. Gover, *et al*., "Superradiant and stimulated-superradiant emission of bunched electron beams", Available online: https://arxiv.org/pdf/1810.07566.pdf.

[34] M. Dunning, *et al*., "Generating periodic terahertz structures in a relativistic electron beam through frequency down-conversion of optical lasers", *PRL* **109**, 074801 (2012).

[35] P. Michel, *et al*., "First lasing of the ELBE mid-IR FEL", in *Proc. of* FEL, 29 Aug - 3 Sep, Italy, pp. 8-13 (2004).

[36] V. P. Bolotin, *et al*., "A project of accelerator-recuperator for Novosibirsk high-power FEL", *Nucl. Instrum. Methods Phys. Res.* **543**(1), 81 (2005).

[37] M. J. Nasse, *et al*., "FLUTE: A versatile linac-based THz source generating ultra-short pulses", *Rev. Sci. Instr.* **84**, 022705 (2013).

[38] X. Su, *et al*., "Measurement of pre-bunched beam's longitudinal form factor based on radiation from a tunable-gap undulator", *Rev. Sci. Instr.* **89**, 013304 (2018).

[39] M. C. Chou, *et al*., "First observation of coherent THz undulator radiation driven by NSRRC high brightness photo-injector", in *Proc.* of FEL'07 Conf. 20–25 August, USA, MOP052, pp. 170-173 (2017).

[40] P. Boonpornprasert, *et al*., "Experimental optimization and characterization of electron beams for generating IR/THz SASE FEL radiation with PITZ", in *Proc. of* IPAC'17 Conf**.**, 14–19 May, Denmark,WEPAB033, pp. 2650-2653 (2017).

[41] E. Chiadroni, *et al.*, "Characterization of the THz radiation source at the Frascati linear accelerator", *Rev. Sci. Instr.* **84**, 022703 (2013).

[42] B. Green, "Superradiant Terahertz Sources and their Applications in Accelerator Diagnostics and Ultra-fast Science", Thesis, Karlsruhe Institute of Technology (2017).

[43] X. Wen, *et al.*, "Superradiant THz undulator radiation source based on a superconducting photo-injector", *Nucl. Instrum. Methods Phys. Res. A* **820**, 75 (2016).

[44] S. G. Liu and J. Urakawa, "Compact THz radiation source based on photocathode RF gun", *SCI CHINA PHYS MECH* **54**, 174 (2010).

[45] W. W. Li, *et al.*, "The design of a compact THz source based on photocathode RF gun", in *Proc.* of IPAC'13 Conf., 12-17 May, China, MOPFI039, pp. 375-377 (2013).

[46] S. Suphakul, *et al*., "Generation of short bunch electron beam from compact accelerator for Terahertz radiation", in *Proc.* of FEL, 8-13 May, Korea, TUPOW008, pp. 1757-1759 (2016).

[47] S. Suphakul, *et al*., "Measurement of Coherent Undulator Radiation of Compact Terahertz Radiation Source at Kyoto University", *Int. J. Magnetics Electromagnetism* **3**(1), IJME-3-008 (2017).

[48] S. Krainara, *et al.*, "Properties of THz Coherent Undulator Radiation (THz-CUR) at Kyoto University", *Rev. Sci. Instr.*, Status: Publish after revision.

[49] H. Zen, *et al*., "Pulse duration measurement of pico-second DUV photocathode driving laser by autocorrelation technique using two-photon absorption in bulk material", in *Proc.* of FEL, Santa Fe, USA, WEP014, pp. 439-441 (2017).

[50] "Nanophotonics and Terahertz Technology (NTT)", https://www.imp.tu-darmstadt.de/forschung_imp/ont_imp/ntt.de.jsp.

[52] B. B. Hu and M. C. Nuss, "Imaging with terahertz waves", *Opt. Express* **20**(16), pp. 1716–1718, (1995).

[53] Z. Jiang and X. C. Zhang, "Terahertz imaging via electrooptic effect", *IEEE Trans. Microw. Theory* **47**(12), pp. 2644–2650 (1999).

[54] B. M. Fischer, *et al*., "Terahertz time-domain spectroscopy and imaging of artificial RNA," *Opt. Express* **13**(14), pp. 5205–5215, Jul. 2005.

[55] J. H. Son, *et al.*, "Principle and applications of terahertz molecular imaging", *Nanotechnology* **24**(21), 214001 (2013).

[56] Z. Chen, *et al*., "A Survey on Terahertz Communications", *China Communications* **16(2)**, pp. 1 - 35 (2019).

[57] N. Devi, *et al.*, "Non-invasive macroscopic and molecular quantification of water in Nafion and SPEEK Proton Exchange Membranes using terahertz spectroscopy", *Journal of Membrane Science* **588**, 117183 (2019).

[58] W. Ghann and J. Uddin, book: Terahertz (THz) Spectroscopy: A Cutting‐Edge Technology (2017), Available online: DOI: 10.5772/67031.

Chapter 2

THz Coherent Undulator Radiation source driven by a photocathode RF gun

2.1 Introduction

THz Coherent Undulator Radiation (THz-CUR) generated from a compact source at Kyoto University is quasi-monochromatic radiation whose oscillation period is identical to the number of periods of the undulator. The intensity of CUR is proportional to a square of electron number, N_e^2 when the bunch length is shorter than the radiation wavelength. Since the electron beam energy of our source is fixed, the wavelength of CUR can only be varied by controlling the magnetic field of the undulator. Figure 2.1 presents the schematic of THz-CUR system. The system starts from the 1.6-cell S-band BNL-type photocathode RF-gun. To produce electrons, a cathode is illuminated with a 266 nm-UV laser. Then, the electron beam with the energy of 4.6 MeV is focused by a solenoid magnet. The electron bunch length is compressed by a magnetic chicane consisting of four dipole magnets. The focusing condition of electron beam is controlled by triplet quadrupole magnets before being sent to the undulator. The details of the main components of our source and theory involved with are described in this Chapter. The requirements of electron beam quality for THz-CUR generation with high power are listed as shown below

- High peak current in a micro pulse
- Short electron bunch
- High charge per bunch
- Low energy spread
- Low emittance
- High stability of electron emission

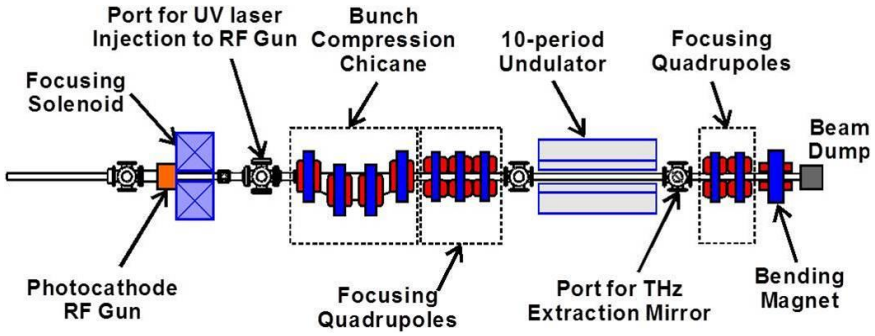

Figure 2.1: Schematic of the THz-coherent undulator radiation system at Kyoto University.

2.2 Photocathode RF gun

Electron gun is the main device used as an electron source to provide electrons for accelerators. The electron gun is classified for three main types depending on the method of electron extraction, which consists of photocathode RF gun, thermionic, and field emission RF gun. For the compact and economic structure, moderate cost, and easy in operation, a thermionic RF gun is a good candidate in comparison with other injectors. A crucial problem of thermionic RF gun is the effect of back-bombardment. Some electrons get into the decelerating phase and reverse back into the cathode after accelerated to heat up the cathode material. This feature makes the unstable operation and leads to the increase of beam current during the macropulse. Another drawback of using thermionic RF gun is a large energy spread of electron beam. To avoid the problems mentioned and to get a high electron bunch charge, we selected the photocathode RF gun for electron emission for a compact accelerator system. In this thesis, we will go in discussing the details of only the photocathode RF gun used in our system.

Nowadays, the requirements of brightness injector for accelerator can be fulfilled by a photocathode RF gun, which was first proposed, tested, and developed at Los Alamos by J. S. Fraser and R. Sheffield in 1985 [1]. A photocathode RF-gun is widely used at many facilities

of particle accelerator and is a reliable candidate of injector with a high electron brightness and high electron beam quality [2]. Although the photocathode RF gun requires a laser system with high cost and complicated operation, it draws attention to the production of high peak current and high quality of electron beam. The pulse shape is more flexible than that of other injectors because it can be controlled by the laser pulse shape. This injector provides the high bunch charge of electron beam because there is no back-bombardment effect. Electron beam can be generated with a high peak current, short pulse, low emittance, and low energy spread.

2.2.1 Photoemission

In the photocathode RF-gun, electrons are generated according to the photoelectric effect. When the photon illuminates a metal surface of the cathode material, the electrons can be emitted because the photon energy is transferred to electrons inside the surface of material. Thus the photon excites the electrons bound in a metal surface to higher energy states. The electrons are released outside from the metal surface with the kinetic energy (E_{KE}) if the photon energy is higher than the escape energy known as the work function (W_f) of material, $h\nu > W_f$. The work function refers to the minimum energy, which is needed for emission from the cathode surface. The photoemission in the processes of photoelectric effect can be described based on the three-step photoemission model of *Spicer's model* [2, 3]. This model includes the absorption of photon, migration to the surface, and electrons emission to vacuum as shown in Fig. 2.2 and reported in Ref. [3].

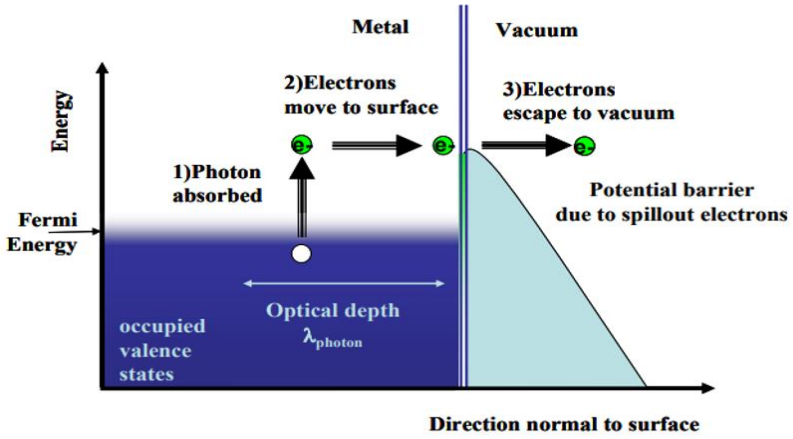

Figure 2.2: Three-step model of photoemission [3].

Total amount of energy required for electron extraction from the cathode surface can be simply expressed as

$$E_{KE} = h\nu - W_f \tag{2.1}$$

where E_{KE} is the kinetic energy of electrons, h is the Plank's constant (6.626×10^{-34} Js), and ν is the frequency of the photon.

The important quantity characterizing the photocathode to generate electrons from the metal surface is considered in term of quantum efficiency η, which is determined by the ratio of number of electrons and incident photons ($\frac{(I/e)}{P/h\nu}$), given in practical units [2]

$$\eta[\%] = 124\frac{I[\mathrm{mA}]}{P[\mathrm{W}]\lambda_l[\mathrm{nm}]} \tag{2.2}$$

where I is the emitted electron current from the cathode, P is the laser power, λ_l is the wavelength of laser light, e is the electron charge (1.602×10^{-19} C).

The quantum efficiency depends on the laser wavelength and the cathode material. For copper photocathode used, the quantum efficiency is 1×10^{-4}. It can be increased to $\eta > 1\times10^{-2}$ with a coating of the metal surface by alkaline metals such as Cs, Te. At present, several types of photocathode are being studied in order to increase the quantum efficiency, such as Cs_3Sb. The Cs_3Sb cathode has good current density and quantum efficiency but it requires a very good vacuum and has a shorter lifetime than that the metal cathodes [2, 4].

The amount of electron charge is dependent on the quantum efficiency and also the properties of laser pulse, defined in the compact form

$$Q\ [\mathrm{nC}] = 8.07\times10^{-3}\eta[\%]E_l[\mu\mathrm{J}]\lambda_l[\mathrm{nm}] \tag{2.3}$$

where E_l is the laser energy to excite the cathode.

From Equation (2.3), it can be seen that the emitted electron bunch charge is dependent on the laser properties such as laser energy and laser wavelength, and the quantum efficiency of cathode material. Besides the parameters as mentioned above, there is another effect to reduce quantum efficiency. That is in term of "*Schottky effect*", which consists of the image charges field and the applied field [3]. This effect has an influence on the work function of cathode material due to the applied fields, which can reduce the barrier and increase the quantum yield. Thus the effective work function with the other fields is expressed as

$$\emptyset_{eff} = W_f - \emptyset_{schottky} = W_f - e\sqrt{\frac{eE}{4\pi\varepsilon_0}}$$
$$= W_f - 0.037947\sqrt{E[\mathrm{MV/m}]}(e\mathrm{V}) \quad (2.4)$$

The quantum efficiency with the Schottky effect can be rewritten as

$$\eta \propto \left(hv - W_f + e\sqrt{\frac{eE}{4\pi\varepsilon_0}}\right)^2 \propto \left(hv - W_f + 0.037947\sqrt{E}\,\right)^2 \quad (2.5)$$

where W_f is the work function of the cathode material with no external electric field, and E is the electric field amplitude [MV/m].

Thus the electron charge is also dependent on the Schottky effect, thus getting

$$Q \propto \left(hv - W_f + e\sqrt{\frac{eE}{4\pi\varepsilon_0}}\right)^2 \quad (2.6)$$

In addition, an electron emission is perturbed by self-fields produced by the electron bunch itself so the space-charge field occurs at the cathode surface. When increasing laser energy higher than space-charge limited, total bunch charge is calculated with the following formula

$$Q_{emitted} = \pi r_m^2 \varepsilon_0 E_0 \sin\phi_0 + Q \exp\left(\frac{-r_m^2}{2\sigma_r^2}\right) \quad (2.7)$$

with the radius r_m defined as

$$r_m = \sigma_r\sqrt{2\ln\left(\frac{Q}{2\pi\varepsilon_0\sigma_r^2 E_0 \sin\phi_0}\right)} \quad (2.8)$$

where σ_r is the transverse distribution of the laser of Gaussian.

2.2.2 1.6-cell S-band BNL-type photocathode RF-gun

The 1.6 cell S-band RF gun is one of the most highly successful innovations in RF technology to produce electrons with the high brightness in a short bunch [1, 5-7]. The photocathode RF gun consists of a cathode in a half-cell followed by one full-length cell as shown in Fig. 2.3. This compact injector combines the acceleration in a high RF field and the generation of electrons by laser pulses hitting the cathode placed inside photocathode RF gun. After the laser pulse illuminates the cathode, electrons are emitted and quickly accelerated using high gradient fields.

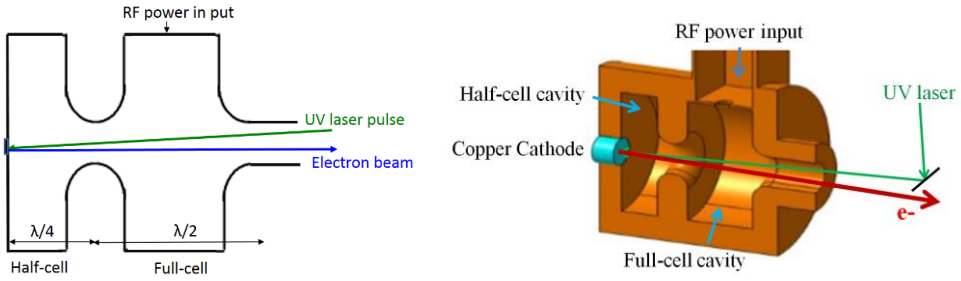

Figure 2.3: (left) Side view of RF gun and (right) cross section of the 1.6-cell S-band BNL-type photocathode RF gun.

The electron is emitted at the cathode surface via the photoelectric effect, and is accelerated by the electric field $E_z(z)$. The electric field in the RF gun is shown in Fig. 2.4. Microwave propagation within the cavity occurs as a standing wave with transverse magnetic field mode, TM010 with π-mode. The longitudinal electric field of the standing wave accelerating the electron bunch is given by

$$E_z(z) = E_0 \cos(kz) \sin(\omega t + \phi_0) \tag{2.9}$$

where E_0 is the maximum accelerating field amplitude

The longitudinal field is assumed to be independent of the transverse coordinate for the radial electric field and the azimuthal magnetic field [5], expressed by

$$E_r = -\frac{r}{2}\frac{\partial E_z}{\partial z},\ cB_\theta = \frac{r}{2c}\frac{\partial E_z}{\partial t} \tag{2.10}$$

where r and θ are the cylindrical coordinates.

The force on a particle defined by the radial Lorentz force is expressed as

$$\begin{aligned} F_r &= e(E_r - \beta c B_\theta) \\ &= er\left\{-\frac{1}{2}\left(\frac{dE(z)}{dz}\right)\cos kz \sin\sin(\omega t + \phi_0) - \frac{1}{2c}\frac{d}{dt}\left(E_0 \sin(kz)\cos(\omega t + \phi_0)\right)\right. \\ &\quad \left. + \frac{\beta}{2}\frac{dE(z)}{dz}\left(\sin(kz)\cos(\omega t + \phi_0)\right)\right\} \end{aligned} \tag{2.11}$$

If ϕ_0 is the phase of the central particles in the bunch when emitted from the cathode, its asymptotic phase at the RF gun exit is expressed as follows

$$\phi = \omega t - kz + \phi_0$$

$$= k\int_0^z \left(\frac{\gamma}{\sqrt{\gamma^2-1}} - 1\right) dz + \phi_0 \quad (2.12)$$

where k is the RF wave number, $k = 2\pi/\lambda$, λ is the RF wavelength, and ϕ_0 is the RF phase of the central electron when leaving from the cathode and starting to be accelerated at zero longitudinal position z.

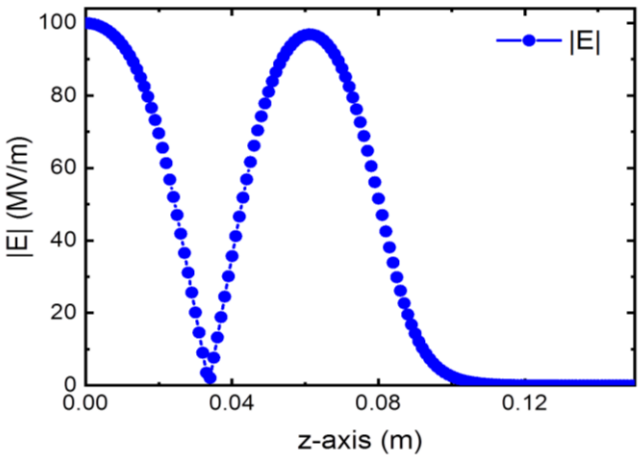

Figure 2.4: Longitudinal accelerating electric field of RF cavity of 1.6-cell S-band BNL-type photocathode RF-gun.

The pulse structure of the emitted electron beam is dependent on the laser properties. The electron beam can be formed at the RF gun exit. The electron beam energy on longitudinal position with respect to the RF phase for acceleration (Fig. 2.5) is expressed as

$$\frac{d\gamma}{dz} = \frac{eE_0}{2m_0c^2}\left[sin\phi + \sin(\phi + 2kz)\right] \quad (2.13)$$

where e is the electron charge, m_0 is electron's mass, c is the speed of light.

If electrons leave the cathode with no kinetic energy, the energy chirp becomes

$$\frac{d\gamma}{dz} = \frac{eE_0}{mc^2}\sin\phi_0 \quad (2.14)$$

The electron's relativistic energy is simply calculated by Eq. (2.15),

$$\gamma = 1 + \alpha[kz\sin\phi + 0.5(\cos\phi - \cos(\phi + 2kz))] \quad (2.15)$$

where α is a dimensionless parameter representing the strength of the accelerating field, given by

$$\alpha = \frac{eE_0}{2m_0c^2k} \tag{2.16}$$

where k is the wave number defined as ω_{rf}/c.

At the RF gun exit, the electron's relativistic energy is simply calculated by

$$\gamma = 1 + \alpha[(n + 1/2)\pi \sin\phi + \cos\phi] \tag{2.17}$$

where n is the integer.

The energy spread is proportional to the initial electron bunch, given by

$$\frac{\Delta U}{U} = \frac{2f_{RF}\sigma_b}{n+0.5} \tag{2.18}$$

where σ_b is the bunch length of electron bunch emission.

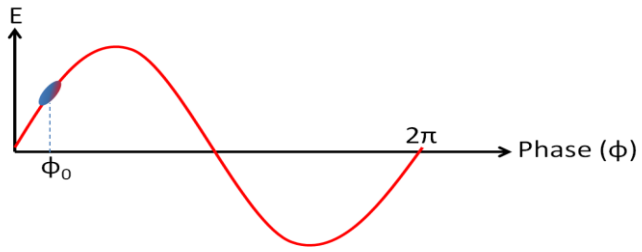

Figure 2.5: Accelerating electric fields of the RF gun and an electron bunch.

At Kyoto University, the 1.6-cell S-band BNL-type photocathode RF gun manufactured in KEK in 2008 has been installed and used as an electron source in the generation of the high brightness electron beam. From the RF gun parameters of our source, the calculated peak accelerating field E_0 corresponding to the RF frequency of 2,856 MHz is 100 MV/m [8] thus the electron beam energy was accelerated to 4.6 MeV with RF power of 9 MW. The difference of the RF phase and laser injection phase can be adjusted by the electronics phase shifter.

The properties of the extracting electron beam from the RF gun can be estimated by an analytical calculation reported by K. J. Kim [5]. For short bunches with Gaussian distributions, the electron beam parameters at the gun exit such as the rms angular divergence, σ_x' can be written as

$$\sigma_x' = \frac{2\pi\alpha f_{RF}}{\gamma c}\sigma_x \tag{2.19}$$

where γ is the Lorentz factor and σ_x is the beam size.

The electron beam quality such as emittance can determine the performance of photocathode RF gun. The emittance of electron beam blows up immediately after electron emission and entering inside the first cell. Since an electron bunch has a high space-charge effect, the electron beam can diverge quickly. The solenoid magnet is employed to focus the electron beam. In general, the normalized emittance can be calculated beginning with the definition in the following expression

$$\varepsilon_n = \beta\gamma\sqrt{\langle x^2\rangle\langle x'^2\rangle - \langle xx'\rangle^2} \tag{2.20}$$

where x and x' are the position and angle of the electron, respectively.

In case of photocathode RF gun, the emittance is composed of the three main elements according to the causes of the space-charge induced emittance (ε_{sc}), the linear RF-induced emittance (ε_{rf}), and the thermal emittance (ε_{th}) [9]. The thermal normalized emittance at the cathode is independent on laser shape and it is defined as the photocathode's intrinsic emittance, given by

$$\varepsilon_{x,y}^t \cong r\sqrt{\frac{\Delta E}{mc^2}} \quad \text{or} \quad \varepsilon_{x,y}^t[\pi\ \text{mm mrad}] \cong \sigma_{x,y}[\text{mm}] \tag{2.21}$$

where r is the cathode radius and ΔE is the difference between the photon energy and the cathode work function.

For an electron beam with a Gaussian distribution, the linear RF-induced emittance is given by

$$\varepsilon_{rf} = 4\sqrt{2}\pi^3\frac{\alpha f^3}{c}\sigma_x^2\sigma_b^2 \tag{2.22}$$

where σ_x and σ_b are rms radius and bunch length, respectively.

The space-charge induced emittance growth can be described in terms of the beam peak current I and the charge density distribution in the form

$$\varepsilon_{sc} = \frac{c^2}{8\alpha f\sin\phi_0}\frac{I}{I_A}\frac{\sigma_b}{(3\sigma_x+5c\sigma_b)} \tag{2.23}$$

where σ_b is the bunch length in time and I_A is the so-called Alfven current equal to 17000 A.

The peak current for a Gaussian distribution is defined by

$$I = \frac{Q}{\sqrt{2\pi}\sigma_b} \tag{2.24}$$

Equation (2.23) can be rewritten in the following expression

$$\varepsilon_{sc} = \frac{c^2}{8\sqrt{2\pi}\alpha f \sin\phi_0}\frac{Q}{I_A}\frac{1}{(3\sigma_x+5c\sigma_b)} \tag{2.25}$$

The final emittance at the gun exit is indeed given by the quadratic sum of the total emittance with the following expression

$$\varepsilon_{total} = \sqrt{\varepsilon_{rf}^2 + \varepsilon_{sc}^2 + \varepsilon_{th}^2} \tag{2.26}$$

Due to the effects explained above, the electron beam quality can be determined and controlled by the management of laser pulse distribution. If the electrons are extracted from the cathode with high charge density, the space-charge field will occur and disturb to the emittance of electron beam. Thus the laser pulse shape also has a significant impact on electron beam quality.

2.3 Laser system

A laser system is one of the keys of an electron injector based on the photocathode source, which has been developed for a photocathode illumination. The laser pulses are time-synchronized with the electron beam, as well as the driven laser. To emit the electrons, the cathode is irradiated by a 266 nm-UV laser with the laser pulse width of 5.8 ps in FWHM [10, 11]. Its pulse width is shorter than the designed pulse duration of 7.5 ps-FWHM of Nd:YVO4 mode-locked oscillator because it is shortened by wavelength conversion using the second and fourth harmonic generation crystals. At the cathode, the transverse profiles of laser assumed to be Gaussian distribution is 0.5 mm and 0.4 mm-rms for vertical and horizontal sizes, respectively. The laser pulse is transported to the copper cathode by several UV enhanced aluminum mirrors.

Figure 2.6 shows the schematic of the laser system used in our source. The main components of laser system are as follows

1. Passively mode-locked Nd:YVO_4 oscillator with built-in acousto-optics modulator (Time bandwidth, GE-100-VAN-89.25MHz-CLX-Flexible AOM),
2. Beam alignment control system (Aligna4D, TEM) ,
3. Three laser diode pump amplifiers (REA5006-2P1,CEO),
4. Non-linear crystals of the second harmonic generation (SHG) and forth harmonic generation (FHG),
5. Faraday isolators.

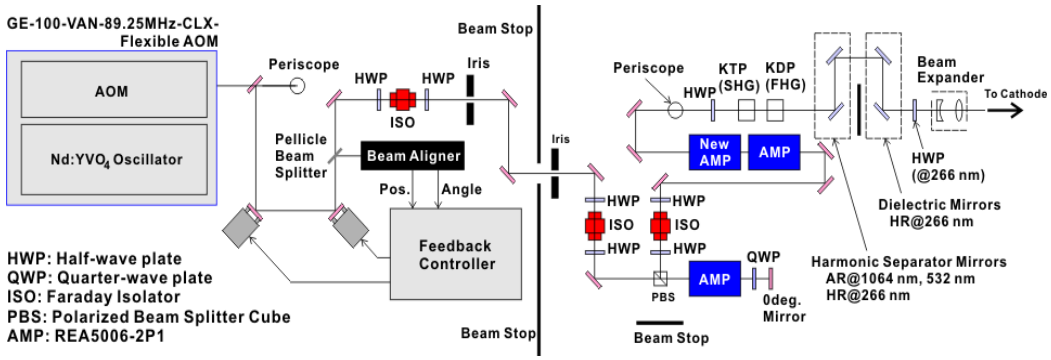

Figure 2.6: Schematic diagram of the laser system for the photocathode RF gun.

The oscillator containing the neodymium-doped yttrium orthovanadate (Nd:YVO_4) laser diode provides a continuous laser at the wavelength of 1064 nm with the repetition frequency of 89.25 MHz and the pulse duration of 7.5 ps at the full width at half maximum (FWHM) to send to an optical cavity, which consists of a concave mirror and flat mirrors. The optical cavity and the cavity length are adjusted to a proper condition to produce a mode-locked laser pulse. Feedback controlled piezo electric actuator (PZT) is used to compensate for the change of the cavity length due to the temperature fluctuation. Using the Semiconductor Saturable Absorber Mirror (SESAM), the intensity light inside the cavity remains only a high-intensity light pulse while the low intensity is absorbed. Acousto-Optics Modulator (AOM) is employed for modulating the amplitude of the pulse train. AOM with an arbitrary waveform generator (AFG3251, Tektronix) is used for the control of generated macro-pulse length.

Due to the temperature fluctuation causing the change of dimensions of the resonance cavity, the temperature of laser room is controlled at 23 ºC to solve the problem. The beam alignment feedback control (Aligna4D, TEM) is used for controlling the beam position and angle stabilization. Reflected laser light can be obstructed by using the Faraday isolators with the half-wave plates in 45 degrees polarization. Three laser diode pumped amplifiers

(REA5006-2P1, CEO) are employed to amplify the laser intensity. The laser pulses propagate to the non-linear crystals of the second harmonic generation (SHG) and fourth harmonic generation (FHG), which are composed of the pair of the potassium titanyl phosphate (KTP) crystal and the potassium dihydrogen phosphate (KDP) crystal, respectively. Eventually, the laser with the wavelength of the fourth harmonic wavelength at 266 nm can be generated and transported to the photocathode by using several optical components. The efficient of laser intensity to cathode is about 82-92% transportation. The laser parameters for injecting to cathode inside photocathode RF-gun are listed in Table 2.1.

In Fig. 2.7 one can see the time structure of the RF pulses and the laser pulses. The laser pulse has a repetition rate of 89.25 MHz. It provides the time duration between pulses of 11.2 ns or 32 times longer than the RF pulse duration that is 350.14 ps of a frequency of 2,856 MHz. The macropulse duration of the RF pulse is set at 2 μs, with the RF pulse repetition rate of 2 Hz.

Table 2.1: Parameters of the photocathode RF gun laser system.

Parameters	Values
Laser system	
Oscillator type	Passively mode-locked
Oscillator wavelength	1064 nm
Wavelength after FHG	266 nm
Repetition frequency of micropulse	89.25 MHz
Pulse duration (FWHM)	5.8 ps
Optical transportation efficiency	82 - 92%
Laser rms radius	0.5 mm
Laser pulse energy	< 200 μJ
RF system	
Electric field at cathode	100 MV/m
RF frequency	2856 MHz
Peak power	9 MW
RF pulse duration	2 μs
RF pulse repetition rate	2 Hz

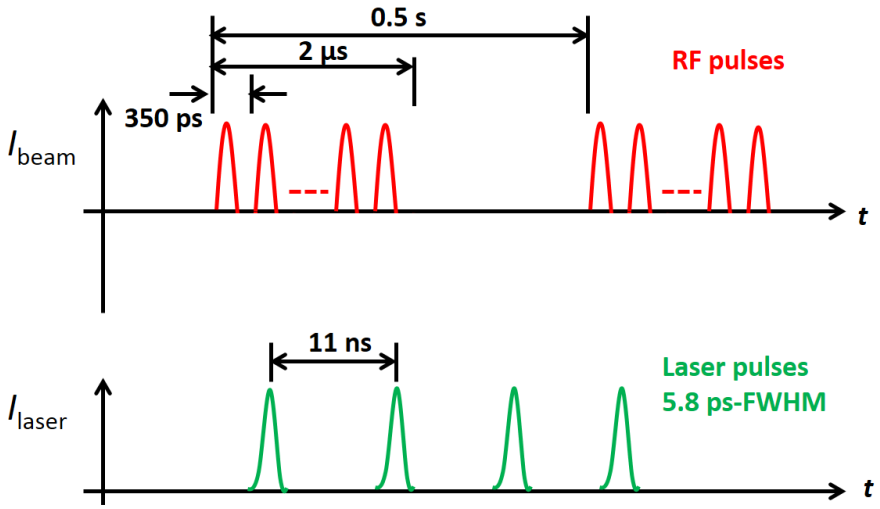

Figure 2.7: Time scheme of (top) the RF pulse and (bottom) the laser pulse.

2.4 Bunch compressor

A chicane bunch compressor is a potential component to obtain a short bunch length by rotating the longitudinal phase space. There are several types of bunch compressor. The simplest one consists of four bending magnets. The energy chirp of the bunch depends on the relative phase between the RF pulse and the injection phase. The R_{56} value before the chicane magnet has to be suitable and to match with the energy chirp h ($d\delta/cdt_{t=0}$) of an initial bunch to obtain a minimum bunch length after bunch compression. The energy chirp of the electron bunch at the RF gun exit by using the GPT simulation code will be described in Chapter 4.

The change of energy chirp inside RF gun at position z_0 on the zero crossing of the longitudinal electric field can be written as in Equation (2.13). The linear energy chirp depending on the electric field accelerating is expressed in the form [12]

$$h = \frac{1}{E_0}\frac{dE}{dz} \cong \frac{1}{E + e\Delta V_0 \cos\phi}\frac{d}{dz}[E + e\Delta V_0 \cos\phi - e\Delta V_0 kz \sin\phi + o(z^2)]$$
$$= -(e\Delta V_0 k \sin\phi)/(E + e\Delta V_0 \cos\phi) \quad (2.27)$$

where E is the electron beam energy.

The dependence of a particle's z-coordinate in the chicane with a proper energy chirp is obtained by

$$z_1 = z_0$$
$$\delta_1 = hz_0 + \delta_0 \quad (2.28)$$

where δ is $\Delta E/E$, h is energy chirp $(d\delta/cdt_{t=0})$, and t is the time position of each electron and c is the speed of light.

In the linear approximation, the longitudinal particle distribution at the exit of the chicane is defined by

$$\begin{aligned} z_2 &= z_1 + R_{56}\delta_1 \\ &= z_0 + R_{56}(hz_0 + \delta_0) \\ &= (1 + hR_{56})z_0 + R_{56}\delta_0 \end{aligned} \tag{2.29}$$

where R_{56} is the chicane matrix element or the 1st order momentum compaction.

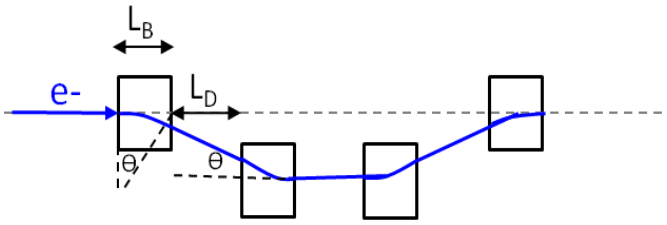

Figure 2.8: Layout of chicane bunch compressor with four bending magnets.

For a simple chicane bunch compressor with four dipoles (Fig 2.8), the R_{56} referring to the change of the bunch length due to the bunch compressor can be defined by

$$R_{56} = \int \eta/\rho ds \approx -2\Theta^2(L_D + 2/3L_B) \tag{2.30}$$

where R_{56} is the 1st momentum compact factor or the linear longitudinal dispersion of the dispersive section, η is dispersion function, ρ is the bending radius, θ is deflection angle relating to total magnetic fields seen by electrons $\theta = e/p \int B ds$, B is the bending magnetic field, p is the momentum of electron, L_B is the physical length of the bending magnet, and L_D is the drift length between the 1st and the 2nd bending magnet.

According to the bunch compression, the R_{56} at the exit of the chicane has to match with the energy chirp (h) of the initial bunch, given by

$$R_{56} = -1/h \tag{2.31}$$

The path length in the chicane can be rewritten as

$$s_1 - s_0 \approx L_B\left(\frac{\theta}{1+\delta}\right)^2 - L_B\theta^2 = \frac{1}{2}R_{56}\left(1 - \frac{1}{(1+\delta)^2}\right) \tag{2.32}$$

The longitudinal phase space of electron beam when passing through the chicane bunch compressor is illustrated in Figure 2.9(right). The tail particles with higher energy are kicked with a smaller deflection angle so they travel with short path length while head particles with lower energy travel with longer path length along with the chicane magnets. The compressed bunch length σ_1 can be approximately expressed from its original bunch length σ_0 as [13]

$$\sigma_1 = \sigma_0 + R_{56}\delta + T_{566}\delta^2 + U_{5666}\delta^3 + \cdots \quad (2.33)$$

where $T_{566} = -3R_{56}/2$ and $U_{5666} = 2R_{56}$, δ is the relative energy spread.

In our source, the magnetic chicane bunch compressor has been constructed and composed of four rectangular dipole magnets each with length L dipole of 0.065 m and pole width of 0.1 m as shown in Fig. 2.9(left). The energy slit is also set between 2nd dipole and 3rd dipole with a width of 0.1 m. To compensate the dispersion and transverse beam offset at 2nd and 3rd dipole magnets, the additional correction coils are added with 0.3 mT [8]. The measured magnetic field as a function of the coil current of the chicane magnet installed in our source is shown in Fig. 2.10.

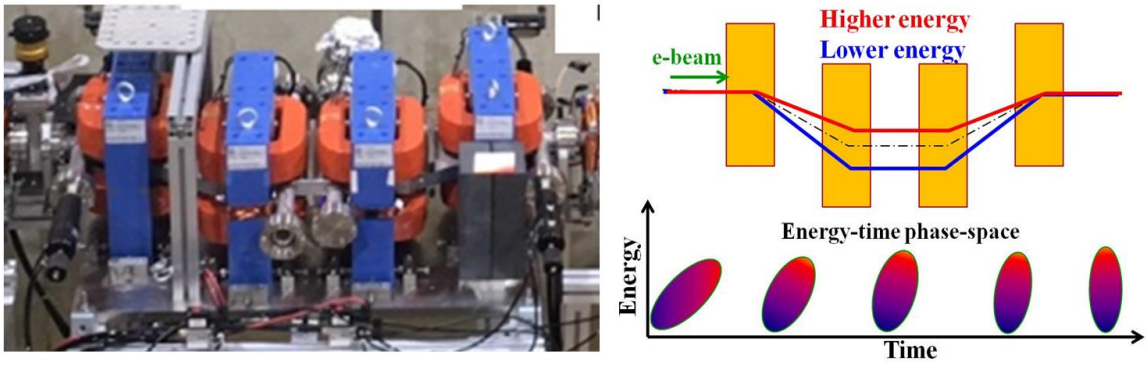

Figure 2.9: (left) Chicane bunch compressor and (right) schematic layout of the negative R_{56} chicane.

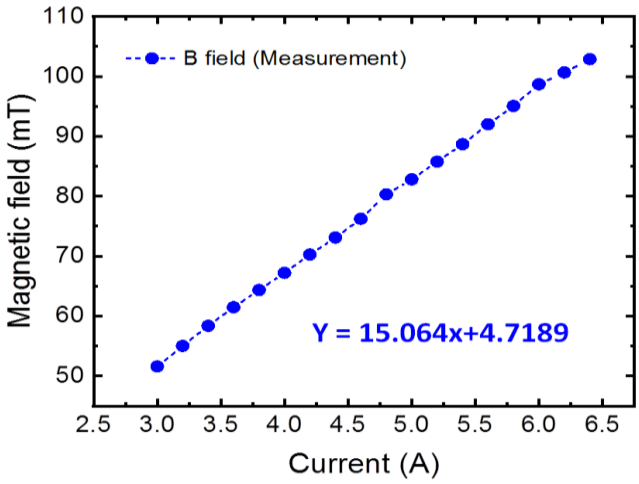

Figure 2.10: Magnetic field at the center of the pole gap as a function of the exited coil current by the measurement.

2.5 Magnets for the compensation of electron beam optics

The main magnets for the compensation of electron beam optics in our system consist of a solenoid magnet to compensate emittance growth due to linear space-charge force, and the triplet quadrupoles to compensate beam optics disturbed by the undulator magnetic field. In addition, there are several steering magnets to align electron beam along beamline, double quadruples, and bending magnet at the end of beamline to compensate beam optics for the measurements of bunch charge and beam energy as detailed in [8].

2.5.1 Solenoid magnet

An electron beam quality depends greatly on electron distributions both in transverse and longitudinal phase spaces. The transverse phase space depends significantly on the emittance, which is one of the most important properties to determine the quality of the RF electron gun. Electrons emitted from the cathode produce the space-charge field thus the defocusing force on the electron beam appears to expand in transverse direction at the beginning of acceleration. The property of electron (e.g. emittance) gets worse in quality. A solenoid magnet is employed for the emittance compensation. In the low energy section of accelerators, the transverse emittance can be compensated by applying the solenoid field, which is used to focus the charged particle beam. Since the focal length of the solenoid magnet relates to the energy of the particle inside a bunch, the electrons in the bunch with energy spread are

focused at different positions. Applying Ampere's law to determine the field inside a solenoid, the longitudinal magnetic field can be written as

$$B_z = \mu_0 nI \tag{2.34}$$

where I is the applied current, and n is the number of turns per unit length (N/L) or turns density.

The solenoid magnet focuses the beam in transverse direction with the edge fields of $B_x = -\frac{1}{2}\frac{\partial B_z}{\partial z}x$ and $B_y = -\frac{1}{2}\frac{\partial B_z}{\partial z}y$ for horizontal and vertical axis. The transfer matrix (M_s) of the solenoid consists of the matrices corresponding to the entrance fringe field, the constant axial magnetic field, and the output fringe field, respectively [14], given as

$$M_s = M_1 M_2 M_3 \tag{2.35}$$

$$M_s = \begin{bmatrix} 1 & 0 & 1 & 0 \\ 0 & 1 & \alpha & 0 \\ 1 & 0 & 1 & 0 \\ -\alpha & 1 & 0 & 1 \end{bmatrix} \begin{bmatrix} 1 & \left(\frac{1}{2\alpha}\right)\sin\theta & 0 & \left(\frac{1}{2\alpha}\right)(1-\cos\theta) \\ 0 & \cos\theta & 0 & \sin\theta \\ 0 & 0 & \left(-\frac{1}{2\alpha}\right)(1-\cos\theta) & \left(\frac{1}{2\alpha}\right)\sin\theta \\ -\sin\theta & \cos\theta & 0 & \cos\theta \end{bmatrix} \begin{bmatrix} 1 & 0 & 1 & 0 \\ 0 & 1 & -\alpha & 0 \\ 1 & 0 & 1 & 0 \\ \alpha & 1 & 0 & 1 \end{bmatrix}$$

$$M_s = \begin{bmatrix} C^2 & CS/\alpha & CS & S^2/\alpha \\ -CS\alpha & C^2 & -S^2\alpha & CS \\ -CS & -S^2/\alpha & C^2 & CS/\alpha \\ S^2\alpha & -CS & -CS\alpha & C^2 \end{bmatrix} \tag{2.36}$$

where $S = \sin\theta/2$, $C = \cos\theta/2$, $\alpha = \sqrt{k}$, $\theta = 2L\alpha$, $k = (B_z/2B\rho)^2$, B_z is the magnetic field, $B\rho$ is the magnetic rigidity, L is the effective length of solenoid.

Assuming the thin lens approximation with small kL, the beam transfer matrix can be written as below

$$M_s = \begin{bmatrix} 1 & 0 & 0 & 0 \\ -1/f & 1 & 0 & 0 \\ 1 & 0 & 1 & 0 \\ 0 & 0 & -1/f & 1 \end{bmatrix} \tag{2.37}$$

where f is the focal length of solenoid magnetic, given by $\frac{1}{f} = kL = (B_z/2B\rho)^2 L$.

In this source, the solenoid magnet in Fig. 2.12(left) is located at the position of 0.4 m from the beginning, which is installed at downstream of the RF gun. Figure 2.11(right) plots the magnetic field as a function of exciting current from the measurement. The magnetic field

at the center is about 0.2 Tesla as shown in Fig. 2.11(left). Regarding an ideal solenoid, the magnetic field can be generated only in longitudinal direction without transverse field. In GPT simulation, the current in A-turns can be converted to the magnetic field, calculated from [15]

$$B_z = \frac{1}{2}\mu_0 nI\left[\frac{z+L/2}{\left\{(z+L/2)^2+R^2\right\}^{1/2}} - \frac{z-L/2}{\left\{(z-L/2)^2+R^2\right\}^{1/2}}\right] \tag{2.38}$$

Where μ_0 is permeability, L is the solenoid length (m), R is radius of the solenoid, and nI is the solenoid current (A-turns).

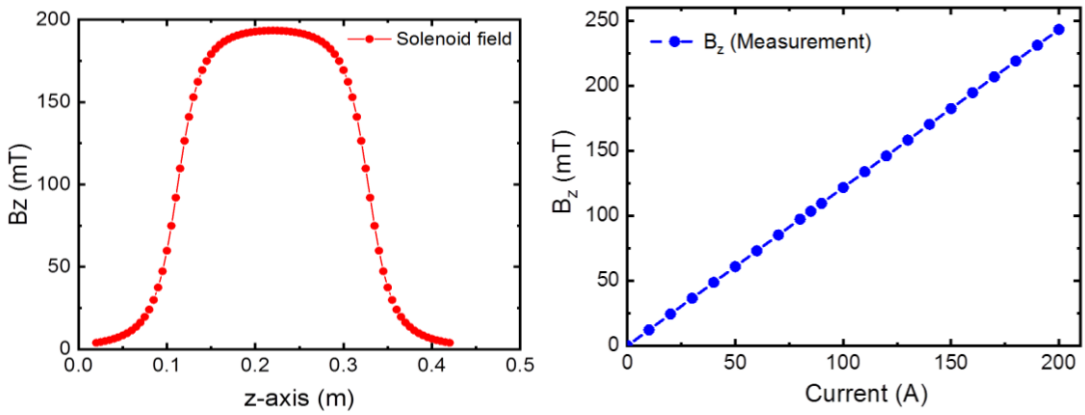

Figure 2.11: (left) Longitudinal magnetic of solenoid field along *z* axis and (right) measured peak longitudinal magnetic field as a function of the excited currents.

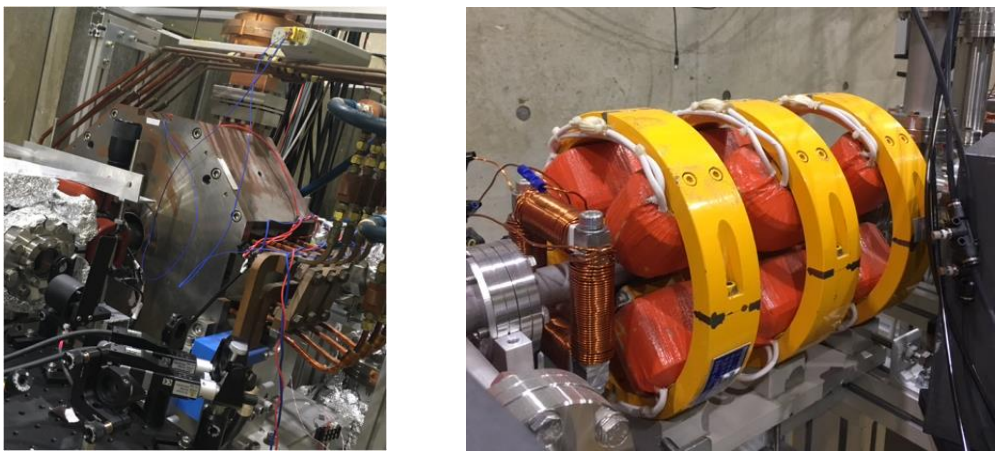

Figure 2.12: (left) Solenoid magnet and (right) Triplet quadrupole magnets.

2.5.2 Triplet quadrupoles for beam matching

The quadrupole magnet has four magnetic poles that generate the magnetic field with magnetic flux density varying along the distance from the magnet center. According to Coulomb's law, the forces among electrons can cause the beam to spread out far from the center. Thereby, this magnet is used to focus the electron beam. A quadrupole magnet is able to focus the beam in one direction while defocusing in another direction. Therefore, there are two families of quadrupoles called "focusing quadrupole" and "defocusing quadrupole". Figure 2.10(right) shows the triplet quadrupoles consisting of two focusing magnets and one defocusing magnet.

In the center of the magnet, there is a magnetic field in free region. The transverse magnetic fields in x and y axis are given by

$$B_x(x, y) = g_x y$$
$$B_y(x, y) = g_y x. \quad (2.39)$$

where g_x and g_y are the magnetic field gradients, B_x and B_y are the magnetic field in x and y planes, respectively. The field gradient (g) of quadrupole is calculated from

$$g = 3.3355 \frac{E}{f \cdot L_{eff}} \quad (2.40)$$

where E is electron beam energy, f is the focal length, and L_{eff} is the effective length of quadrupole magnet.

Transformation matrices of transverse focusing quadrupole are

$$M_{xx} = \begin{bmatrix} \cos\sqrt{k}L & \sin\sqrt{k}L/\sqrt{k} \\ \sqrt{k} * \sin\sqrt{k}L & \cos\sqrt{k}L \end{bmatrix}, \quad M_{yy} = \begin{bmatrix} \cosh\sqrt{k}L & \sinh\sqrt{k}L/\sqrt{k} \\ \sqrt{k} * \sinh\sqrt{k}L & \cosh\sqrt{k}L \end{bmatrix} \quad (2.41)$$

Transformation matrices of a transverse defocusing quadrupole are

$$M_{xx} = \begin{bmatrix} \cosh\sqrt{k}L & \sinh\sqrt{k}L/\sqrt{k} \\ \sqrt{k} * \sinh\sqrt{k}L & \cosh\sqrt{k}L \end{bmatrix}, \quad M_{yy} = \begin{bmatrix} \cos\sqrt{k}L & \sin\sqrt{k}L/\sqrt{k} \\ \sqrt{k} * \sin\sqrt{k}L & \cos\sqrt{k}L \end{bmatrix} \quad (2.42)$$

where k is focusing strengths of quadrupole magnet, L is quadrupole length.

Due to the focusing/defocusing nature of quadrupole magnets, they are commonly placed in groupings of three magnets to supply the necessary focusing in both planes to correct the mismatched beam optics disturbed by undulator field. The strength of the magnets and the

size of the drift space between quadrupoles must be optimized to supply the necessary focusing for the beam at the designed focal point in the beam line. The focal length of three quadrupoles in series with each quadrupole acting as a lens with focal lengths (f_1, f_2, f_3) can be expressed as

$$f = \frac{f_1 f_2 f_3}{f_3(f_2 + f_1 - s_1) + f_1 f_2 + s_2 f_2 + s_2 f_1 - s_1 s_2} \tag{2.43}$$

where s_1 and s_2 are the drift spaces between subsequent quadrupoles.

These quadrupoles can be used to focus the electron beam and correct beam optics into the undulator. In THz-CUR source, the triplet quadrupole magnets are installed at upstream undulator. The distance from center to center of another quadrupole is 0.1 m. The arrangement is the focusing, defocusing, and focusing magnets. The effective length of the quadrupole is 0.055 m as defined by $\int B_z dz/g_x$ where B_z is the magnetic field in the longitudinal direction and g_z is the magnetic field gradient as shown in Fig. 2.13.

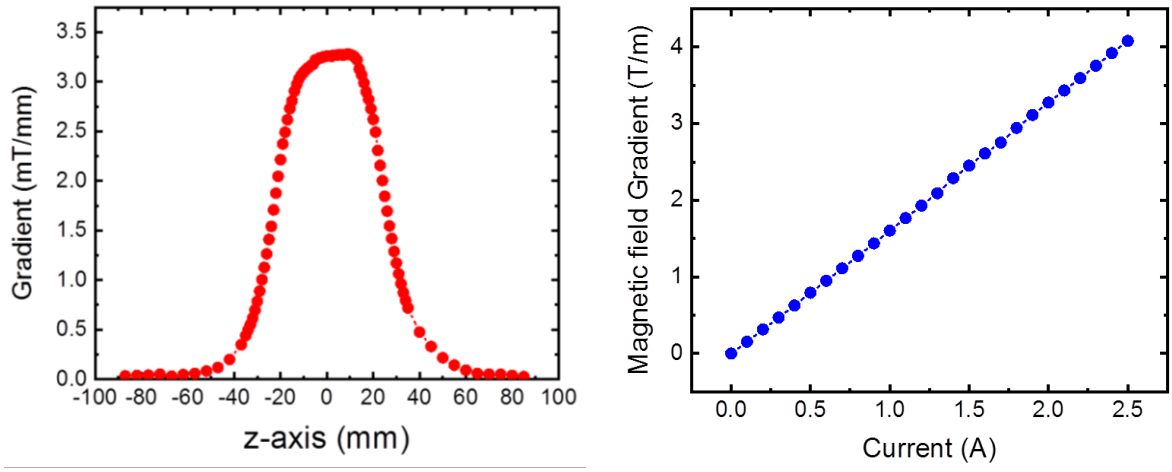

Figure 2.13: (left) measured results of the longitudinal magnetic fields and (right) magnetic field gradient of the quadrupole magnet from the measurements.

2.6 Electron motion in a planar undulator

In general, an undulator is composed of a periodic structure of dipole magnets, which can be the permanent magnets or superconducting magnets depending on the type of undulator. Intense radiation is generated with narrow spectrum bandwidth when the relativistic electrons travel through an undulator. Each electron emits a wave train with the period number of

undulator in the forward direction. For an ideal planar vertical deflection undulator, a magnetic field is assumed to be purely sinusoidal in the horizontal direction as simply shown in Fig. 2.14. The undulator magnet is to produce a sinusoidal field with a peak field B_0, given by

$$\begin{aligned} B_x &= B_0 \cos\left(2\pi z / \lambda_u\right), \\ B_y &= 0, \\ B_z &= 0 \end{aligned} \tag{2.44}$$

where B_0 is the peak magnetic field and λ_u is the undulator wavelength.

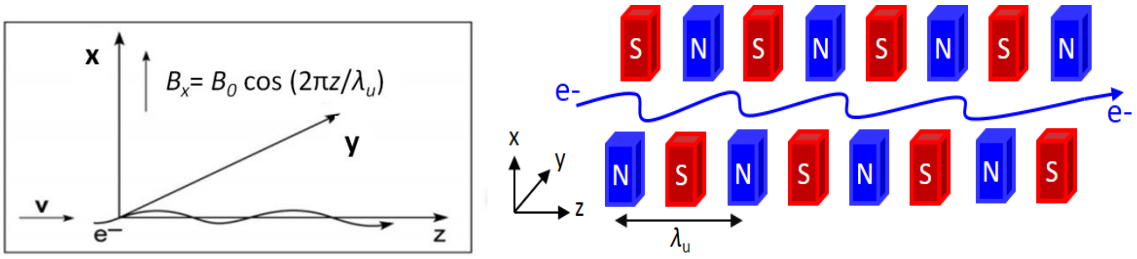

Figure 2.14: Electron motion along an undulator.

The Lorentz force can be obtained to electron motion with velocity $\vec{v}$ inside a device magnet with the magnetic field $\vec{B}$ [16] as follows

$$\frac{d\vec{p}}{dt} = \frac{d(\gamma m_0 \vec{v})}{dt} = -e\left(\vec{v} \times \vec{B}\right) \tag{2.45}$$

where $\vec{p}$ is the particle momentum, e is the electron charge, m_0 is the electron mass, and γ is the relativistic factor.

For the vertical deflection undulator, the electron beam has a sinusoidal trajectory on axis and only the electron motion in the vertical plane occurs while the horizontal motion is normally negligible. The equation of electron motion can be written as

$$\begin{aligned} \frac{d^2x}{dt^2} &\cong 0 \\ \frac{d^2y}{dt^2} &= \frac{ev_z}{\gamma m_0 c} B_0 \sin k_u z \\ \frac{d^2z}{dt^2} &= -\frac{ev_y}{\gamma m_0 c} B_0 \sin k_u z \end{aligned} \tag{2.46}$$

From the equation of motion with the initial condition of $v_y = -cK/\gamma$, the electron velocity under the magnetic field of the undulator can be obtained by

$$\begin{aligned} \frac{dx}{dt} &= 0 \\ \frac{dy}{dt} &= -c\frac{K}{\gamma}\cos(k_u z) \\ \frac{dz}{dt} &\approx \beta c\left[1 - \frac{1}{2}\frac{K^2}{\gamma^2}\cos^2(k_u z)\right] \end{aligned} \tag{2.47}$$

where K is undulator parameter, $eB_0\lambda_u/(2\pi m_0 c)$.

Thus the electron trajectory in the planar undulator is given as

$$\begin{aligned} x(t) &= 0 \\ y(t) &= -\frac{K}{k_u\gamma}\sin(\omega_u t) \\ z(t) &= \overline{v}t - \frac{K^2}{8\gamma^2 k_u}\sin(2\omega_u t) \end{aligned} \tag{2.48}$$

with the average longitudinal speed $\overline{v} = c\left(1 - \frac{1}{2\gamma^2}(1 + K^2/2)\right)$.

The radiation wavelength observed into the laboratory frame is represented as

$$\begin{aligned} \lambda_r &= \lambda_u(1 - \bar{\beta}\cos\theta) \\ &= \frac{\lambda_u}{2\gamma^2}\left(1 + \frac{K^2}{2} + \gamma^2\theta^2\right) \end{aligned} \tag{2.49}$$

with $\bar{\beta} = 1 - \frac{1}{2\gamma^2}\left(1 + \frac{K^2}{2}\right)$ and $\cos\theta \approx 1 - \theta^2/2$.

The radiation wavelength (λ_r) in forward direction can be determined by

$$\lambda_r \approx \frac{\lambda_u}{2\gamma^2}\left(1 + \frac{K^2}{2}\right) \tag{2.50}$$

where λ_u is the undulator period length, γ is the Lorentz factor, and θ is the observation angle from the beam direction.

The undulator strength parameter is rewritten in practical unit

$$K = 0.934 B_0[\text{Tesla}]\lambda_u[\text{cm}] \tag{2.51}$$

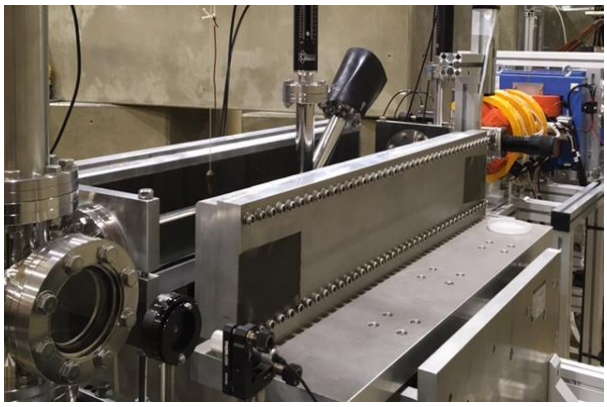

Figure 2.15: Planar Halbach type undulator permanent magnet for THz-CUR at Kyoto University.

Table 2.2: Undulator parameters used in THz-CUR at Kyoto University

Parameters	Values
Undulator	Planar Halbach type with permanent magnets
Gap	30 – 90 mm
Number of period	10 periods
Period length	0.07 m
Maximum magnetic field	0.43 Tesla

For our system, the undulator of planar Halbach type (Fig. 2.15) constructed from either permanent magnet is one of the main components. It has several advantages in terms of performance, compactness, and cost-effectiveness. The magnetic field strength is changed by controlling the undulator gap as shown in Fig. 2.16. The period length and the number of period of the undulator are 0.07 meters and 10 periods, respectively. The undulator specifications are listed in Table 2.2. The gap can be manually adjusted between 30 mm to 90 mm.

Essentially, the radiation with a frequency of 0.16 THz can be emitted from undulator of 0.43 Tesla with an undulator parameter of 2.83 with the 30-mm gap. The peak magnetic field and undulator strength parameter as a function of the undulator gap are plotted in Fig. 2.17.

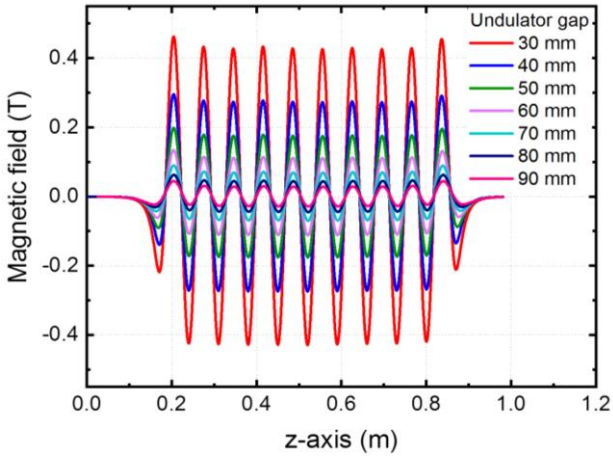

Figure 2.16: Magnetic field distribution along undulator as a function of undulator gap.

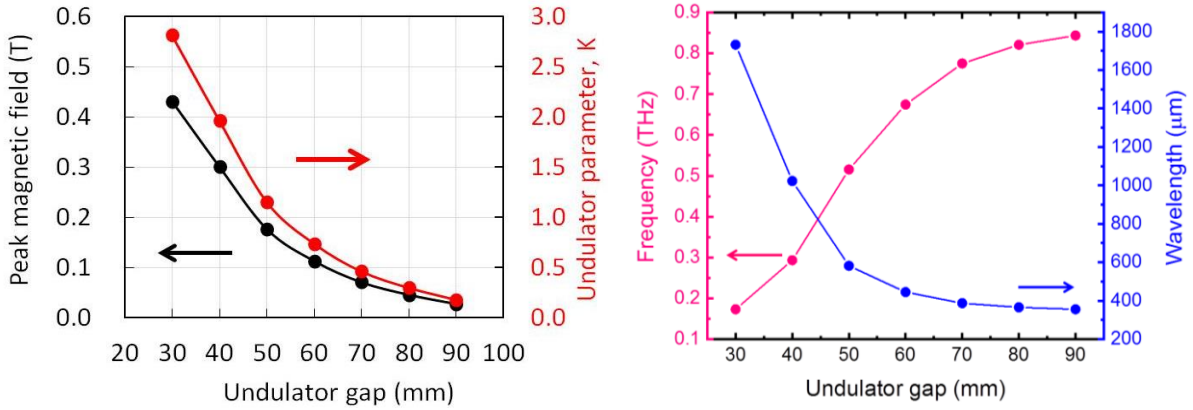

Figure 2.17: (left) Peak magnetic field and undulator parameter *K* and (right) the frequency and wavelength of undulator radiation by fixing the beam energy at 4.6 MeV.

According to the equation of motion, as mentioned above, it can be seen that the properties of the undulator magnetic field have a strong influence on the electron beam dynamics in low beam energy source since the undulator in this respect manifests itself as an additional quadrupole lens. Thus, accurate consideration of the undulator focusing properties is of great importance for understanding the electron beam dynamics in low beam energy source. As it is known that an electron beam is forced by the Lorentz force when passing through the insertion device, the electron beam displacement and angle deflection for the magnetic field in horizontal plane can be calculated by the magnetic field integral

$$y' = \frac{e}{\gamma m_0 c}\int_0^s B_x(s')ds' \qquad (2.52)$$

$$y = \frac{e}{\gamma m_0 c}\int_0^s ds' \int_0^{s'} B_x(s'')ds'' \tag{2.53}$$

where B_x is the magnetic field of undulator.

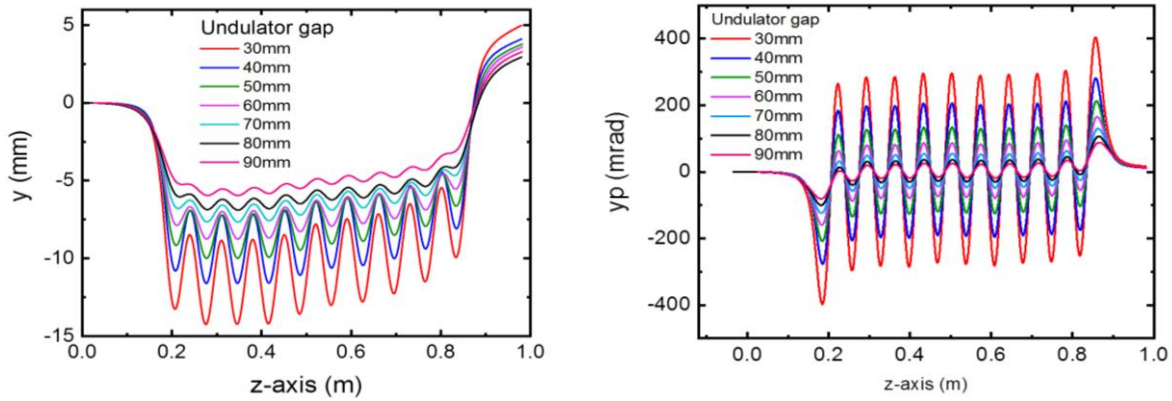

Figure 2.18: (left) Electron displacement and (right) electron angle along the undulator with the beam energy of 4.6 MeV.

On account of the magnetic field error of undulator, the electron beam is gradually kicked out from the ideal orbit and moves out the undulator with non-zero displacement as shown in Fig. 2.18. The electron displacement at the end of undulator is about 5 mm away from the center for the undulator gap of 30 mm. This orbit deviation for trajectory and angle can be corrected by steering magnets adjacent to undulator. The deflected angle and position of an electron beam at the exit were compensated for in both planes by steering magnets. Due to low electron energy, an electron trajectory has a large distortion. In actual machine, the misalignment of undulator could appear and result in the electron beam trajectory in the undulator. The schematic of electron motion inside the undulator is shown in Fig. 2.19.

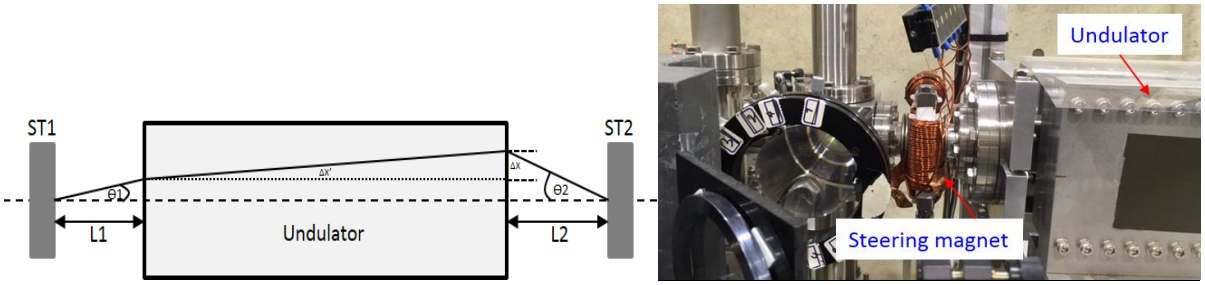

Figure 2.19: Layout of electron trajectory inside undulator and steering magnets upstream and downstream undulator.

The electron position shifted from the central orbit can be calculated from

$$\theta_1 = \frac{-(\Delta y + \Delta y' L_2)}{L_1} \tag{2.54}$$

$$\theta_2 = -(\theta_1 + \Delta y') \tag{2.55}$$

From Equations (2.54) and (2.55), the magnetic field of the steering magnet adjacent to the undulator used to correct the electron trajectory is simply calculated by

$$b = B\rho\theta / l_{\text{eff}} \tag{2.56}$$

where B is the magnetic field of steering magnet beside undulator, l_{eff} is the effective length of steering magnet.

2.7 Coherent Undulator Radiation

Coherence represents the degree of interference of undulator radiation. The emitted radiation is coherent when the electric fields from electrons typically interfere with high degree. For the case of incoherent radiation generation, the phase differences of electrons within the bunch are random. The comparison of incoherent and coherent radiation emitted from electrons is shown in Fig. 2.20. Regarding the coherent radiation, there are two types including temporal and spatial coherences. The coherent radiation can be emitted from electrons passing through a periodic field undulator under the condition that the electron bunch length must be equal or shorter than the radiation wavelength ($2\pi\sigma_z \leq \lambda_r$, σ_z is the rms bunch length). For the spatial coherent radiation, the transverse beam emittance (ε_{xy}) is equal or less than the diffraction-limited emittance of the photon, $\varepsilon_{xy} \leq \frac{\lambda_r}{4\pi}$, where λ_r is the radiation wavelength.

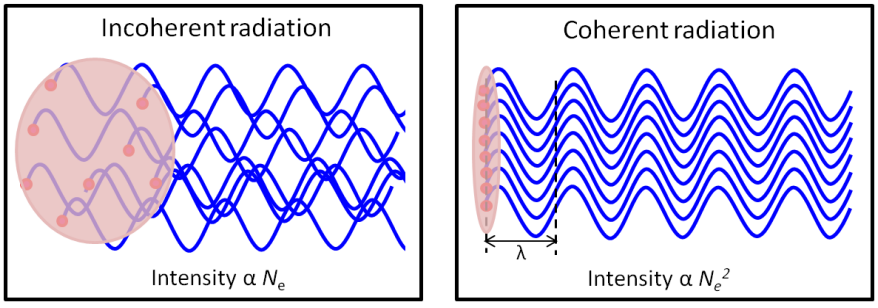

Figure 2.20: (left) Incoherent radiation and (right) coherent radiation.

In general, the energy density of spectral and spatial distribution of the radiation generated from electrons propagating through an undulator can be calculated from the Lienard-Wiechert potentials [17]. The electric field of the radiation described by Lienard-Wiechert potential with far-field approximation is given by [18]

$$\vec{E}(\vec{r},t) = -\frac{e}{4\pi\varepsilon_0}\left[\frac{\vec{n}-\vec{\beta}}{\gamma^2 R^2(1-\vec{n}\cdot\vec{\beta})^3} + \frac{\vec{n}\times\left\{(\vec{n}-\vec{\beta})-\vec{\beta}\right\}}{Rc(1-\vec{n}\cdot\vec{\beta})^3}\right] \tag{2.57}$$

The total energy when the electrons enter at times $t_j=z_j/c$, can be written as

$$\vec{E}_{tot}(\vec{k}) = \vec{E}_{1e}(\vec{k})\sum_{j=1}^{N_e} e^{i\vec{k}\cdot\vec{r}_j} \tag{2.58}$$

where $\vec{r}_j = \vec{r}_{j\perp} + z_j\hat{z}$ locates the j-th electron with respect to the first electron. The radiated power is proportional to the square of the field given by

$$P_{tot}(\vec{k}) = P_{1e}(\vec{k})\left|\sum_{j=1}^{N_e} e^{i\vec{k}\cdot\vec{r}_j}\right|^2 \tag{2.59}$$

A probability distribution $S(\vec{r})$ for the charge density of the electron bunch is defined by $1 = \int S(\vec{r})d^3r$ so the radiation power becomes

$$P_{tot}(\vec{k}) = P_{1\mathrm{e}}(\vec{k})N_e^2\left|\int S(\vec{r})e^{i\vec{k}\cdot\vec{r}_j}d^3r\right|^2 \tag{2.60}$$

Where $P_{1\mathrm{e}}$ is the power radiation of single electron, and the term of $\left|\int S(\vec{r})e^{i\vec{k}\cdot\vec{r}_j}d^3r\right|^2$ is known as the bunch form factor.

For coherent radiation, the three-dimensional bunch form factor can be defined as the square of the 3D Fourier transform of the normalized longitudinal particle density distribution, given by [19]

$$f(\vec{k}) = \left|\int S_{3d}(\vec{r})e^{i\vec{k}\cdot\vec{r}_j}d^3r\right|^2 \tag{2.61}$$

where $\vec{k}$ is the wave vector of the observation point. The normalized three-dimensional particle distribution is given by

$$S_{3d}(\vec{r}) = \frac{1}{N}\left\langle\sum_{i=1}^{N}\delta(\vec{r}-\vec{r}_i)\right\rangle \tag{2.62}$$

Here N is the total number of particles. It is convenient to recast, given by

$$S_{3d}(x,y,z) = \frac{1}{2\pi\sigma_{xy}^2} e^{-\frac{x^2+y^2}{2\sigma_{xy}^2}} \frac{1}{\sqrt{2\pi}\sigma_z} e^{-\frac{z^2}{2\sigma_z^2}} \quad (2.63)$$

Thus the bunch form factor becomes

$$f_{3d} = B_{3d}^2(k_x, k_y, k_z) = e^{-\sigma_z^2 k_z^2} e^{-\sigma_{x,y}^2(k_x^2+k_y^2)} \quad (2.64)$$

where $k_x^2 + k_y^2 = (\omega \sin\theta\,/c)^2$, $k_z = \omega \cos\theta\,/c$, ω is the angular radiation frequency, and θ is the observation angle of $1/\gamma$.

Taking into account only the z component of the wave vector, the longitudinal form factor becomes

$$f(\omega) = \int_{-\infty}^{\infty} S(z)\, e^{-i\omega z} dz \quad (2.65)$$

with the longitudinal particle distribution function, S(z).

For a Gaussian bunch, the bunch form factor (Fig. 2.21) can be convenient to recast in Eq. (2.66) [20]

$$f(\omega, \sigma) = \exp(-\omega^2\sigma^2) \quad (2.66)$$

Here σ is the RMS longitudinal bunch length and ω is angular frequency.

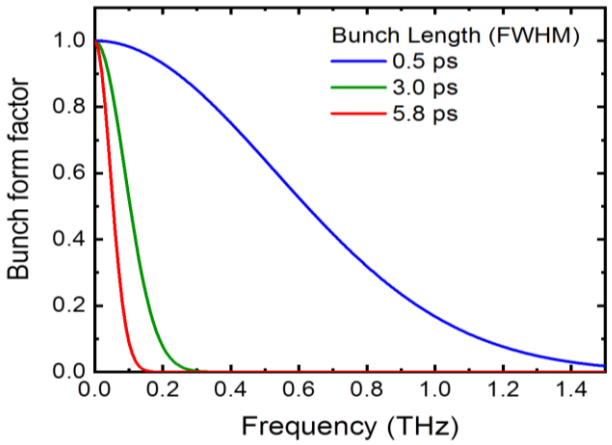

Figure 2.21: Longitudinal bunch form factor of three bunch lengths of 0.5 ps (compressed), 3.0 ps (uncompressed), and 5.8 ps-FWHM (at the beginning of RF gun).

The frequency spectrum of radiation from Fourier transform of radiation field is given by

$$\frac{d^2W}{d\omega d\varphi} = \varepsilon_0 \frac{c}{\pi} \left| \int_{-\infty}^{\infty} R(t)\vec{E}(t)\, e^{-i\omega t} dt \right|^2 \tag{2.67}$$

The spectral influence of the total emission energy from electron bunch is illustrated in the form

$$\frac{d^2W}{d\omega d\varphi} = \left(\frac{d^2W}{d\omega d\varphi}\right)_{1e} \left(N_e + N_e(N_e - 1)\left|B_{3d}(\vec{k})\right|^2\right) \tag{2.68}$$

The energy spectral density on-axis radiation can be simply expressed as [19]

$$\frac{d^2W_n}{d\omega d\varphi} = \frac{Q^2 N_u^2 \gamma^2}{4\pi\varepsilon_0 c} \frac{K^2}{(1+K^2/2)^2} n^2 \left\{ \frac{sin\left[N_u \pi(\frac{\omega}{\omega_r} - n)\right]}{N_u \pi(\frac{\omega}{\omega_r} - n)} \right\}^2 JJ^2 \times f(\omega, \sigma) \tag{2.69}$$

where Q is the bunch charge, N_u is the number of undulator periods, γ is the Lorentz factor for the electron, ε_0 is the permittivity of free space, K is the undulator parameter, and the coherence enhancement factor, $f(\omega,\sigma)$ is a bunch form factor for the longitudinal distribution, JJ is the Bessel function of the undulator harmonics, given by

$$JJ = J_{\frac{n+1}{2}}(nK^2/(4+2K^2)) - J_{\frac{n-1}{2}}(nK^2/(4+2K^2)) \tag{2.70}$$

where n = 1, 3, 5... is the harmonic number.

Figure 2.22 shows the electric fields of undulator radiation in the case of coherent and incoherent radiation from a 10-period undulator corresponding to the cycle number of the emitted radiation. The frequency spectrum of the undulator radiation can be obtained by the Fourier transform of this field. The spectrum of undulator radiation consists of the first harmonic for the main components and the other harmonics at higher frequency. In a central cone, the radiation energy spectral density will have a narrow relative bandwidth of $\Delta\omega/\omega \sim 1/N_u$.

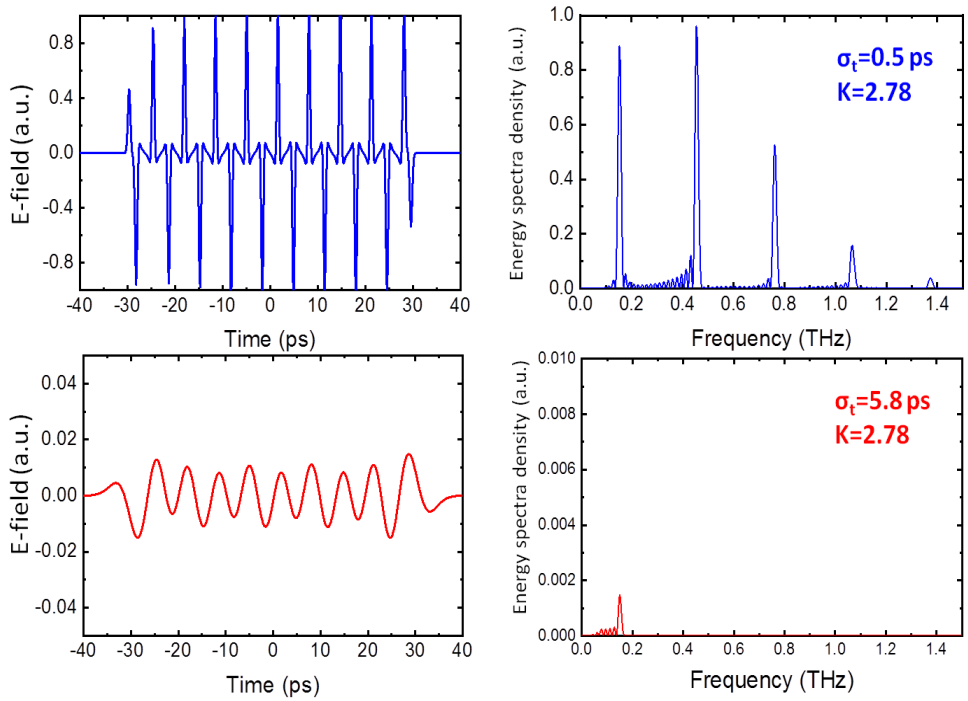

Figure 2.22: (left) Electric field and (right) energy spectral distribution of a 10-period undulator with the undulator field of 0.43 Tesla (30-mm gap).

Total energy of CUR for an ideal radiation emission

In general approach of the radiation characterization, total radiated energy consists of both incoherent and coherent radiations, and is defined as

$$W_{total} = W_{1e}\left[N_e + N_e(N_e - 1) f(\omega,\sigma)\right] \tag{2.71}$$

where W_{1e} is the radiated energy of a single electron, N_e is a number of electrons in a bunch, The bunch form factor, $f(\omega, \sigma)$ is defined as the Fourier transform of the longitudinal particle distribution within the bunch, ω is the resonance frequency, and σ is the longitudinal bunch length. The term corresponding to Coherent Undulator Radiation (CUR) is strongly enhanced by a square of electron number, N_e^2 dependence. The total energy of CUR for an ideal radiation emission is written as

$$W_{coh} = \frac{\pi e^2 N_u}{3\varepsilon_0 \lambda_u} K^2 \gamma^2 N_e{}^2 f(\omega,\sigma) \tag{2.72}$$

where N_u is number of undulator period, γ is the relativistic factor, K is the undulator strength parameter, and λ_u is the period length of undulator.

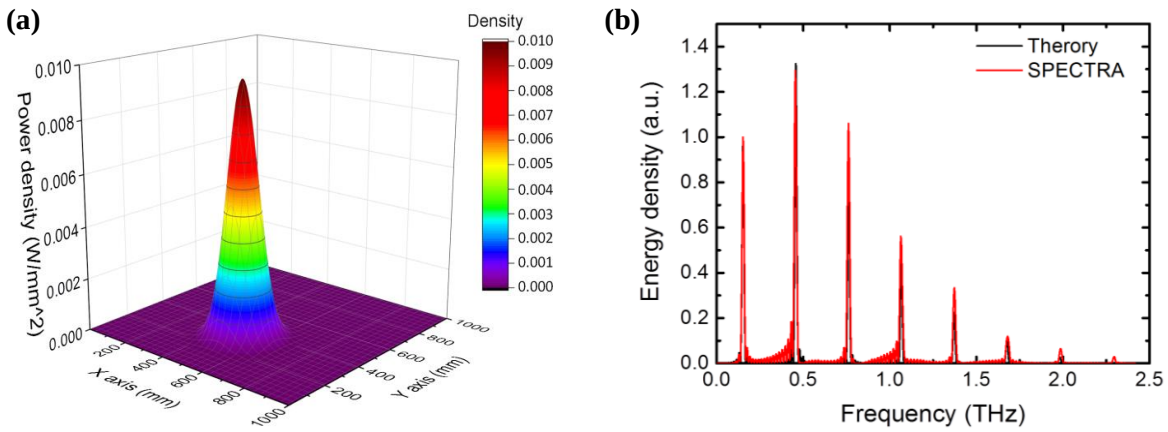

Figure 2.23: (a) Power density and (b) energy spectral density for an undulator field of 0.43 Tesla with bunch length of 0.2 ps-FWHM, energy spread of 0.1 %, and emittance of 0.1 mm-mrad [23].

Assuming the machine is operating under conditions of turn-off of the space-charge effect and other effects, the electron beam has a bunch length σ_t < 0.2 ps, energy spread $\delta\gamma/\gamma$ < 0.1%, and emittance ε < 0.1 mm-mrad. The prediction of the total radiation energy from Equation (2.68) may be up to several hundred μJ with the bunch charge of 160 pC and undulator field of 0.43 Tesla, corresponding to an efficiency conversion value of less than 40% of the electron bunch energy of 4.6 MeV. The power density from SRW code [21] is shown in Fig. 2.23(a). Figure 2.23(b) shows the calculated result for the energy spectral density, in comparison with that of a SPECTRA simulation [22] using the coherent radiation mode. Since the emission condition in SRW code is assumed to be incoherent, the radiation power is proportional to the number of electrons N_e. Therefore, the power density for coherent radiation can be estimated by converting the number of electrons to N_e^2. The calculation of the peak radiated power is in the megawatt (MW) class when the charge in the electron bunch increases to 160 pC. However, for the actual system, both known and unknown effects can disturb the generation of radiation, so a deep understanding of the effects involved is required. The phase error may perturb the radiation emission, and the effects of the electron beam parameters lead to broadening of the radiation spectrum and a reduction in radiation energy. The impacts of bunch lengthening, energy spread and emittance growth on the radiation properties must be observed for the enhancement of the radiation energy. This investigation can act as a guideline for improving the performance of a source further.

2.8 References

[1] J. S. Fraser, *et al.*, "High-Brightness Photoemitter Injector for Electron Accelerators", IEEE Transactions on Nuclear Science **32**(5), pp. 1791-1793 (1985).

[2] T. R. David and H. Dowell, "An engineering guide to photoinjectors", eds., published (2013), online available: http://arxiv.org/abs/1403.7539

[3] D. H. Dowell and J. F. Schmerge, "The quantum efficiency and thermal emittance of metal photocathodes", *Phys. Rev. Accel. Beams* **12**, 074201 (2009).

[4] G. Wang, *et al*., "Overcoming the quantum efficiency-lifetime tradeoff of photocathodes by coating with atomically thin two-dimensional nanomaterials", *npj 2D Materials and Applications* **17**, (2018).

[5] K. J. Kim, "RF and Space-Charge Effects in Laser-Driven RF Electron Guns", *Nucl. Instrum. Methods Phys. Res. A* **275**, pp. 201-218 (1989).

[6] A. Deshpande, *et al.*, "Experimental results of an rf gun and the generation of a multibunch beam", *Phys. Rev. Accel. Beams* **14**, 063501 (2011)

[7] J. Hong, *et al*., "High-power Beam Test of the Photocathode RF Gun at the Pohang Accelerator Laboratory", *J. Korean Phys. Soc.* **58**(2), pp. 198~204 (2011).

[8] S. Suphakul, "Development of Compact Accelerator-Based Terahertz Radiation Source at Kyoto University", PhD Thesis, Kyoto University (2017).

[9] C. Travier, "An introduction to photo-injector design", *Nucl. Instrum. Methods Phys. Res. A* 340, pp. 26-39 (1994).

[10] H. Zen, *et al*., "Development of photocathode drive laser system for rf guns in KU-FEL", in *Proc.* of FEL, Basel, Switzerland, THP045, pp. 828-831 (2014).

[11] H. Zen, *et al*., "Pulse duration measurement of pico-second DUV photocathode driving laser by autocorrelation technique using two-photon absorption in bulk material", in *Proc. of* FEL, Santa Fe, USA, WEP014, pp. 439-441 (2017).

[12] S. D. Mitri, "Bunch-length Compressors", *CERN Yellow Reports: School Proceedings* **1/2018**, CERN-2018-001-SP (2018).

[13] K. Kan, *et al*., "Effect of emittance and space charge in femtosecond bunch compression", *Nucl. Instrum. Methods A* **597**, pp. 126–131 (2008).

[14] P. Royer, "Solenoidal Optics", European Organization for Nuclear Research, CERN- PS Division Geneva, Switzerland (1999).

[15] "User manual version 3.2 General Particle Tracer", Pulsar Physics, NL-5614 BC Eindhoven, The Netherlands.

[16] N. Smolyakov, "Chapter 2: Motion of Electrons in Planar Ideal Undulator", Accelerator Physics-Radiation Safety and Applications, pp. 15-36 (2018).

[17] D. Bocek, "Generation and Characterization of Superradiant Undulator Radiatio", Thesis Stanford University (1997).

[18] L. D. Landau and E. M. Lifshitz, "The classical theory of fields", (4th Rev. English Ed.), Elsevier Ltd (1975).

[19] O. Grimm, *et al*., "Transverse electron beam size effect on the bunch profile determination with coherent radiation diagnostics", in *Proc.* of EPAC, Genoa, Italy, TUPC030 (2018).

[20] I. Nozawa, *et al.*, "Measurement of <20 fs bunch length using coherent transition radiation", *Phys. Rev. Accel. Beams* **17**, 072803 (2014).

[21] O. Chubar and P. Elleaume, "Accurate and efficient computation of synchrotron radiation in the near field region", in *Proc.* of the EPAC'98, Sweden, 22-26 June, pp. 1177-1179 (1998).

[22] T. Tanaka and H. Kitamura, "SPECTRA: a synchrotron radiation calculation code", *J. Synchrotron Radiation* **8**, 1221 (2001).

[23] S. Krainara, *et al.*, "Properties of THz Coherent Undulator Radiation (THz-CUR) at Kyoto University", *Review of scientific instruments*, Status: Publish after revisions (2019).

Chapter 3

Experiments and properties of THz-CUR at Kyoto University

The purposes of this study were to investigate in-depth the radiation properties and examine the influences of the phase error and the degradation of electron beam qualities on the generation of THz radiation. The results indicated that the bunch length, the energy spread, and the emittance were essential parameters in the reduction of the higher THz-CUR power. This opens the possibility of understanding in the generation of THz-CUR and has shed light on the enhancement of the radiation power. The specific THz application of the use of quasi-monochromatic THz-CUR is under consideration based on the characteristics of the THz radiation including the total radiated energy and frequency range. Section 3.1 describes the machine operation. The bunch charge measurement is explained in Section 3.2. Section 3.3 is devoted to presenting the experimental setup and the properties of THz-CUR from the measurement. The investigations of the phase error and the degradation of the electron beam qualities on the radiation spectrum and radiation power are presented and discussed in Section 3.4. Finally, our conclusions regarding the properties of THz-CUR and the effects on coherent radiation generated using a compact accelerator source developed at Kyoto University are given in Section 3.5.

3.1 Machine operation of THz-CUR source

The electron beam energy was fixed at 4.6 MeV with an RF power of 9 MW. The optimization of machine condition has been achieved by adjusting the injection phase, solenoid current, chicane field, and quadrupole magnets for reducing bunch length and increasing the quality of the electron beam to obtain the maximum intensity of the THz-CUR [1].

To minimize the transverse dimension of the electron beam, the solenoid current for the beam focus was adjusted from 80 to 120 A. The injection phase of the photocathode drive laser should be adjusted to 10.5 to 20 degrees to have a suitable longitudinal phase-space for the bunch compression. The current of chicane bunch compressor was scanned in between 5.55 A–5.85 A to obtain a short bunch length. Using triplet quadruples, the beam optics inside the undulator could be compensated by adjusting the quadruple currents between 0.5 A–0.9 A to obtain an optimum beam optic. Moreover, the magnetic field of steering components installed along beamline was also adjusted to align the electron beam. At each measurement condition, the electron beam optics and positions were optimized to have the maximum intensity of THz radiation. Figure 3.1 shows the dependences of THz-CUR energy and bunch charge as a function of phase injection with the use of laser energy of 30 μJ to illuminate the cathode. The maximum peak radiation energy occurs at the injection phase around 10–12 degrees. The solenoid current and chicane current were at 100 A and 5.8 A, respectively. The detail of the optimization will be explained in the next chapter.

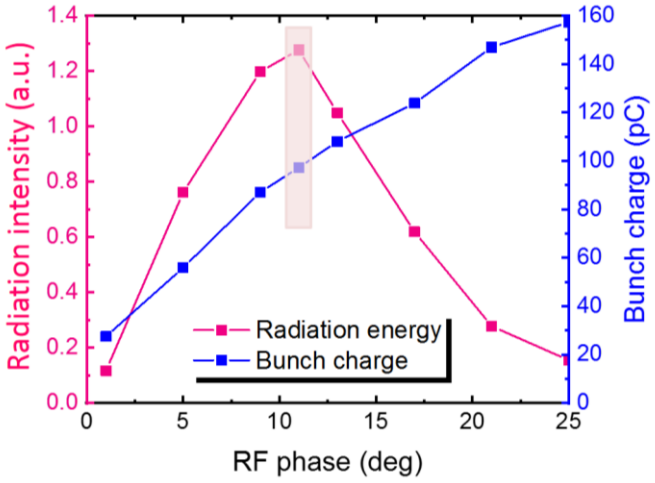

Figure 3.1: CUR Intensity vs. RF charge after compressing bunch length with laser energy of 45 μJ and the undulator gap of 30 mm for the bunch charge of 100 pC.

3.2 Bunch charge measurement

The bunch charge was measured by a cubic carbon employed as a Faraday cup. This Faraday cup is commonly used for particle charge measurement because of simplicity and reliability. The Faraday cup was made of a cubic carbon block with 10 cm to collect all charged particles and prevent scattering of particles. It was covered by a mylar tape to prevent loss of electrons. The property of carbon material is suitable for measuring the particle charge because it has a low atomic number to provide low backscattering electron. The total charge carried by the particles was collected and measured by connecting to an oscilloscope device via a coaxial cable. The schematic diagram of the bunch charge measurement by the Faraday cup is shown in Fig. 3.2. The relation between the measured voltage signal and the bunch charge can be expressed by [2]

$$Q = \int I(t)dt$$
$$= \frac{1}{R}\int V(t)\,dt \qquad (3.1)$$

where I (t) is the current signal, R is the impedance of the measurement system, and V(t) is the measured voltage by the oscilloscope.

The bunch charge was measured in the air after the electron bunch traveled through the extraction copper window of 0.2 mm thickness to a Faraday cup placed at the end of THz-CUR beamline. A current signal was detected and recorded by a 200 MHz oscilloscope (Iwatsu, DS-5624A) as shown in Fig. 3.2. The signals from the Faraday cup were monitored and integrated over time to obtain the bunch charge. In order to focus and monitor the electron beam before going to Faraday cup, the double quadrupole magnet and screen monitor have been installed at the end of the beamline. Figure 3.4(left) shows the measured result of the bunch charge at a laser energy of 30 μJ/pulse. The bunch charge was dependent on the injection phase. As a result, the bunch charge raises up to a maximum of 220 pC at the injection phase about 50 degrees. However, the injection phase also impacts on the longitudinal phase space for bunch compression. The bunch charge with a suitable phase for bunch compression could be generated only 80 pC when the cathode was excited by laser with the energy of 30 μJ/pulse. Figure 3.3(right) shows the relationship of the bunch charge as a function of laser energy at a suitable phase for bunch compression at the injection phase of 12 degrees approximately. The detail of RF phase adjustment for bunch compression will be presented in the next Chapter. In this measurement, the bunch charge was varied by

adjusting the laser energy excitation up to about 80 μJ in order to increase the bunch charge to 160 pC.

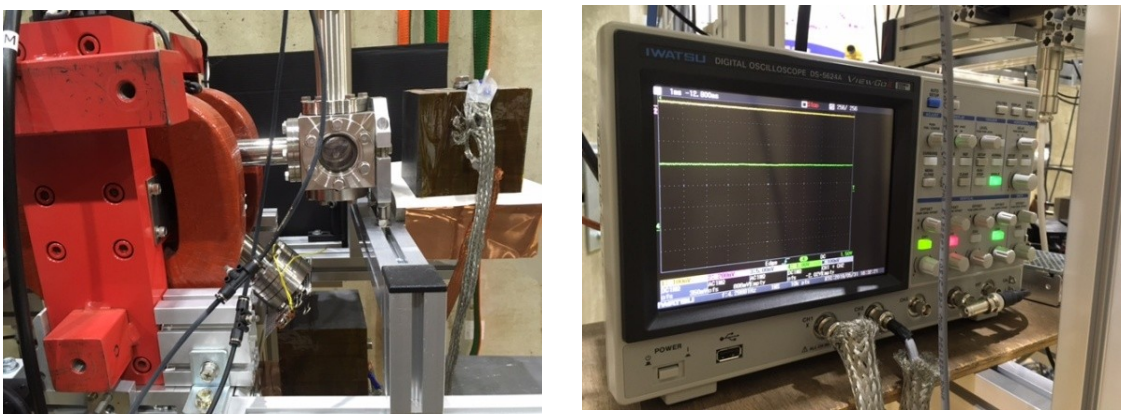

Figure 3.2: Schematic of Faraday cup for bunch charge measurement and oscilloscope for the signal monitor.

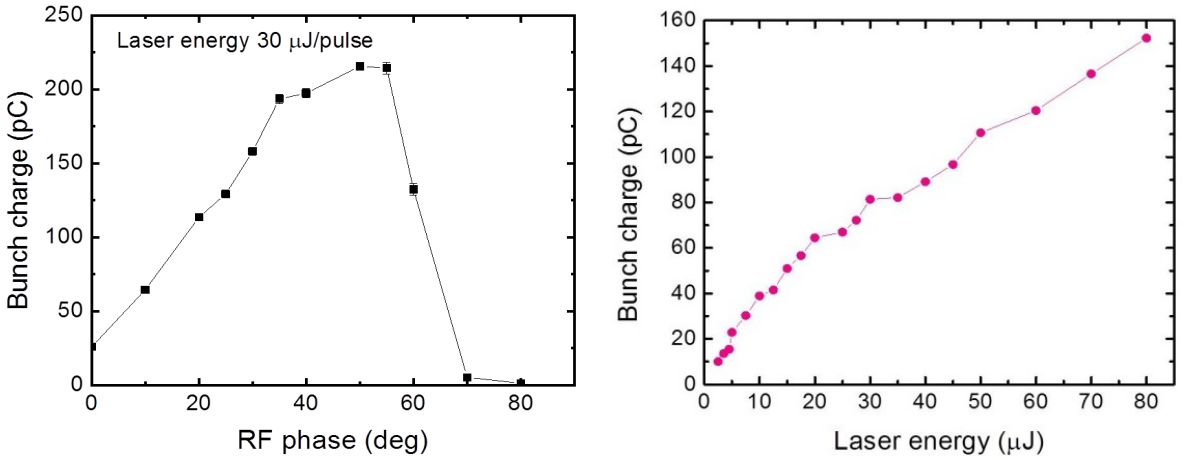

Figure 3.3: (left) Bunch charge as a function of RF phase using laser energy of 30 μJ/pulse and (right) laser energy vs. bunch charge at a suitable RF phase of about 12 degrees for bunch compression.

3.3 Measurements of THz-CUR

3.3.1 Experimental setups

The THz radiation was reflected by titanium foil of thickness 50 μm inside the vacuum chamber and then traveled through a fused silica window with transmission 75%. It was then sent to the experimental setup. All experiments were set up in the air because THz radiation in a range lower than 1.0 THz was not affected by atmospheric absorption. According to the

old experimental setup in Ref. [3], Teflon lenses were used to focus the radiation after passing through the THz window. Here, the focusing components were changed to the parabolic mirrors instead to avoid the intensity loss. In these measurements, two uncooled pyroelectric detectors (Fig. 3.4) were used to measure the characteristics of THz radiation. A pyroelectric detector is a thermal detector that converts the energy of a radiation pulse into a voltage using the pyroelectric effect. When the incident radiation illuminates on a pyroelectric crystal of detector, the crystal temperature changes then a polarization current is generated. The specifications of two detectors used in the measurement were summarized in Table 3.1. The detector was connected to a 1GHz oscilloscope (Tektronix, DPO4104) for monitoring the signal.

Figure 3.4: Detectors used in the experiments (left) pyroelectric detector PYD1/2, PHLUXi, Φ=1 mm and (right) THz10, Φ=10 mm.

Table 3.1: Specifications of pyroelectric detectors.

Detector	PYD1/2, PHLUXi	THz10
Sensor size	Φ=1 mm	Φ=10 mm
Frequency response	300 Hz	>500 Hz
Rise time	350 µs	100 µs
Sensitivity	12 MV/J (@1064 nm)	795 V/J
Gain adjustment	-	10, 100, 1000, 10,000
Maximum intensity	10 µJ	15 mW/cm²

(a) Power spectrum

In the real experiment, the production of coherent radiation from our source can be guaranteed by "Michelson interferometer" based on the interference of reflected radiations. The interference pattern can be observed by measuring the beam signal as a function the optical path difference of the two mirrors. The interference pattern is the superposition of the two separated beam for each wavelength. A diagram of the system is shown in Fig. 3.5.

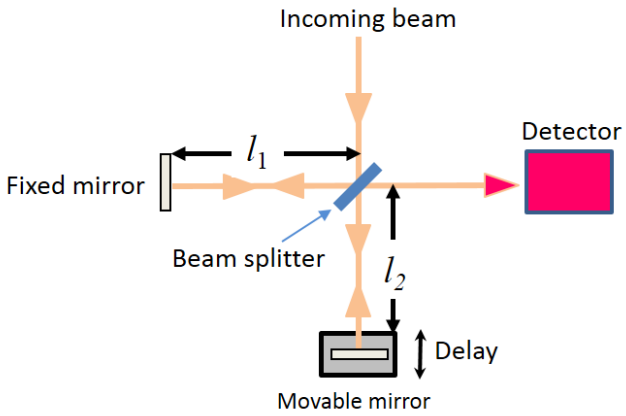

Figure 3.5: Layout of Michelson Interferometer.

The incident beam hits the beam splitter installed 45° respect to beam direction, and is divided into two beams. The beams are reflected from the mirrors and recombined at the beam splitter prior to be superposed to interfere with each other. The interference can be observed at the detector. The only difference between two beams is determined by the optical path difference of $\delta = 2l_2 - 2l_1$. When the two beams are in phase, maximum of the combined beam occurs at the same position ($\delta = 0$). The two beams are recombined with constructive interference and the amplitude of interferogram reaches the maximum. The signal amplitude becomes zero when the path difference is equal to the half wavelength ($\lambda/2$) of the incident light or is 180° out of phase for the destructive interference.

The electric field of combined beam is represented as [4]

$$\begin{aligned} E(t) &= E_{fix}(t) + E_{move}(t) \\ &= TRE(t) + RTE(t + \delta/c) \end{aligned} \tag{3.3}$$

where R and T refer to the reflection and transmission coefficients of the beam splitter, respectively.

The intensity of radiation from the Michelson interferometer is

$$I_a(\delta) \propto \int |TRE(t) + RTE^*(t+\delta/c)|^2 dt$$
$$= 2\int |RT|^2 E(t)E^*\left(t+\frac{\delta}{c}\right)dt + 2\int |RTE(t)|^2 dt \quad (3.4)$$

where *E(t)* is the electric field of light reflected from the fixed mirror and *E*(t+δ/c)* is the electric field of light reflected from movable mirrors, t is the time, δ is the path difference, and c is the speed of light.

The dependence of radiation intensity on the path difference called "interferogram" can be written in Equation (3.5)

$$I(\delta) \propto 2Re\int |RT|^2 E(t)E^*(t+\delta/c)dt \quad (3.5)$$

The interferogram can be converted to the power spectrum of the radiation by the fast Fourier transform (FFT).

$$I(\delta) = 2Re\int_{-\infty}^{+\infty} \left|R(\omega)T(\omega)\tilde{E}(\omega)\right|^2 e^{-i\omega\delta/c}d\omega \quad (3.6)$$

The power spectrum $I(\omega)$ becomes

$$I(\omega) = FT\{I(\delta)\}$$
$$\propto \left|R(\omega)T(\omega)\tilde{E}(\omega)\right|^2 \propto \int_{-\infty}^{+\infty} I(\delta)e^{i\omega\delta/c}d\,\delta \quad (3.7)$$

where $E(\omega)$ is the electric field in the frequency domain.

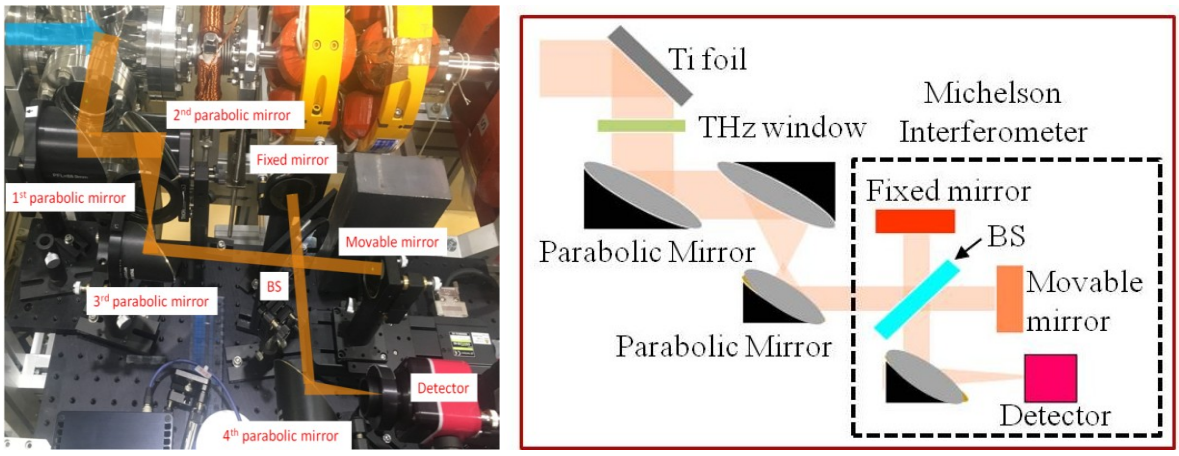

Figure 3.6: Experimental setup of the Michelson interferometer for power spectrum measurement (pyroelectric detector PYD1/2, PHLUXi, Φ=1 mm).

Figure 3.6 shows the experimental setup using to measure the power spectrum. A parabolic mirror with focal length 50 mm was placed downstream to create the parallel beam. The transported beam was then separated into two by a beam splitter (Inconel coated pellicle beam splitter, Edmund Optics). The reflected beam was injected to the fixed mirror and reflected back, while the transmitted beam was sent to a movable mirror on a linear stage and reflected back. Both beams were merged and focused by a fourth parabolic mirror before going to a detector. The detector used in this measurement was a pyroelectric detector (PYD-1/2, PHLUXi) equipped with a built-in lens. The detected signal was recorded by a 1 GHz oscilloscope (Tektronix, DPO4104). The signal of the intensity as a function of the path difference (interferogram) was measured and converted to a power spectrum using a fast Fourier transform (FFT). For the measurement of the interferogram signal, the movable mirror position was scanned with an optical path difference of ±2 cm and with an interference interval of 0.02 cm over three averaged measurements.

(b) Spatial distribution

The layout is presented in Fig. 3.7. We used two parabolic mirrors to focus the THz beam. The first parabolic mirror was used to make the beam parallel, and the second was used to focus the beam on the detector. Firstly, the spatial distribution was measured and scanned on the longitudinal axis to investigate the focusing point using a pyroelectric detector with a sensitivity diameter of 1 mm (PYD-1/2, PHLUXi) by removing the built-in lens. It was found that the focusing point was 68 mm from the second parabolic mirror. This distance was used to install the detector for the spatial distribution and the total radiation energy. In the measurement of spatial distribution, the detector was scanned or the signal was measured from −2 to 2 cm, with a step size of 0.2 cm.

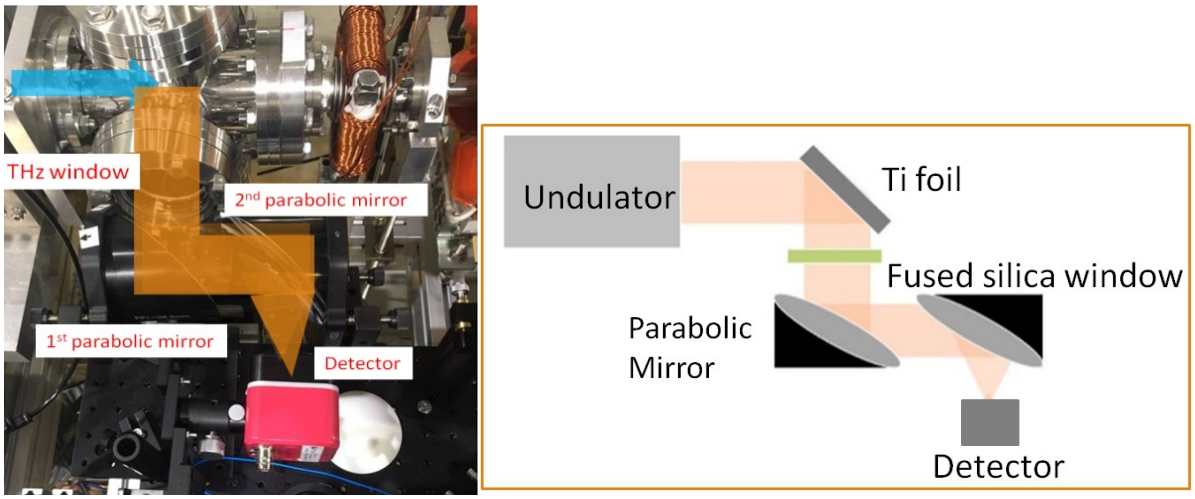

Figure 3.7: Experimental setup for spatial distribution (pyroelectric detector PYD1/2, PHLUXi, Φ=1 mm).

(c) Absolute radiation energy:

The focusing mirror was installed in the way same as the experimental setup of the spatial distribution, as shown in Fig. 3.8. The focal lengths of the first and second parabolic mirrors were 177.2 mm and 101.6 mm, respectively. In order to cover all of the radiation, a thin-film pyroelectric detector with diameter 1 cm (THz 10 and VPA amplifier module, Sensor und Lasertechnik) was located and fixed at the focusing point, 68 mm from the second parabolic mirror. The initial sensitivity of this detector was 795 V/J and a gain of 10,000 was used in this measurement, giving a detector sensitivity of 7.95 MV/J. The measured voltage signal can be converted to the absolute total radiation energy using

$$W_{tot} = \frac{(voltage)}{(sensitivity \times transmission \times overlap\ factor)} \quad (3.8)$$

where *voltage* refers to the measured voltage, *sensitivity* is the detector sensitivity, *transmission* is the window transmission of 75% for fused silica window, and *overlap factor* is the ratio of whole area and detector area.

The example of signal waveform detected is shown in Fig. 3.9. The range of signal waveform for the total intensity is in between two blue lines, which was considered only the peak of the radiation pulse.

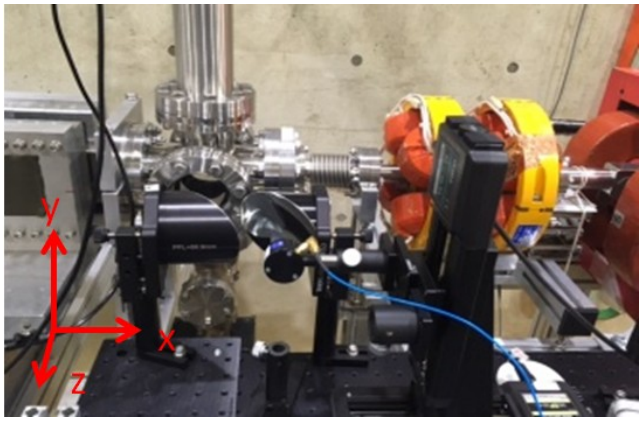

Figure 3.8: Experimental setup for total radiation energy (THz10, Φ=10 mm).

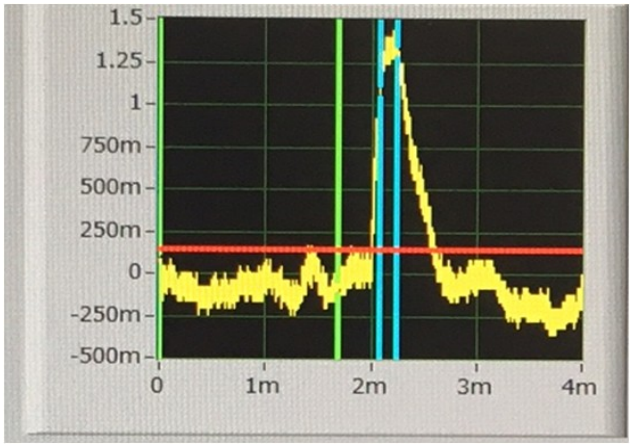

Figure 3.9: Signal waveform detected by THz10 and recorded from the oscilloscope.

3.3.2 Results and discussion

(a) Power spectrum

The intensity signals as a function of the path difference of two beams (known as interferograms) were measured by the Michelson interferometer. The dependence of the interferogram on the undulator gap was investigated and obtained using a path difference of ±2 cm with a step of 0.02 cm, as plotted in Fig. 3.11(left). The maximum intensity at the center of the interferogram was dependent on the bunch charge. According to the measured result, the interferograms contain the periodic interference pattern and correspond to the period number of the undulator, guaranteeing that coherent undulator radiation was generated from our source. The interferograms were then converted to THz-CUR power spectra, as illustrated in Fig. 3.11(right), using an FFT. By changing the gaps of the undulator from 30–

60 mm, THz-CUR with a 60 pC bunch charge can be produced in the center frequency range of 0.16–0.65 THz with a bandwidth (~1/N_u) of approximately 10%, where N_u is the number of undulator periods. It was found that the results of center frequency from measurement were shifted slightly from the calculated frequency. For example, at the undulator gap of 30 mm, the center frequency changed from 0.17 THz to 0.16 THz. It might be because of the discrepancy in beam energy, magnetic field of the undulator, or misalignment of experimental setup (Figure. 3.10). As seen the power spectrum from the undulator gap of 40 mm, the central frequency of the CUR was detected not only at 0.33 THz but also at 0.27 THz. From the measured signal of the 40 mm undulator gap, this seems to be superimposed with another pattern in the ranges -1 cm to -0.25 cm and 0.25 cm to 1 cm, as shown in the red circle in Fig. 3.11. This signal was obtained at a radiation frequency of 0.27 THz. The cause may be the reflection of radiation from the vacuum chamber. At other undulator gaps such as 35 mm, the reflection signal appears but it is at the same frequency as the main one as shown in Fig. 3.12. At a bunch charge of 160 pC, the THz-CUR power spectrum at 0.65 THz could not be observed because the signal was not strong enough to be detected. The center frequency was therefore between 0.16–0.51 THz, as shown in Fig. 3.11 (bottom right) for 160 pC bunch charge.

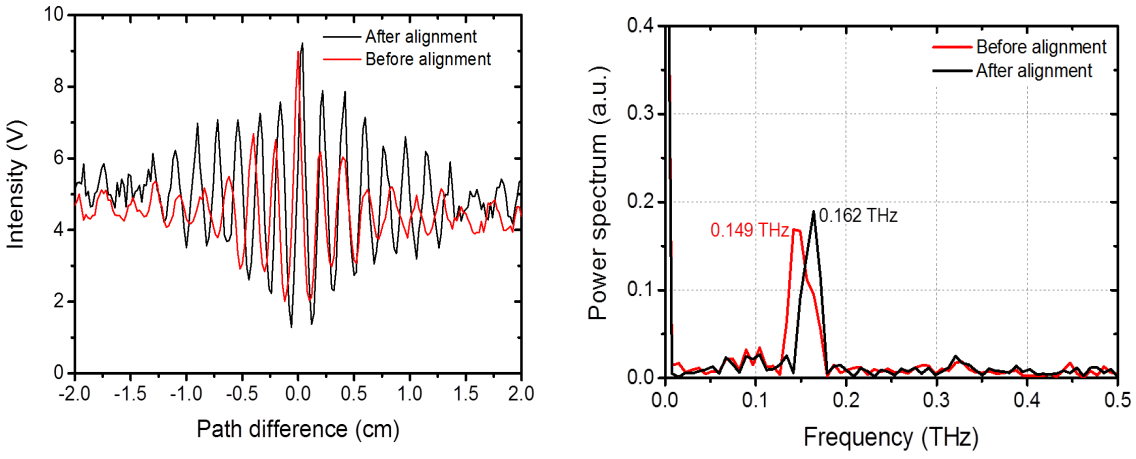

Figure 3.10: Comparison of power spectrum with and without good alignment.

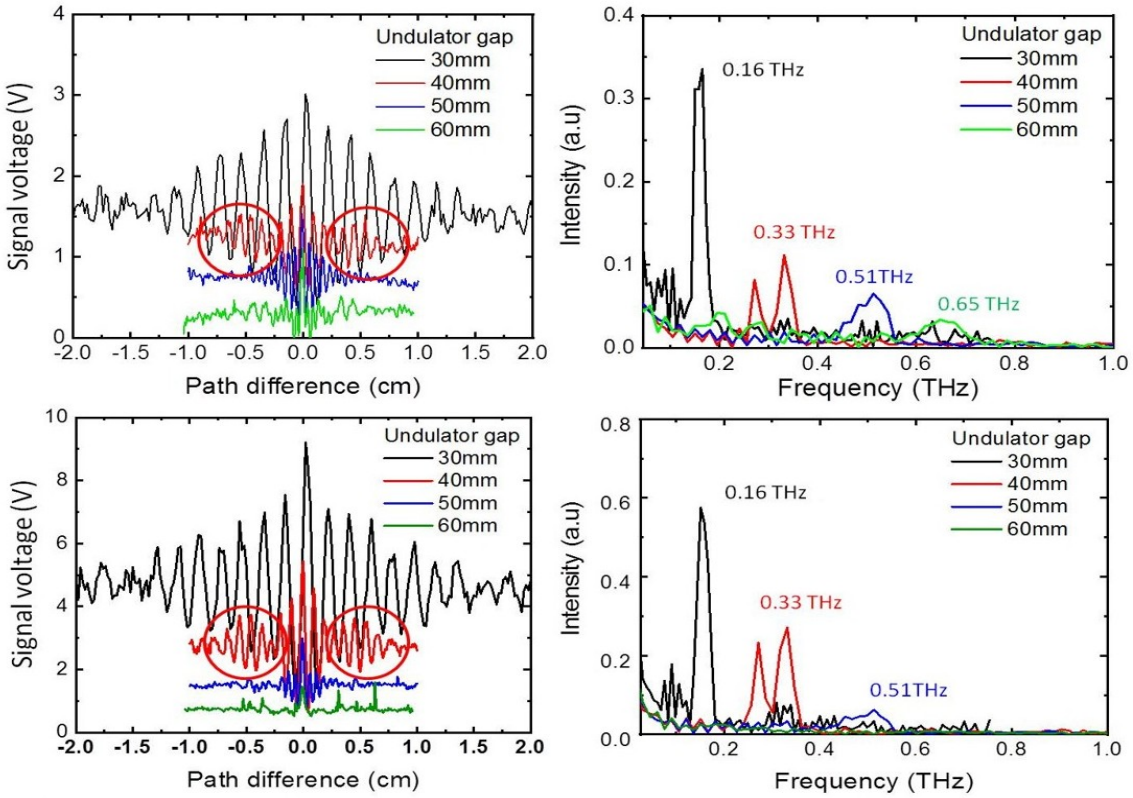

Figure 3.11: (left) Interferograms and (right) power spectra with a bunch charge of (top) 60 pC and (bottom) 160 pC at undulator gaps of 30, 40, 50 and 60 mm.

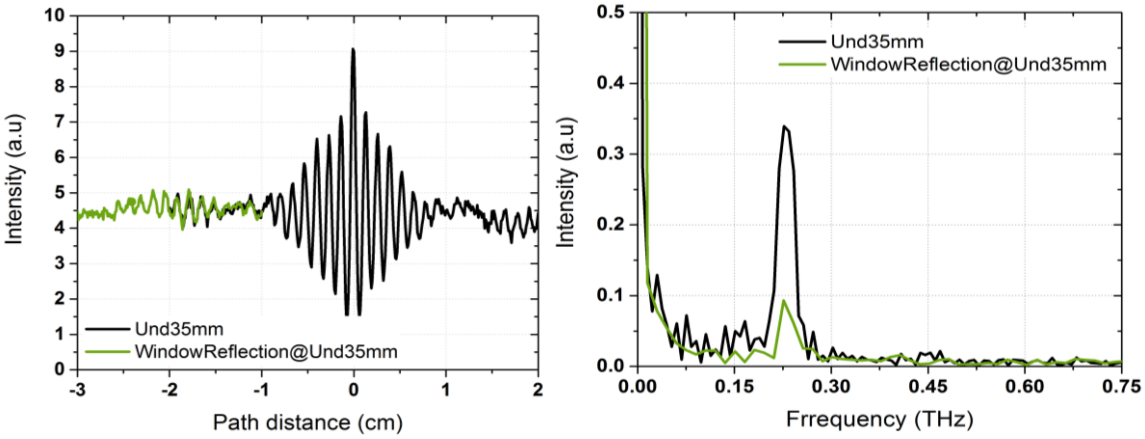

Figure 3.12: (left) Interferogram and (right) frequency spectrum indicated the vacuum chamber reflection at an undulator gap of 35 mm.

The dependence of the spectral intensity of CUR at a resonance frequency of 0.16–0.65 THz on the bunch charge is illustrated in Fig. 3.13. The spectral intensities were gradually reduced as the bunch charge increased to 160 pC for undulator gaps of 40, 50 and 60 mm, unlike for an undulator gap of 30 mm. However, the relationship between spectral intensity

and bunch charge at an undulator gap of 30 mm did not meet the quadratic function (a dashed black line) in the higher charge region. One likely cause of the spectral intensity was the bunch lengthening due to the space-charge effect, meaning that the electron bunch length could be not successfully compressed at a high bunch charge region. The effects on THz-CUR generation will be discussed in Section 3.4.

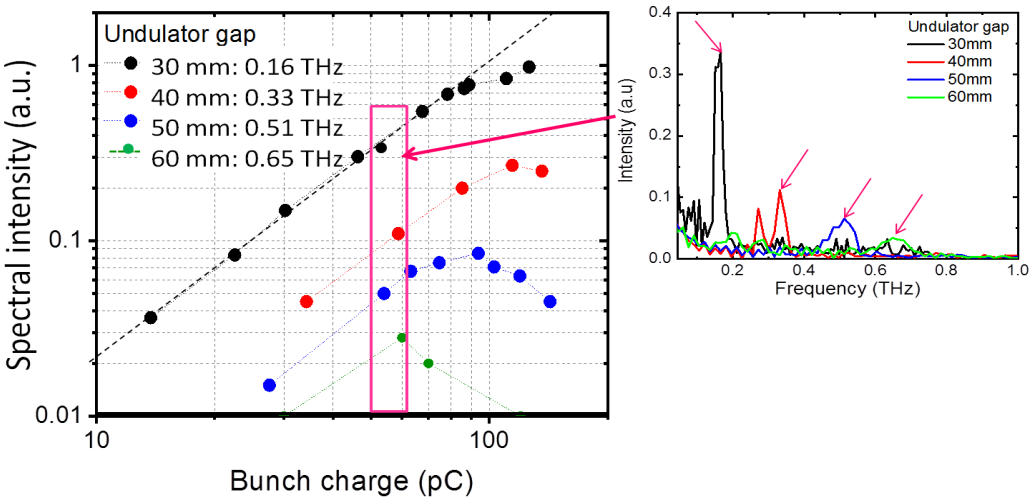

Fig. 3.13: Spectral intensity as a function of bunch charge for different undulator gaps (the pink box indicates the spectral intensity measured at a bunch charge of around 60 pC).

(b) Spatial distribution

Regarding the focusing point, the spatial distribution was measured in longitudinal position. Figure 3.14 shows the dependence of spatial distribution on the longitudinal distance from the second parabolic mirror. It was found that the focusing point is at a distance of 68 mm from the second parabolic mirror. Note that the radiation intensity was decreased by the factor of about 0.6 when installing the detector far away from the focusing point of about 3 cm. The results of the measurement of the spatial distribution are presented in Fig. 3.15 for different undulator gaps and bunch charges. The area of comparison between the THz10 detector and the THz beam is called the "overlap factor". This was determined by the ratio of integration of the measured distribution inside the 1 cm aperture in a white circle and the whole area obtained in the range of −2 cm to 2 cm. In case of an undulator gap of 30 mm and bunch charge 160 pC, the integrations of the detector signal were 0.9548 V·cm^2 and 1.9564 V·cm^2 for the 1 cm detector aperture and the whole area, respectively, giving an experimental result for the overlap factor of approximately 0.5. It is worth noting that around

half of the total radiation was measured by the calibrated THz10 detector at all undulator gaps and bunch charges.

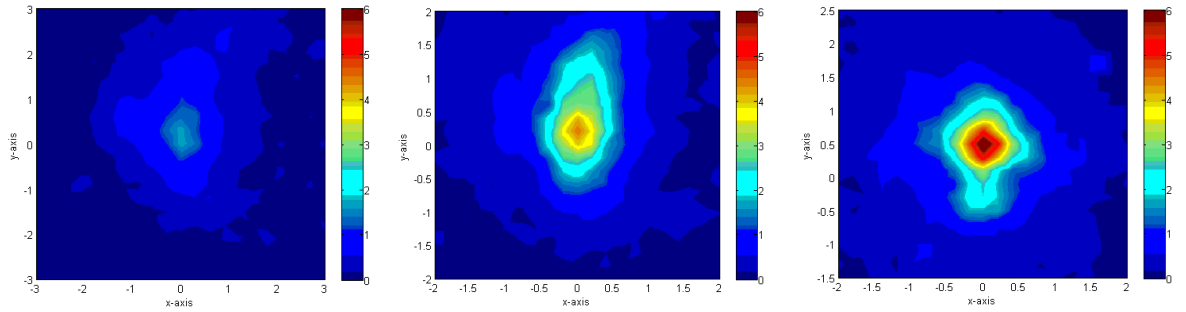

Figure 3.14: Spatial distribution at different distance from second parabolic mirror, 130 mm, 100 mm, and 68 mm (focusing point).

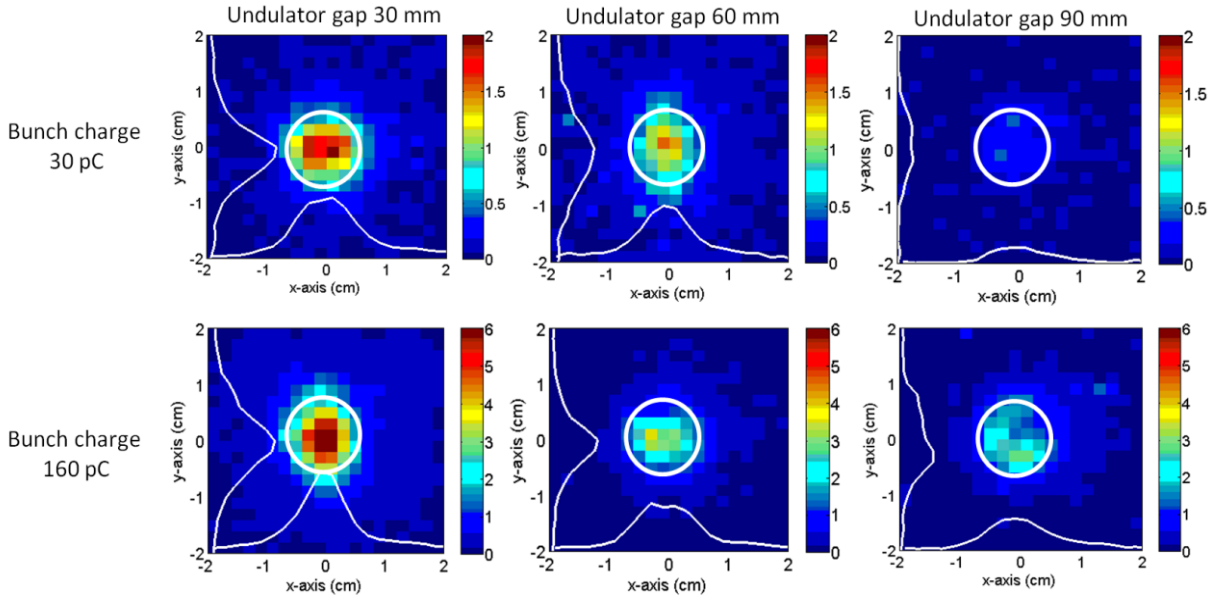

Figure 3.15: Spatial distribution with bunch charge of 30 pC and 160 pC at the undulator gaps of 30 mm, 60 mm, and 90 mm.

(c) Total radiation energy

The dependence of the total radiation energy on the bunch charge is shown in Fig. 3.16a for different undulator gaps. In fact, the coherent radiation intensity has a quadratic function dependence on the bunch charge or is proportional to the square of the number of electrons in the bunch. The results showed that the curves of the total radiation energy with bunch charge were a quadratic function prior to saturation. It was found that saturation obviously took

place when the bunch charge was higher than 80 pC and 50 pC for 0.16 THz and 0.65 THz, respectively. The saturation of radiation energy at a frequency of 0.65 THz occurred earlier than that at 0.16 THz. However, the total radiation energy at 0.16 THz was around 1.2 μJ at a bunch charge condition of 160 pC. Since the bunch form factor is proportional to the total radiation energy divided by the square of the bunch charge, $f(\omega,\sigma) \propto W_{coh}/Q^2$, the total radiation energy can be used to estimate the bunch form factor. It was found that the bunch form factor at 0.16 THz was slightly reduced from 1.0 to around 0.28 when the bunch charge was between 20–160 pC, as reported in [1]. The main cause of the saturation of total radiation energy in the higher charge region may result from the decrease in the bunch form factor or the bunch lengthening.

The properties of THz-CUR from an electron bunch generated in our experimental setup at Kyoto University are summarized in Table 3.2. The expected peak radiated power was calculated from the proportion of the total radiated energy and the radiation pulse width:

$$P_{peak} = \frac{W}{(N_u \lambda_r / c)} \tag{3.9}$$

where λ_r is the radiation wavelength calculated from $\lambda_u(1+K^2/2)/2\gamma^2$; c is the speed of light; and $(N_u\lambda_r/c)$ is the slippage time or the radiation pulse width.

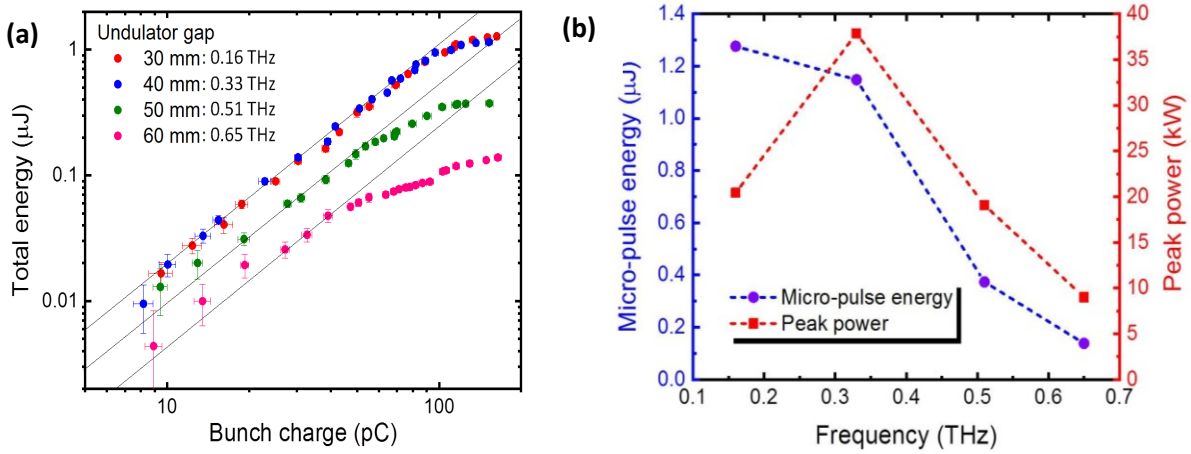

Figure 3.16: (a) Total radiation energy as a function of the bunch charge and undulator gap; and (b) radiation energy in the micropulse and the peak radiated power.

In doing so, the peak radiated power at a frequency of 0.16 THz was evaluated to be higher than 20 kW in the micropulse on the assumption of a pulse duration of 10 cycles, as plotted in Fig. 3.16b. Figure 3.17 is the plot of the relationship between the center frequency of generated radiation and the undulator gap.

Table 3.2: Characteristics of THz-CUR generated in our setup

Parameters	Value
Frequency range	0.16–0.65 THz
Bandwidth type	quasi-monochromatic
Micro-pulse total energy	～1 μJ @ 0.16 THz with 160 pC
Micropulse duration	60 ps @ 0.16 THz
Peak radiated power	～20 kW @ 0.16 THz with 160 pC
Macropulse duration	2 μs
Macropulse power	～1 W

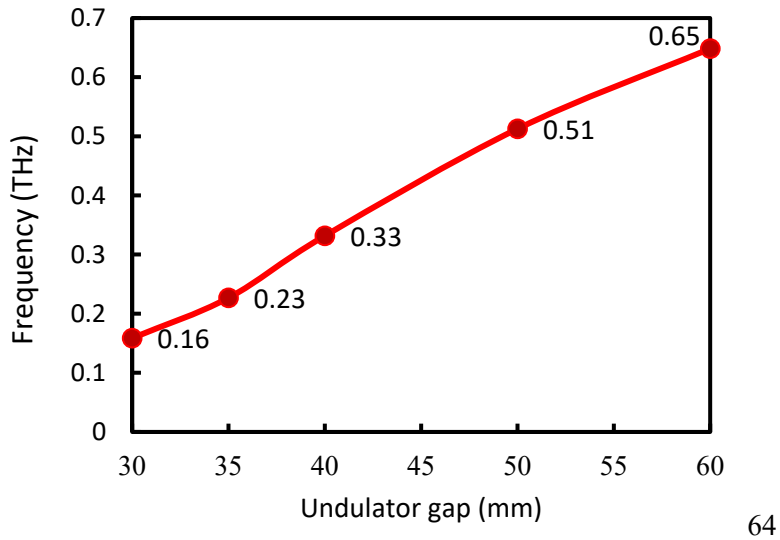

64

Figure 3.17: Resonance frequency of THz-CUR generated at Kyoto University.

3.4 Impacts of qualities of undulator and electron beam on the generation of THz-CUR

Based on the results presented above, we found the limitations of the generation of THz-CUR from our source. In order to improve the radiation properties and to enhance radiation power, we need to study the effects on the generation of THz-CUR as presented in this section.

3.4.1 Phase error from magnetic field error in an undulator

When an electron passes through the insertion device such as undulator, it is subjected to the Lorentz force, which can be explained in terms of the electron displacement and angle. The parameters such as the electron trajectory, the radiation phase, and the radiation intensity can be calculated directly from the measured magnetic field of the undulator. The magnetic field distribution of the undulator used in this calculation was measured by the Hall probe measurement method [3]. The maximum electron displacement and the angle for an undulator gap of 30 mm (max. field = 0.43 Tesla) were about 15 mm and 0.4 rad, respectively as shown in Fig. 2.18 of Chapter 2. Due to magnetic field error, it is possible to evaluate the reduction in radiation intensity. The imperfect field of the undulator can be represented in terms of the phase error. The function of the radiation phase, ϕ(z), can be calculated from the following equation [5]:

$$\phi(z) = \frac{2\pi}{\lambda}\left[\frac{z}{2\gamma^2} - \frac{\int x'^2 dz}{2}\right] \tag{3.10}$$

where λ is the wavelength and γ is the Lorentz factor. In the case of the vertical magnetic field, x' is the horizontal angle of electron motion defined in terms of the field integral, $x'(z) = \frac{e}{\gamma mc}\int_{-z}^{z} B_y(z)dz$, where B_y is the measured magnetic field of an undulator.

The phase error δ(z) of undulator was obtained from the difference of the phase radiation ϕ(z) between the measured and ideal magnetic fields. It is an important parameter that can affect the generation of undulator radiation. For an undulator gap of 30 mm, the RMS phase error was 11.5° or 0.20 rad, and this was gradually reduced to 2° when the gap was opened wider. The reduction in the quality of the radiation spectral intensity due to the phase error can be written as the simple expression in Equation (3.11) [6]:

$$I = I_{ideal}\exp(-n^2\delta^2) \tag{3.11}$$

where I_{ideal} is the intensity calculated from the ideal field of the undulator; n is the harmonic number; and δ is the RMS phase error.

Figure 3.18 shows the comparison of the energy spectral density from SPECTRA [7] between using the ideal field and measured field, and the calculated result with the phase error of the undulator. For calculation, a bunch length of 0.5 ps-FWHM, an emittance of 0.5 mm-mrad and an energy spread of 1% were used to define the input parameters, since these were the target electron beam parameters of our source [3]. The energy spectral density calculated from the measured magnetic field of the undulator is in good agreement with the results calculated from the phase error. The calculated result of total radiation energy including the phase error is lower than that of the total radiation energy from the perfect field undulator approximately 20% for the overall frequency and only 5% at the fundamental frequency. As a result, the phase error has a negligible effect on radiation power at the fundamental frequency for our system.

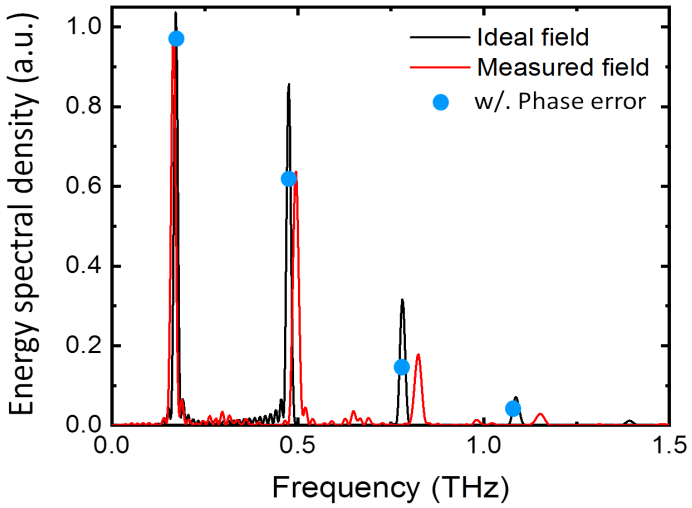

Figure 3.18: Energy spectral density for an undulator gap of 30 mm with a bunch length of 0.5 ps-FWHM, an energy spread of 1%, and an emittance of 0.5 mm-mrad.

3.4.2 Degradation of the qualities of an electron beam

In the observation of the properties of THz-CUR, the calculated result of the total radiated energy as presented in Section 3.2 was higher than the measured result of 1.2 μJ at a bunch charge of 160 pC. In order to study the properties of the radiation and to understand its

behavior, the reasons for the degradation of the electron beam qualities resulting from the space-charge effect, such as the bunch lengthening, the high energy spread, and the emittance growth, are needed to be investigated deeply.

In general, the radiation generated from relativistic electrons passing through a periodic magnetic field can be considered to be coherent when the electron bunch length is equal to or shorter than the radiation wavelength. The bunch length relating to the bunch form factor is one of the most important parameters in the generation of coherent radiation since it determines the degree of coherence and the interference spectrum. The bunch form factor considered here is given in Fig. 3.19(a). It consists of the bunch form factor calculated from the Gaussian bunch and the bunch form factor simulated using a general particle tracer (GPT) simulation [8], which was defined as the square of the Fourier transform of the longitudinal particle distribution. The energy spectral densities were calculated under the conditions of 1% energy spread, performed using a GPT at a bunch charge of 160 pC. Figure 3.19(b) shows the radiation energy dropped markedly on account of the low bunch form factor as the higher harmonic frequency was cut off. The radiation power could therefore be reduced by a factor of about three at 0.16 THz because the bunch form factor reduced from 1 to 0.28. However, the radiation power remained lower than expected, even when the bunch form factor reached its maximum value. In consequence, the emitted radiation could be affected by other parameters such as energy spread and emittance growth.

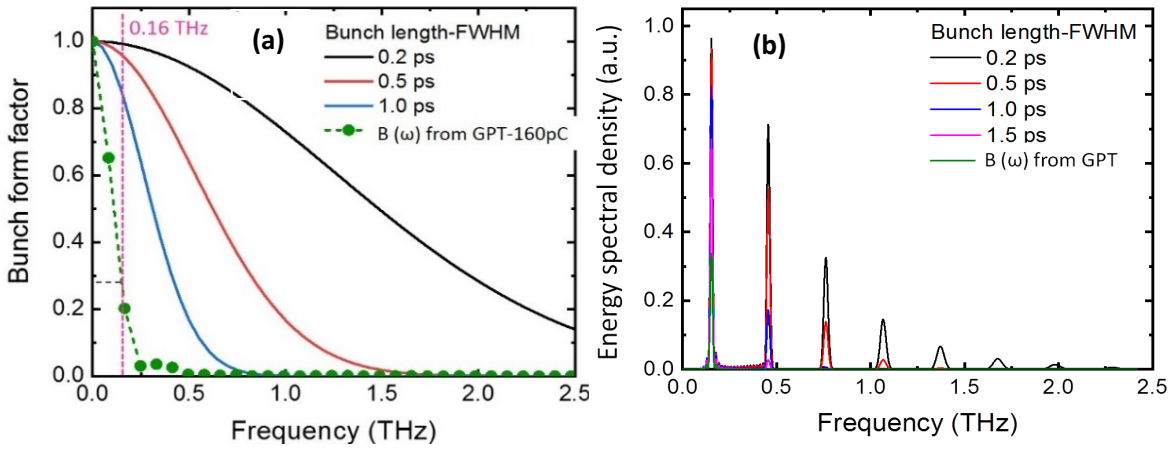

Figure 3.19: (a) Dependence of the longitudinal bunch form factor on bunch lengths at 160 pC; and (b) energy spectral density of an undulator gap of 30 mm with an energy spread of 1% as function of bunch length.

Consequently, it is necessary to discuss the impact of all of the effects of the electron bunch on the properties of the CUR. The energy spread and emittance growth can lead to broadening of the THz spectrum, and the peak radiated power will then be reduced in order to conserve the total power [9] since the relative frequency width $\delta\omega/\omega$ due to the energy spread $(\delta\gamma/\gamma)$ corresponds to [10]

$$\frac{\delta\omega}{\omega} = \frac{2\delta\gamma}{\gamma} \tag{3.12}$$

In order to give an indication of the effect of the energy spread on the radiation spectral energy, the bunch length, and the emittance were kept constant at 1 ps-FWHM and 0.5 mm-mrad, respectively. The results of the radiation power obtained from SPECTRA as a function of the energy spread at undulator gaps of 30 mm (0.16 THz) and 60 mm (0.65 THz) are plotted in Fig. 3.20(a) and Fig. 3.20(b), respectively. The energy spread simulated using a GPT simulation was 0.5% for the condition of turn-off of the space-charge effect but in the actual machine, the energy spread was between 2% and 3%. To cover the whole range of energy spread, the investigation in this study was carried out over the range of 0.5% and 5%. It was found that the radiation power depended on the energy spread, and decreased by about five as the energy spread increased from 0.5% to 5%. This large energy spread causes distortion in the generation of coherence radiation, which results in a loss of radiation power.

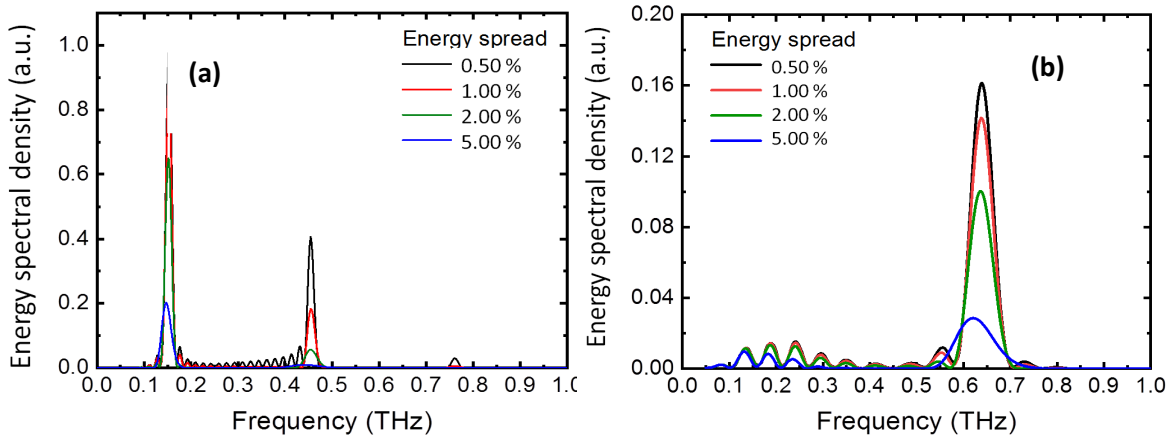

Figure 3.20: Energy spectral density for (a) an undulator gap of 30 mm (0.16 THz) and (b) an undulator gap of 60 mm (0.65 THz) simulated using SPECTRA with bunch length of 1 ps-FWHM as a function of energy spread.

Figure 3.21(a) shows the dependence of the radiation power at 0.16 THz on energy spread and bunch length. The radiation power was obtained from the energy spectral density, integrated over both frequency and angle at the fundamental frequency and divided by the slippage time. It is interesting to note that the radiation power from an energy spread of 0.5% was enhanced by a factor of about five over an energy spread of 5%, compared to the value of each bunch length. In the actual machine system with 5.8 ps-FWHM laser pulse width, the measured energy spread increased from 2% to 3% with an increase in the bunch charge from 20 to 160 pC [11]. With keeping the bunch charge constant at 160 pC, the radiation power could be increased by 40% when decreasing the energy spread from 3% to 2%.

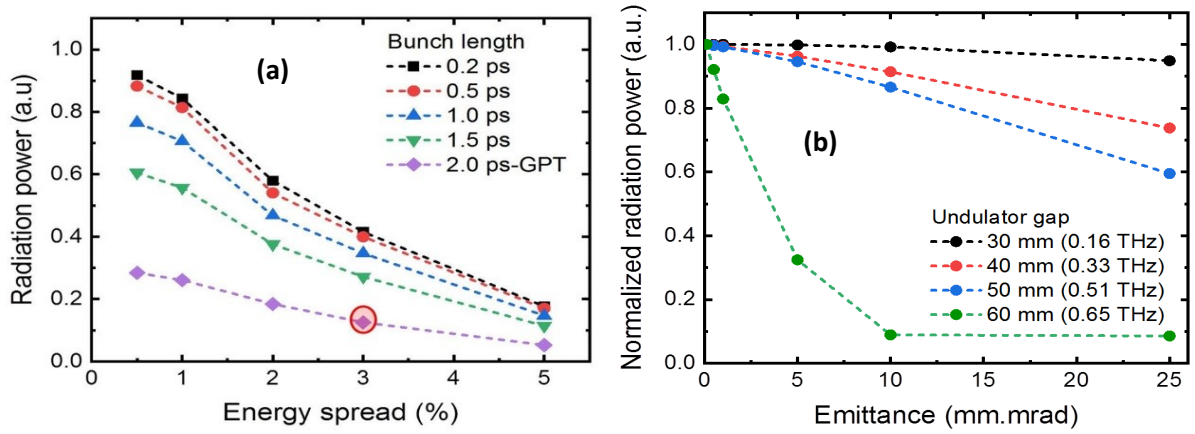

Figure 3.21: Radiation power at a bunch charge of 160 pC (a) as a function of energy spread ($\delta\gamma/\gamma$) of undulator gap of 30 mm (the red circle indicates the radiation power from the present condition of our machine) and (b) normalized radiation power as a function of the undulator gap and emittance at an energy spread of 0.5% with a bunch length of 1 ps-FWHM.

The properties of THz radiation were dependent not only on the bunch length and the energy spread but also the emittance. The transverse electron beam emittance must be equal to or less than the diffraction-limited of the photon beam, for the generation of spatial coherence radiation, given by

$$\varepsilon \leq \frac{\lambda_r}{4\pi} \tag{3.13}$$

where λ_r is the radiation wavelength.

The emittance can only disturb radiation at a higher frequency or shorter resonance wavelength. Figure 3.21(b) presents the dependency of radiation power at different

frequencies on the emittance obtained from the SPECTRA simulation. The results clearly showed that the emittance growth caused a significant reduction in the radiation power at a higher frequency (0.65 THz) but was almost unchanged at a lower frequency (0.16 THz). More specifically, the radiation power at a frequency of 0.65 THz dropped by a factor of about 3 as the bunch emittance increased from 0.1 to 10 mm-mrad. It is particularly important to keep the natural emittance to less than 1 mm-mrad to avoid a decrease in radiation power due to emittance at a frequency of between 0.16 and 0.65 THz.

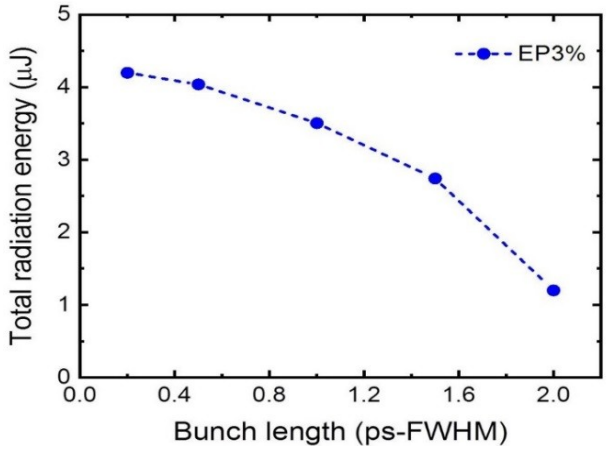

Figure 3.22: Radiation power at a frequency of 0.16 THz with bunch charge of 160 pC as a function of bunch length, an energy spread of 3% (from measurement), and natural emittance 0.5 mm-mrad.

By taking into account the qualities of the electron beam to evaluate the properties of the radiation, the dependence of the total radiation energy or peak radiated power on the electron beam parameters can be estimated based on the measured results. As shown by the measured results in Section 3.3, THz-CUR at a frequency of 0.16 THz can be generated with 1.2 μJ total radiation energy (about 20 kW peak radiated power) at 160 pC. The properties of the electron beam include a bunch form factor of 0.28 [1], estimated from the relation between the measured total radiation energy and the bunch charge, a measured energy spread of 3%, and the natural emittance of 0.5 mm-mrad. We then investigated the expectation of the radiation power, starting from the previously measured results.

Figure 3.22 shows the estimated result for radiation energy at different bunch lengths with 3% of the energy spread. If the bunch length can be compressed to 0.2 ps-FWHM, the radiation energy can reach approximately 4 μJ (～70 kW). In the case where the space-charge

effect is mitigated and the electron beam optics are optimized successfully, the total radiation energy can be increased up to 8 μJ (~140 kW peak radiated power) at a 0.2 ps-FWHM bunch length, an energy spread of less than 0.5% and 0.5 mm-mrad emittance, in the same way as turning off the space-charge effect.

In this study, it can be seen that the characteristics of CUR emitted from our source were judged based on the qualities of the electron beam. The first one was connected with the electron bunch length. The effect of emittance was negligible on the radiation power when the emittance was smaller than 1 mm-mrad. It is maintained that a high-quality electron beam (a short bunch length, low energy spread, and low emittance) is required to achieve an enhancement in the radiation power over the whole frequency range. To obtain high qualities of electron beam, one potential method is the manipulation of the transverse and longitudinal laser distribution, as reported in [12] for mitigating the space-charge effect.

3.5 Conclusions

THz-CUR from compressed electron bunch passing through a planar undulator is generated using a compact accelerator-based THz-CUR source developed at Kyoto University. This source can produce THz-CUR at 0.16 THz with a total radiation energy of 1.2 μJ and a peak radiated power of about 20 kW at a bunch charge of 160 pC. By controlling the undulator gap from 30 to 60 mm, the resonance frequency can be tuned to cover in the range between 0.16 to 0.65 THz with a relatively narrow 10% bandwidth at a 60 pC bunch charge. Through our measurements, we identified that the total radiation energy saturated in the higher charge region, and the power spectrum of THz-CUR at 0.65 THz frequency could not be observed under the condition of 160 pC bunch charge. In our source, the phase error obtained from the magnetic field error of undulator had no influence on the generation of THz-CUR at the fundamental frequency. The total radiation energy and peak power were limited by the space-charge effect in an electron bunch, which resulted in degradation of the qualities of the electron beam. This leads to broadening of the spectral width and a reduction in the peak power of the THz radiation. The mitigation of the space-charge effect and the optimization of beam optics to obtain a high-quality electron beam were indispensable in generating THz-CUR with a higher power. Using the electron beam parameters of $\sigma_z < 0.2$ ps-FWHM, $\delta\gamma/\gamma < 0.5\%$ and $\varepsilon < 0.5$ mm-mrad, the peak power with 160 pC bunch charge could be increased to more than 100 kW at a radiation frequency of 0.16 THz.

The chapter reported in the journal and proceeding as follows

1. S. Krainara *et al.*, "Properties of THz Coherent Undulator Radiation (THz-CUR) at Kyoto University", *Review of scientific instruments,* Status: *Publish after revision.*
2. S. Krainara *et al*., "Observation of THz radiation from THz Coherent Undulator Radiation Source", in *Proc.* of AESJ annual meeting, Hokkaido, Japan (2017).
3. S. Krainara *et al*., "THz coherent undulator radiation generated from compact accelerator based on photocathode RF gun", in *Proc.* of PASJ, WEOM02, (2017).

3.6 References

[1] S. Krainara, *et al*., "Development of compact THz coherent undulator radiation source at Kyoto University", in *Proc.* of FEL'17, USA, 20-25 Aug, pp 158-161 (2017).

[2] K. Damminsek, *et al*., "Electron Beam Properties from a Compact Seeded Terahertz FEL Amplifier at Kyoto University", in *Proc.* of FEL'15, Korea, 23–28 Aug, MOP025, pp. 85-88 (2015).

[3] S. Suphakul, "Development of Compact Accelerator-Based Terahertz Radiation Source at Kyoto University", Ph.D. Thesis Kyoto University (2017).

[4] C. Settakorn, "Generation and Use of Coherent Transition Radiation from Short Electron Bunches", Ph.D. Thesis, Stanford University, (2001).

[5] R. P. Walker, "Phase errors and their effect on undulator radiation properties", *Phys. Rev. Accel. Beams* **16**, 010704 (2013).

[6] R. P. Walker, "High-performance pure permanent-magnet undulators", *Nucl. Instrum. Methods Phys. Res., Sect. A* **335**, 328 (1993).

[7] T. Tanaka and H. Kitamura, SPECTRA version 10 .1.3, J. Synchrotron Radiation 8, 1221 (2001).

[8] S. B. van der Geer, *et al.*, "General Particle Tracer: A 3D code for accelerator and beam line design", in *Proc.* of EPAC'96, THP18F (1996).

[9] R. Chulkova, *et al*., "Effects of emittance and energy spread in an electron bunch on THz radiation generated by a superradiant source", FREIA Report 2014/02, pp.1-14 (2014).

[10] M. Gehlot and G. Mishra, "Effect of beam energy spread on cascade optical klystron undulator radiation", *Opt. Commun.* **283**, 1445 (2010).

[11] S. Krainara, *et al*., "Study of the saturation of radiation energy caused by the space charge effect in a compact THz coherent radiation source", *J. Phys.: Conf. Ser.* **1067**, 032022 (2018).

[12] S. Krainara, *et al*., "Manipulation of laser distribution to mitigate the space-charge effect for improving the performance of a THz Coherent Undulator Radiation source", *Particles* **1**(1), pp. 238-252 (2018).

Chapter 4

Study of electron beam characteristics under the influence of space-charge force

As the results presented in Chapter 3, saturation of total radiation energy occurred when the bunch charge was higher than 80 pC. It was found that the total energy of micro-pulse is not only saturated when reaching to high bunch charge, but also the CUR spectrum at the frequency above 0.65 THz could not be observed. It may cause from the space-charge effect resulting in the degradation of the electron beam quality (e.g. bunch lengthening, beam optics, energy spread). In order to better understand the electron beam behavior under the influence of space-charge force, the electron beam properties have to be investigated.

4.1 Space-charge effect

Although the photocathode RF gun is an excellent electron source, generating high brightness electron bunch, it is well-known that space-charge effect dominates for high bunch charge in the low-energy region. The space-charge occurs when the electrons interact with self-fields at the cathode surface. Each electron interacts inside the bunch with each other one and also subjects to the electric and magnetic fields generated from all the other electrons in

the bunch. The self-fields distort the phase space distribution and introduce couplings between motions along the coordinate axes. The space-charge force strongly occurs in the high bunch charge region and scales as $1/\gamma^2$ [1, 2]. The space-charge force is represented in the form

$$\vec{F}_{sc}(\gamma,\vec{r}) \approx \frac{e}{\gamma^2}\vec{E}_{sc}(\vec{r}) = \frac{e}{\gamma^2}\frac{n_0}{4\pi\varepsilon_0}\vec{\epsilon}(\vec{r}) \tag{4.1}$$

where n_0 is the line density at the bunch center $\int \rho(x,y,0)dxdy$, ρ is the volume charge density, and $\vec{\epsilon}$ is a normalized space-charge field in the bunch. The charge density is considered in following expression [2]

$$\rho(r,z) = \frac{Q}{(\sqrt{2\pi})^3\sigma_z\sigma_r}e^{-z^2/2\sigma_z^2}e^{-r^2/2\sigma_r^2} \tag{4.2}$$

where σ_r is the standard deviation of the electron beam and σ_z is the longitudinal beam.
The calculation of radial electric field with charge distribution assumed as cylindrical symmetry is given by

$$E = \frac{1}{2\pi\varepsilon_0}\frac{Q}{\sqrt{2\pi}\sigma_z\sigma_r^2 r}e^{-\frac{z^2}{2\sigma_z^2}}\int_0^r e^{-r^2/2\sigma_r^2}rdr = \frac{1}{2\pi\varepsilon_0}\frac{Q}{\sqrt{2\pi}\sigma_z\sigma_r^2 r}e^{-\frac{z^2}{2\sigma_z^2}}\left[\frac{1-e^{-r^2/2\sigma_r^2}}{r}\right] \tag{4.3}$$

The force inside the electron bunch is written as follows

$$F = \frac{e}{2\pi\varepsilon_0\gamma^2}\frac{Q}{\sqrt{2\pi}\sigma_z}e^{-\frac{z^2}{2\sigma_z^2}}\left[\frac{1-e^{-r^2/2\sigma_r^2}}{r}\right] \tag{4.4}$$

where γ is the Lorentz factor for the electron and ε_0 is the permittivity of free space.

In a low-energy source, an electron bunch is easily perturbed by this force while the electron beam is not affected for $\gamma \to \infty$.

This force results in the emittance growth happening near the cathode surface. The emittance growth caused by space-charge force is of great importance at low energy. For a Gaussian beam, the emittance induced space-charge [1] can be written as

$$\varepsilon_{SC} = \frac{Q}{\sqrt{2\pi}\sigma_b}\frac{\pi\mu(A)}{4\alpha k I_A sin(\phi_0)} \tag{4.5}$$

where A is the parameters depending on σ_x/σ_b, σ_x is transverse beam size, σ_b is bunch length, I_A is the so-called Alfven current equal to 17000 A, Q is the total bunch charge, and μ factor

for Gaussian charge distribution is $1/(5+3A)$ and $1/(1+4.5A+2.9A^2)$ approximately given for transverse and longitudinal directions, respectively. In the case of a uniformly charged cylindrical shape, the space-charge factor μ is smaller than that for Gaussian distribution [2].

The space-charge induced emittance can be rewritten in the following equation

$$\varepsilon_{sc} = 3.76\times10^{3}\,\frac{Q\ (\mathrm{nC})}{E_0(\mathrm{MV/m})\left[2\sigma_x(\mathrm{mm})+\sigma_b(\mathrm{ps})\right]} \tag{4.6}$$

Normally, the linear space-charge force causing emittance growth can be compensated by solenoid field, which is used to focus the beam divergence variations and to compensate for the linear space-charge force but cannot for the non-linear space-charge force. In an actual device, a non-linear space-charge force appears and the emittance increases due to a non-uniform charge distribution. Easy way to observe the space-charge effect is to investigate longitudinal phase space or the emittance as a function of bunch charge. Figure 4.1 presents the longitudinal phase space disturbed by the space-charge force. This effect can affect to the longitudinal phase space and the energy chirp before bunch compression. Note that, the non-linear of energy chirp confines the bunch compression.

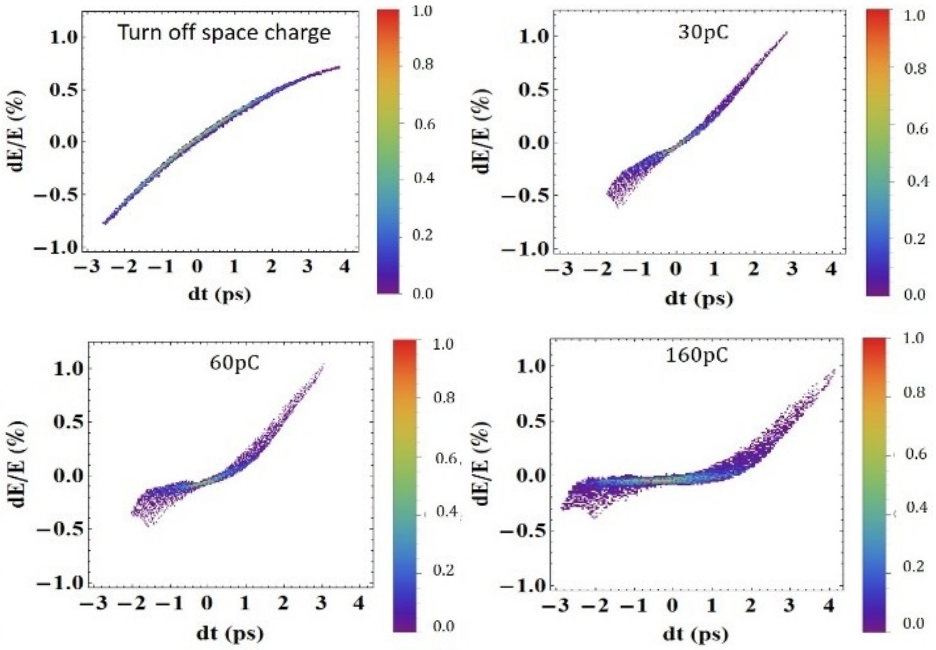

Figure 4.1: Longitudinal phase space before bunch compression.

4.2 Study of the saturation of radiation energy caused by the space-charge effect

In our machine, the laser pulse width of 5.8 ps-FWHM and transverse size of 0.5 mm-RMS were used to excite the cathode to generate electrons. As reported in Chapter 3, it was found that the THz-CUR energy in the micro-pulse at 0.16 THz had the quadratic dependence on the bunch charge prior to saturation. The THz-CUR energy gradually went to the saturation region when a bunch charge was higher than 80 pC and completely saturated at a bunch charge of higher than 110 pC [3].

According to the measured result of total radiation energy, we estimated the change of the bunch form factor. Normally, the bunch form factor is proportional to the total radiation energy divided by the square of the bunch charge, $f(\omega,\sigma) \propto W/Q^2$, where W is total radiation energy, Q is the bunch charge. Figure 4.2 presents the decreasing in the normalized value of bunch form factor with the increasing of bunch charge. It was found that the value of bunch form factor reduced promptly when the bunch charge was raised up more than 80 pC [4]. The result leads to bunch lengthening. In consequence, the dependence of the bunch length as a function of bunch charge is essential to be investigated in order to study and perceive the behavior of the electron beam in a short bunch.

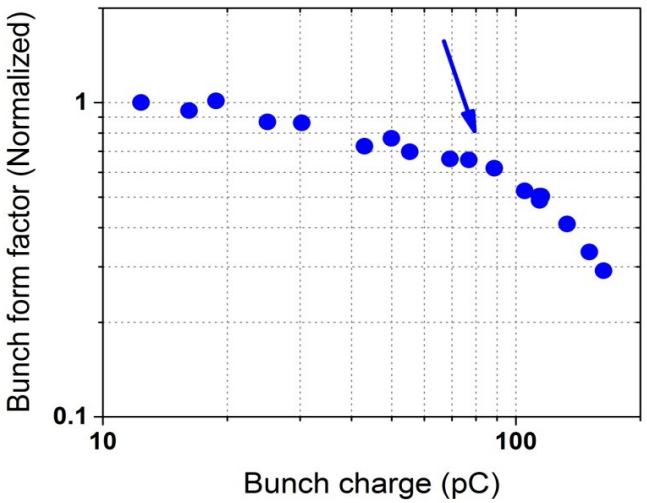

Figure 4.2: Bunch form factor estimated from the total radiation energy at the frequency of 0.16 THz.

In the next section, the dependence of a bunch length on a bunch charge performed by GPT simulation and compared with CTR and CUR experiments will be presented. Additionally, the investigations of electron beam size inside undulator and energy spread on bunch charge will be presented.

4.3 Electron beam properties

4.3.1 Bunch length estimation

For the coherent radiation, the bunch length is one of the most important parameters. The bunch length needs to be investigated as a function of bunch charge in order to study the space-charge disturbing an electron bunch. Although it is well known that the simulation is the best way to study, some unknown effects are not included. A direct way to measure the bunch length in the real measurement, a streak camera has been used in many electron beam accelerator facilities [5]. However, the price of the streak camera is high and the experimental setup is complicated. Therefore, to get the preliminary results of the bunch length measurements, we used CTR and CUR power spectra for estimating the bunch length. The bunch length was measured as a function of a bunch charge and compared with the result simulated by the General Particle Tracer (GPT) code.

4.3.1.1 General Particle Tracer (GPT) simulation

The General Particle Tracer (GPT) code is a particle tracking simulation employed to study the charged particle dynamics in electromagnetic fields [6]. This code is a powerful tool used for the design of accelerators and beamlines and it is suitable for studying the space-charge force in an electron beam. The effect of Coherent Synchrotron Radiation (CSR) is not included in GPT version 3.10 used in this work. The fifth order Rung-Kutta with adaptive step size control is used to solve the equation of motion for the macro-particles to be kept the minimum for more accurate computation. All particle interactions are calculated in the rest frame of the bunch, fully analogous to the "*spacecharge3D*" using the point-to-point method. The generated fields are directly from the relativistic particle-particle interaction. The number of macro-particles used in the simulation is 10,000 particles to be sufficient for 3D-model calculation for checking [7]. In GPT simulation, the space-charge is defined as the particles collective effect and governed by long-range interactions with charge density. The

calculation of Coulomb interactions are derived from the electric field with all particles *j* given by

$$\vec{E}_i = \sum_{j\neq 1} \frac{Q_j}{4\pi\varepsilon_0} \frac{\vec{r}_j - \vec{r}_i}{|\vec{r}_j - \vec{r}_i|^3} \tag{4.7}$$

where Q is the particle charge.

In order to check the condition of initial machine parameters, the simulation uses the "*spacecharge3Dmesh*" based on solving Poisson's equation in 3D in the rest frame of the bunch by dividing the total beam in N macro-particles. This is the fastest space-charge model. For calculating the all Coulomb interactions, *spacecharge3D* routine is the best mode for calculation.

New approach for beam dynamics optimization

The automatic optimum function in GPT simulation can be used as an optimizer to find a good solution; however, this function is not proper if the initial condition is far from the optimum point. Therefore, we applied new approach to find the initial machine parameters to optimize the electron beam parameters. It helps to understand the phenomena of the electron beam under the space-charge force. Figure 4.3 shows the optimal steps of simulation consisting of three main steps detailed as below. The steps of optimization consist of the calculation of space-charge factor, the suitable energy chirp, and compressed bunch length.

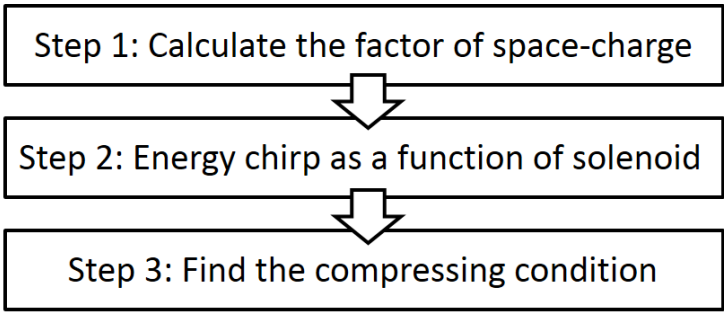

Figure 4.3: Diagram of optimization step.

Step 1: Space-charge factor:

Actually, total emittance defined at the gun exit is given in Equation (4.8) [8]

$$\varepsilon_{total} = \sqrt{\varepsilon_{rf}^2 + \varepsilon_{sc}^2 + \varepsilon_{th}^2} \tag{4.8}$$

where ε_{sc} is the space-charge force induced emittance, ε_{rf} is the linear RF-induced emittance, and ε_{th} is the thermal emittance. As mentioned in Chapter 2, the emittance only ε_{sc} is dependent on the bunch charge. Therefore, the emittance, ε can be re-written as

$$\varepsilon = \sqrt{(aQ)^2 + b^2} \tag{4.9}$$

where Q is bunch charge, a is a factor referred to the space-charge force, b is the other effects sum including the RF-induced emittance, the thermal emittance, etc.

From the above equation, we can use to estimate the space-charge factor in order to find the optimum condition. Laser pulse width referring to initial bunch length was fixed at 5.8 ps-FWHM in order to have the same RF induced emittance. The RF injection and solenoid current were scanned from 6° to 20° and the solenoid field from 0.07-0.13 Tesla (60,000-120,000 A-turns), respectively. As shown in Fig. 4.4, the emittance with solenoid field of 0.097 Tesla was simulated as the functions of RF phase and bunch charge. The bunch charge was in the range of 40-200 pC. The relation of emittance and bunch charge was fitted by Equation (4.4) to obtain the space-charge factor. Figure 4.5 shows the dependence of space-charge factor on RF phase and solenoid current. It was found that the optimal RF phase was different at each solenoid current. For example, the compensation of space-charge force with the solenoid current of 80,000 A-turns, the optimal RF phase has to be at 10.5 deg. Due to the effective bunch compression depending on longitudinal phase space, the energy chirp should be considered to obtain a suitable one before a chicane bunch compression.

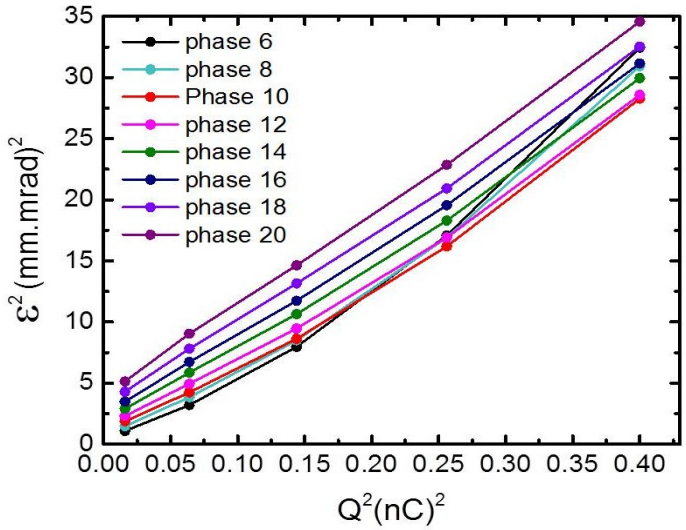

Figure 4.4: Dependence of Emittance with solenoid field of 0.097 Tesla at different RF phase and at bunch charge from 40 pC–200 pC.

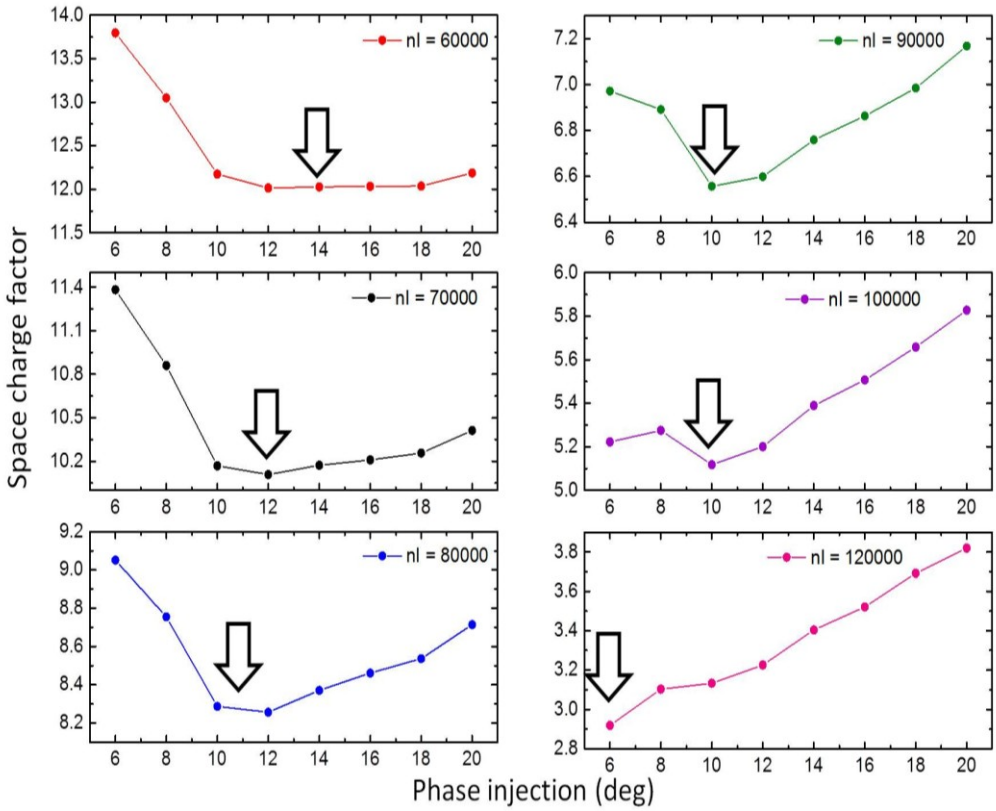

Figure 4.5: Space-charge factors before bunch compression at the different phase injection and solenoid current.

Step 2: Energy chirp before bunch compression:

An energy chirp at upstream chicane has a significant influence on the effective bunch compression. The energy chirp can defined by the relationship between the energy spread and electron position, $h = d\delta/cdt$. Due to the space-charge force in a short electron bunch, the rotation of longitudinal phase space happens because the beam's tail loses energy while the beam's head gains energy. The longitudinal phase space (Fig. 4.6) was calculated at the machine parameter of solenoid current from 60,000 A-turns – 100,000 A-turns with the optimal RF phase found in Step 1.

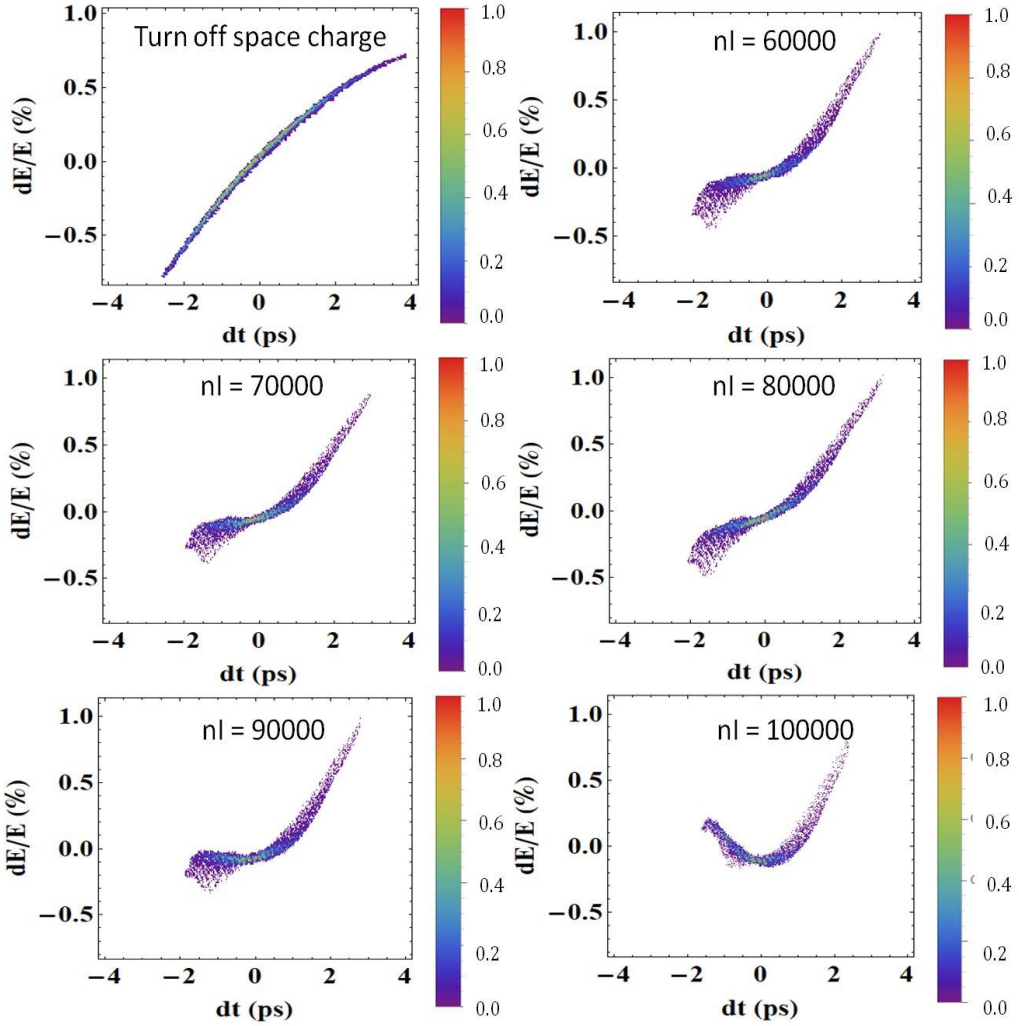

Figure 4.6: Longitudinal phase space at upstream chicane magnet with the bunch charge of 60 pC.

In case of turn-off space-charge, the energy chirp (h) was about 40 m^{-1} calculated from the longitudinal phase space of the case of turn off space-charge as shown in Fig. 4.6. This result of energy chirp is the most suitable value of bunch compression for our machine. Figure 4.7(left) shows the energy chirp calculated from longitudinal phase space as a function of the solenoid field with the optimal RF phase. It was found that the suitable energy chirp at upstream chicane bunch compressor with tuning on space-charge effect was about 30 m^{-1}. The parameters of the solenoid field and RF phase were 0.103 Tesla (85,000 A-turns) and RF phase of 10.5 deg. These machine parameters can be used as an initial parameter for optimization. At the other bunch charges, RF phase and solenoid were optimized by using automatic optimum function in GPT simulation. It was found that the RF phase of 12 degrees with the optimal solenoid field of 0.103 Tesla was proper for 160 pC bunch charge.

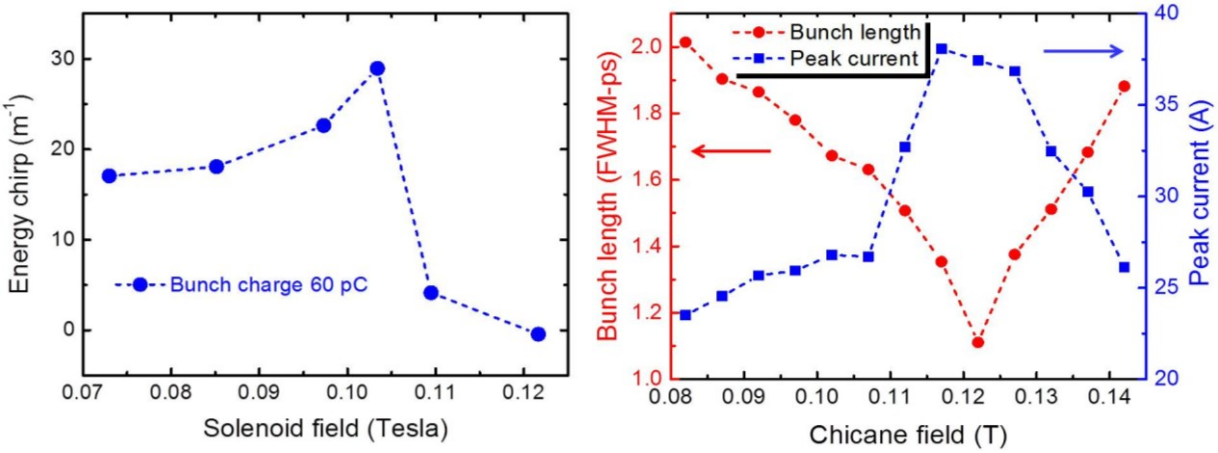

Figure 4.7: (left) Energy chirp as a function of solenoid field and (right) Bunch length with the bunch charge of 60 pC after compressing bunch length using solenoid of 0.103 Tesla and RF phase of 10.5 deg.

Step 3: Bunch compression by a chicane magnet:

To obtain a short electron bunch, the compressed bunch length was observed as a function of the magnetic field of chicane from 0.08 to 0.14 Tesla with fixed solenoid field and phase injection conducted from Step 2. In GPT simulation, the bunch length was calculated from the longitudinal distribution determined from the histogram of the peak current and then converted to bunch form factor by using fast Fourier transform (FFT). For Gaussian beam, the bunch form factor was fitted with $f(\omega,\sigma) = A\cdot\exp(-\omega^2\sigma^2)$ to get the effective bunch length. Figure 4.7(right) plots the effective bunch length and peak current versus magnetic field of the chicane. The best condition of the magnetic chicane for bunch

compression is at the magnetic chicane of 0.122 T referring to the bunch length of 1.11 ps-FWHM at the bunch charge of 60 pC.

Figure 4.8 shows the comparison of longitudinal phase space after bunch compression between 60 pC and 160 pC. In higher charge region, the electron bunch cannot be completely compressed by a chicane bunch compressor even the machine parameters were adjusted to the optimum point. As a result of GPT simulation, it is presumed that the bunch length at a high charge cannot be compressed by only adjusting the machine parameters. Figure 4.9 shows the dependence of the bunch length on the bunch charge. The bunch length increased by factor 3 approximately when increasing the bunch charge from 20 to 160 pC.

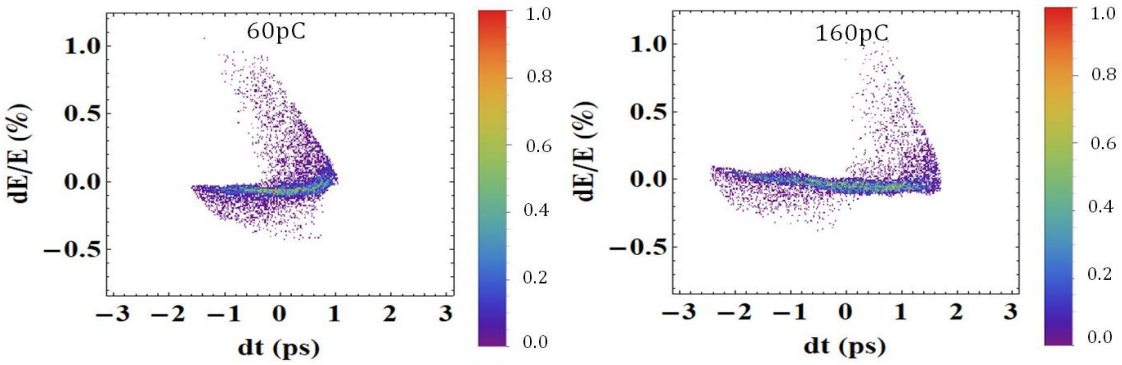

Figure 4.8: Energy–time phase space after bunch compression.

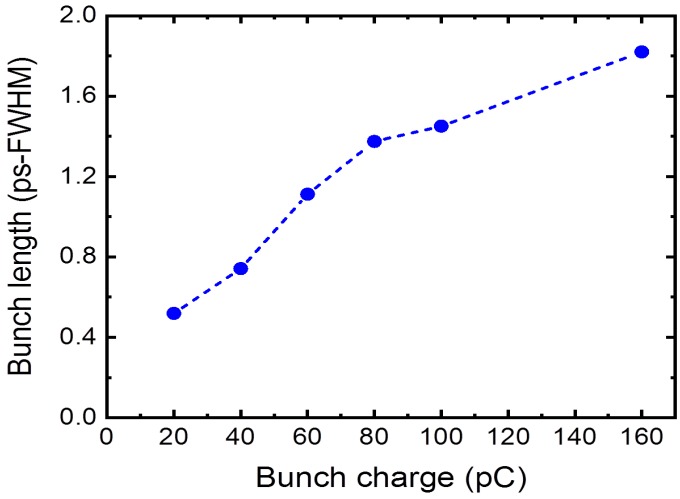

Figure 4.9: Bunch length after chicane bunch compressor from GPT simulation.

4.3.1.2 Measurements of CTR and CUR spectra for the bunch length estimation

The Michelson interferometer was used for measuring the power spectrum of coherent radiation. The principle of this technique was described in Chapter 3. The measurements of the power spectra of Coherent Transition Radiation (CTR) and CUR have been used for estimating the bunch length because the radiation spectrum relates to the bunch form factor [3]. The experimental setups of CTR and CUR were installed at the locations as shown in Figure 4.10. The variation of radiation intensity on the path different (interferogram) can be converted to the power spectrum of the radiation by the fast Fourier transform (FFT). The power spectrum refers to the bunch form factor, given by

$$I(\omega) = FT\{I(\delta)\} \propto \left|R(\omega)T(\omega)\tilde{E}(\omega)\right|^2$$
$$\propto |B(\omega)|^2 \propto f(\omega) \qquad (4.10)$$

where $R(\omega)$, $T(\omega)$, $E(\omega)$ are the reflection coefficient, the transmission coefficient, and the electric field in the frequency domain.

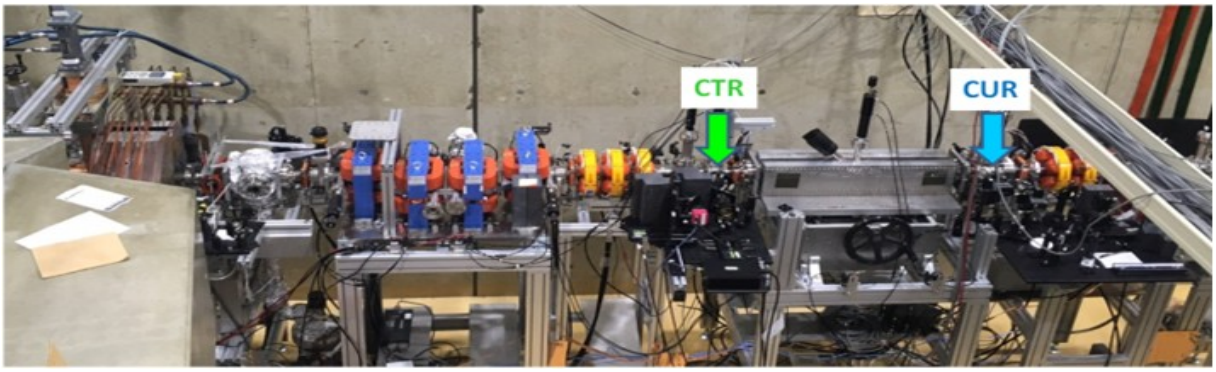

Figure 4.10: Location for the measurements of CTR and CUR.

(a) Experimental setup

1. Coherent Transition Radiation (CTR)

Transition radiation (TR) occurs when a relativistic charged particle crosses the interface between two media of different dielectric properties or different permittivity [9, 10]. Its spectrum has a board spectrum and depends on the longitudinal profile of an electron bunch. Therefore, the TR is suitable for the estimation of the longitudinal bunch length. When an

electron beam with short bunch length crosses the boundary between different dielectric constants, the radiation can be generated coherently. The TR characteristic can be calculated analytically by Ginzburg-Frank (GF) formula from Maxwell equations in the assumptions of far-field approximation. The spectral energy density of transition radiation emitted into the backward direction is defined as

$$\frac{d^2 I_{TR}}{d\Omega d\omega} = \frac{e^2\beta^2}{4\pi^3\varepsilon_0 c}\frac{\sin^2\theta}{(1-\beta^2\cos^2\theta)^2} \tag{4.11}$$

where Ω is the solid angle of the detector, ω is angular frequency, e is the bunch charge of electron, ε_0 is the dielectric constant in vacuum, β is the ratio of the speed of a particle to the speed of light ($\beta = v/c$), c is the speed of light, and θ is the observation angle measured with respect to the backward direction.

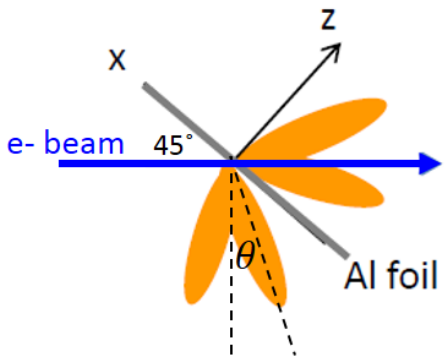

Figure 4.11: Transition Radiation (TR) extraction.

In order to generate TR, an aluminum foil of 11 μm thick was used as a radiation radiator placed on the screen monitor with 45° respect with the electron moving direction as shown in Fig. 4.11. The emitted radiation extracted through a z-cut natural crystal quartz window is not only the backward TR but also in the forward direction. The radiation intensity for the backward direction of the generated transition radiation in parallel and perpendicular polarization can be explained by the following Eq. (4.12) and (4.13), respectively:

$$\frac{dI_{\parallel}}{d\Omega d\omega} = \frac{e^2\beta^2}{2\pi^2 c}\left[\frac{2\sin\theta-\sqrt{2}\beta\cos\varphi}{(\sqrt{2}-\beta\sin\theta\cos\varphi)^2-\beta^2\cos^2\theta}\right]^2 \tag{4.12}$$

$$\frac{dI_{\perp}}{d\Omega d\omega} = \frac{e^2\beta^2}{2\pi^2 c}\left[\frac{\sqrt{2}\beta\cos\theta\sin\varphi}{(\sqrt{2}-\beta\sin\theta\cos\varphi)^2-\beta^2\cos^2\theta}\right]^2 \tag{4.13}$$

where θ is the angle defined in the generated radiation direction and φ is the azimuthal angle.

Since the maximum intensity occurs at $\gamma\,\theta = 1$, the angular distribution has its maximum at the angle given by

$$\theta_m = \frac{1}{\gamma} = \sqrt{1-\beta^2} = \frac{m_e c^2}{E_e} \tag{4.14}$$

where E_e is the energy of electron beam and m_e is the electron mass.

The total intensity of TR by the number of electrons N_e in an electron bunch, can be calculated by

$$\frac{d^2 I}{d\Omega d\omega} = \frac{d^2 I_{TR}}{d\Omega d\omega}\left(N_e + N_e(N_e - 1) f(\omega)\right) \tag{4.15}$$

where I_{TR} is the radiation intensity generated by a single electron, and $f(\omega)$ is the bunch form factor.

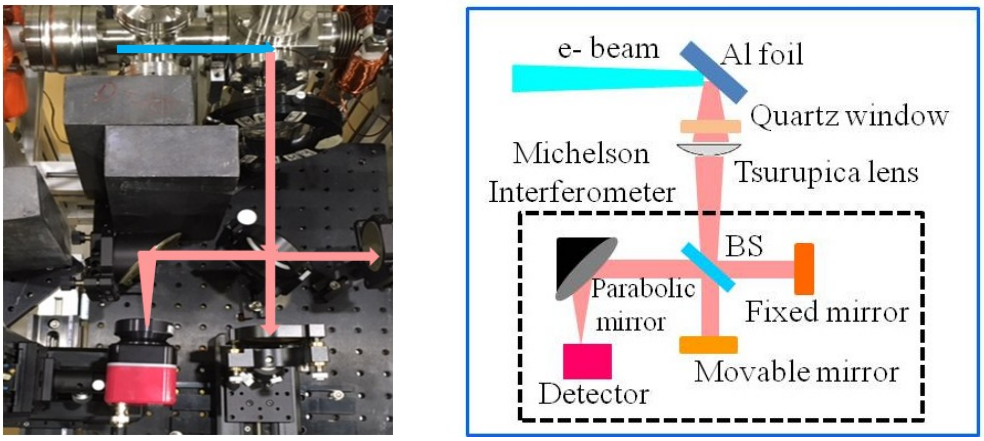

Figure 4.12: Experimental layout of CTR.

For this measurement, the chicane current used was at 5.6 A with the injection phase of 12 degrees and solenoid current of 100 A to reach the maximum CTR intensity at 60 pC. The triplet quadrupole currents were adjusted to focus the electron beam at CTR extraction station. At the other bunch charge, the injection phase, solenoid, and chicane current have to be adjusted slightly to obtain the optimum solution. In this experiment, the extracted CTR before injecting to the interferometer setup was focused by a Tsurupica lens. A schematic diagram and setup of the Michelson interferometer used for the measurement are shown in Fig. 4.12. The 0.1 mm-thick sapphire beam splitter (BS) was used because it has high efficiency of intensity transmission. However, the power spectrum of the CTR was distorted

because the efficiency of the sapphire BS drops to zero at 0.475 THz due to destructive interference. The beams from a fixed mirror and a movable mirror were combined again and focused by a parabolic mirror. The combined beam was aligned again to the center of the detector by using two-plane scanning in x-y axis. A pyroelectric detector (PYD-1, PHLUXi) was used to detect the intensity of the CTR and the intensity signal was recorded by a 1 GHz oscilloscope (Textronix, DPO4104).

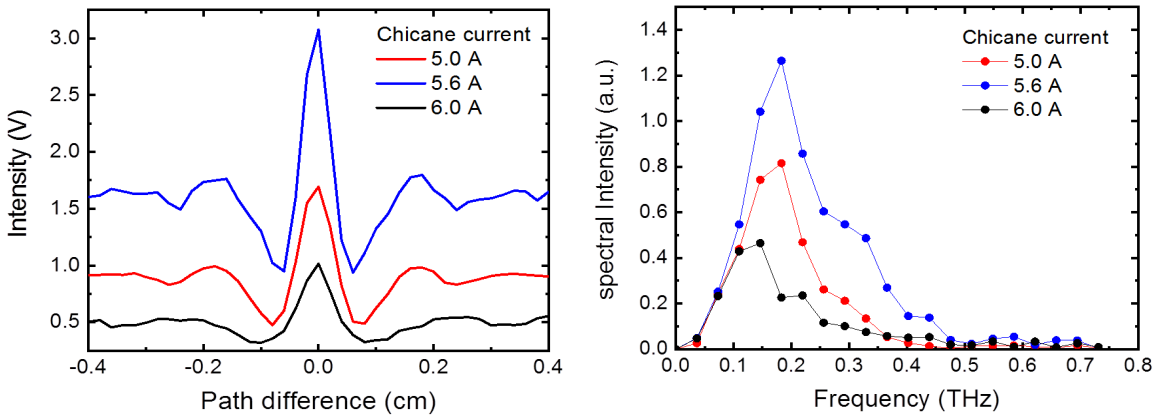

Figure 4.13: (left) Interferogram and (right) frequency spectrum from CTR measurement with the bunch charge of 60 pC at different chicane current.

Figure 4.13 presents the comparison of interferogram and frequency spectrum of CTR. The bunch charge was fixed at 60 pC in order to find the initial condition of chicane current for machine operation. The dependence of CTR intensity on chicane current was measured with fixed the RF phase and solenoid at 12 degrees and 100 A, respectively. The CTR intensity is maximum at the chicane current of 5.6 A, resulting in shortest bunch length as shown in Fig. 4.14. The detail to estimate bunch length from CTR spectrum will be described in the next section.

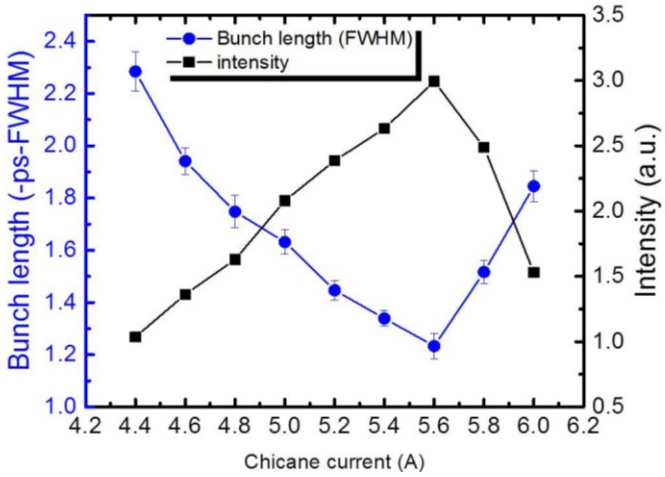

Figure 4.14: Dependence of bunch length on the chicane magnet current at the bunch charge of 60 pC.

2. Coherent Undulator Radiation (CUR)

As explained in Chapter 2, CUR can be produced when a short electron bunch length travels along an undulator. CUR generated in the undulator was reflected by a 20 μm titanium foil. The CUR was extracted through a fused silica window and sent to the Michelson interferometer, as shown in Fig. 3.6 of Chapter 3. Three parabolic mirrors were used to make a THz-CUR beam size smaller and a quasi-parallel beam to fit the Michelson interferometer. In this setup, an Inconel coated pellicle beam splitter was used as a beam splitter, because of its broadband characteristics. The reflected and transmitted beams from the beam splitter were injected to a fixed mirror and a movable mirror, respectively. Both beams were merged again and focused by a parabolic mirror before detected by a pyroelectric detector (PYD-1/2, PHLUXi).

(b) Measurement results

1. Interferogram:

The intensity signals of the CTR and CUR were measured as a function of path difference, as shown in Fig. 4.15(a) and Fig. 4.15(b), respectively. The path difference is equal to the position of the movable mirror multiplied by factor 2. The movable mirror position was scanned with the optical path difference from -0.4 cm to 0.4 cm and from -2 cm to 2 cm with step sizes of 0.01 cm and 0.02 cm for the measurements of CTR and CUR, respectively.

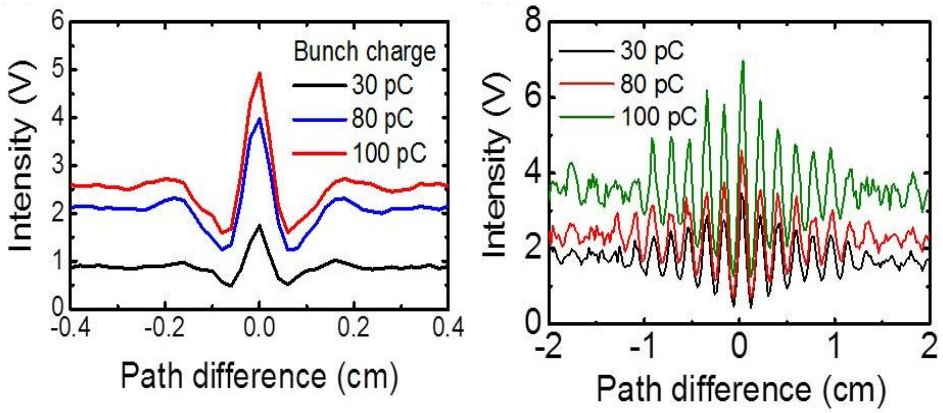

Figure 4.15: Interferograms of (a) the CTR and (b) the CUR at an undulator gap of 30 mm with bunch charges of 30 pC, 80 pC, and 100 pC.

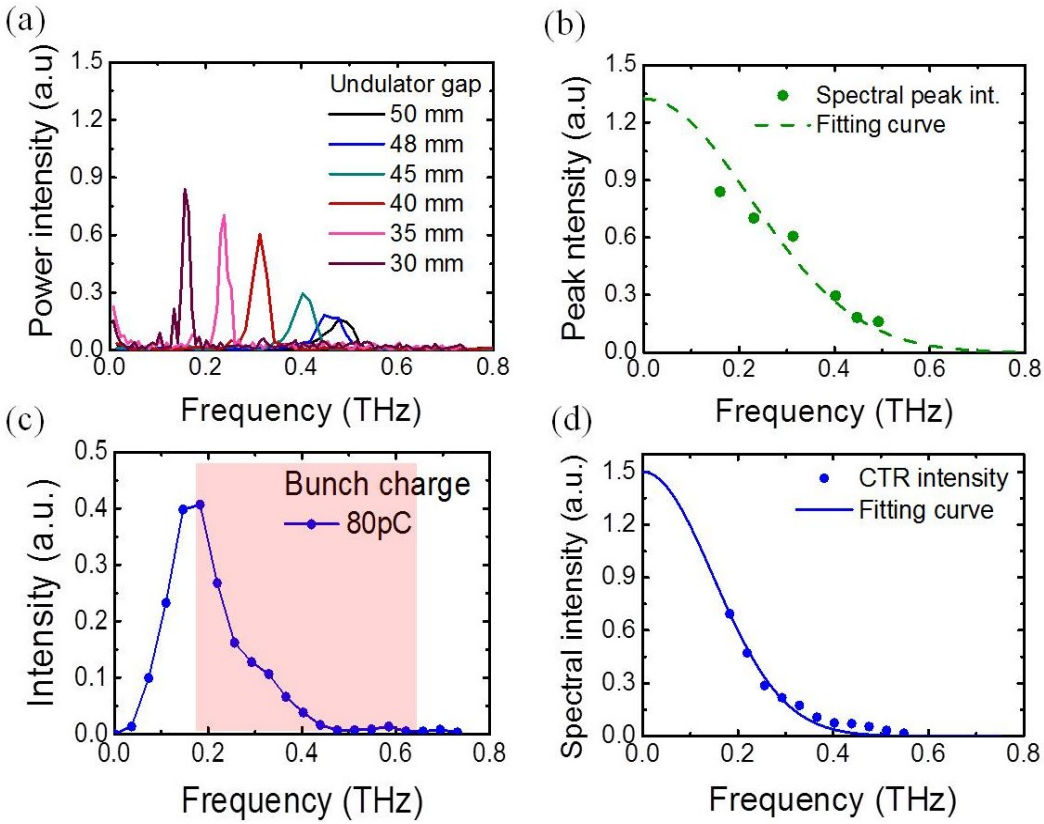

Figure 4.16: Measured spectral power intensity of (a) the CUR and (c) the CTR. The spectral intensity with the fitted curves for (b) the CUR and (d) the CTR with a bunch charge of 80 pC.

2. Spectral intensity:

The interferogram was converted to a power spectrum by using fast Fourier transform (FFT).

- **CTR:** To avoid the distortion of the beam splitter, the power spectrum was normalized with the efficiency of the sapphire BS [11], which relates to the reflection and transmission coefficient of beam splitter. In addition, the frequency range was selected from the center peak of the power spectrum located in the red box of Fig. 4.16(c), which is higher than the 0.16 THz, since the CTR was cut due to the limited aperture of the measurement system and the strong diffraction of low frequency (long wavelength) radiations.
- **CUR:** The resonance frequency of the THz-CUR was varied by changing the undulator gap from 30 to 50 mm in a step of 5 mm, each (Fig. 4.16(a)). Only maximum peaks of power intensities at each undulator gaps were used for estimating the bunch length, as shown in Fig. 4.16(b). Mismatched electron beam optics due to the strong magnetic field of the undulator lead to the decrease of power intensity of the CUR at low frequency.

3. Bunch length:

The bunch length was estimated by fitting spectral intensity with the function of the bunch form factor $f(\omega,\sigma) = A\cdot\exp(-\omega^2\sigma^2)$, as plotted in Fig. 4.16(b) and 4.16(d), with the assumption of Gaussian longitudinal distribution.

Figure 4.17 presents the bunch length performed from CTR and CUR techniques as a function of bunch charges. The measured bunch lengths with the CTR and CUR elongate more than 20% when the bunch charge increases from 30 to 100 pC. In the case of CUR measurement, the mismatched electron beam due to the strong magnetic field of the undulator disturbs the power intensity of the CUR at low frequency. It may result in uncertainty about the estimation of a bunch length. The technique in this experiment can estimate only the relative value. In order to obtain the exact value, the steak camera will be applied future. Although only the relative bunch length can be measured, the results indicated that the electron bunch is lengthened when increasing the bunch charge.

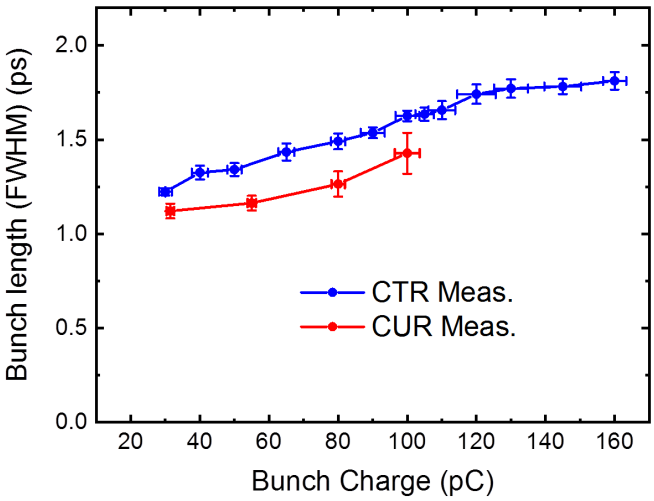

Figure 4.17: Comparisons of the bunch length from CTR and CUR measurements at the different bunch charges.

4.3.2 Optimization of the beam optics in a planar undulator

Since the electron beam optic has a great influence on the power radiation, the lattice functions such as betatron function and beam size inside the undulator have to be optimized for a good condition [12]. The disported beam optics due to the magnetic field of undulator can be compensated with the triplet quadrupoles. For the beam matching [13], the β function has to be optimized to obtain a small fluctuation within the undulator with symmetrical distribution to guarantee the beam traveling through with a large good field region. Figure 4.18 shows the calculation of β function. In the middle of the undulator, the β function is less than 0.2 m for both planes. The beam waist with a minimum β_x and $\alpha_x = 0$ is desired at the undulator center. The matching condition requires for $\beta_{x,1} = \beta_{x,0}$ and $\alpha_{x,1} = -\alpha_{x,0}$. Using the transfer matrix of the drift space, we have $\beta_{x,0} = L(1 + \alpha_{x,0}^2)/2\alpha_{x,0}$

$$M_x = \begin{pmatrix} 1 & z \\ 0 & 1 \end{pmatrix} \tag{4.16}$$

$$\beta_x(z) = \gamma_{x0} z^2 - 2\alpha_{z0} z + \beta_{x0} \tag{4.17}$$

where z is the distance of the undulator (z= 0.7 m).

The focusing properties in the vertical plane can be described with a vertical transfer matrix

$$M_y = \begin{pmatrix} \cos(k_y z) & 1/k_y \sin(k_y z) \\ -k_y \sin(k_y z) & \cos(k_y z) \end{pmatrix} \tag{4.18}$$

where $k_y = 2\pi a_u/\gamma\lambda_u$. At the entrance of the undulator, a minimum β function can be defined as the initial twiss parameters $\beta_{y,ent}=1/\sqrt{ky}$, $\alpha_{y,ent}= 0$. The β function inside an undulator can be calculated by

$$\beta_y(z) = \left(\frac{\beta_{y0}}{2} + \frac{\gamma_{y0}}{2k_y^2}\right) + \sqrt{\left(\frac{\beta_{y0}}{2} - \frac{\gamma_{y0}}{2k_y^2}\right)^2 + \left(\frac{\alpha_{y0}}{k_y}\right)^2} \sin\left[2k_y z + \varphi\right] \tag{4.19}$$

where the initial phase satisfies the equation

$$\varphi = \arctan\left(-\frac{\beta_{\gamma 0}k_y^2 - \gamma_{y0}}{2\alpha_{y0}k_y}\right) \tag{4.20}$$

where $k_y = \frac{1}{2}(B_0/B\rho)^2$ [m^{-2}]. Since our source is operated at low beam energy, the beam optics strongly dominate with undulator field. The field gradient in the horizontal plane can be assumed to be zero in good field region the same as a drift space. The defocusing strength has no influence on the electron beam parameters.

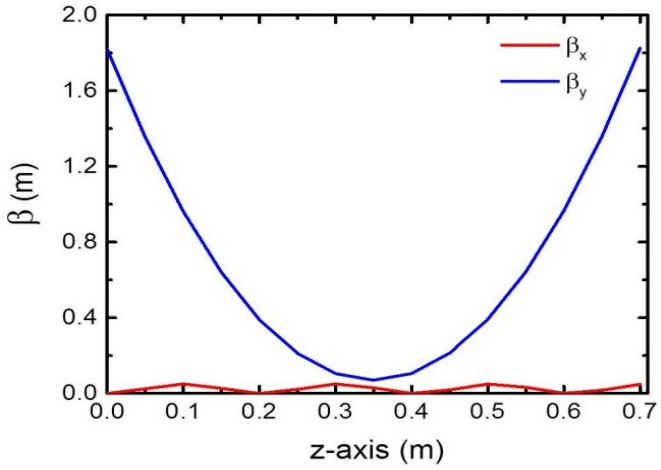

Figure 4.18: β function calculated by the transfer matrix with the beam energy of 4.6 MeV and the undulator field of 0.43 Tesla.

For our machine, the triplet quadrupoles located between a chicane bunch compressor and undulator were used to focus the electron beam. For GPT simulation, the "*GDFsolve"* function was used as optimizer by automatically finding the setting of quadrupole strength to focus the beam size inside undulator. The constraints for optimization were set at the entrance and middle of undulator for horizontal and vertical β function, respectively. The best solution can meet the β function of 0.025 m at the entrance of undulator using the magnetic strengths of the 1st, 2nd, 3rd quadrupoles of 1.45 T/m, -3.19 T/m, and 2.38 T/m, respectively. The result of the β function (Fig. 4.19) has a good matching with the theoretical value. The horizontal

and vertical beam sizes at the middle undulator are 0.253 mm and 0.156 mm, respectively. As a result performed from GPT simulation, it was proven that the triplet quadrupole magnets are enough to optimize the beam optics.

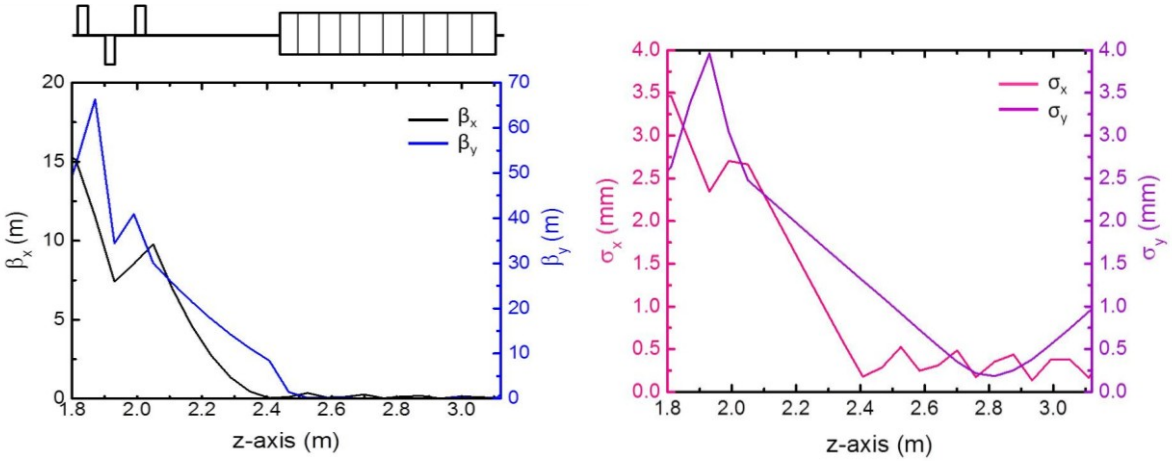

Figure 4.19: (left) β function and (right) beam size with 0.43 Tesla Undulator at the bunch charge of 60 pC after optimization.

In measurement, the transverse beam size inside undulator was observed by the fluorescent screen monitor. The schematic of the screen monitor installation is shown in Fig. 4.20. When the electron beam hits on the screen, the visible lights can be emitted and captured by the CCD camera (BASLER, acA640) with the lens and extension tubes. Figure 4.21 shows the beam profile for the case of 60 pC and 160 pC bunch charges with the undulator field of 0.43 Tesla. The applied currents of triplet quadrupoles were about 0.7 A, 0.8 A, and 0.7 A used in this measurement. The transverse beam size on the screen monitor inside undulator is doubled in both planes when increasing bunch charge from 60 pC to 160 pC. Figure 4.22 shows the comparison of beam size inside undulator between measurement and GPT simulation. The beam size in the real experimental condition is not good agreement with the result performed from GPT simulation because in the actual machine the effects consist of known and unknown effects so more complicated than that from GPT simulation. The possibilities to disturbed the beam size inside undulator may be the misalignment and field error of undulator magnet.

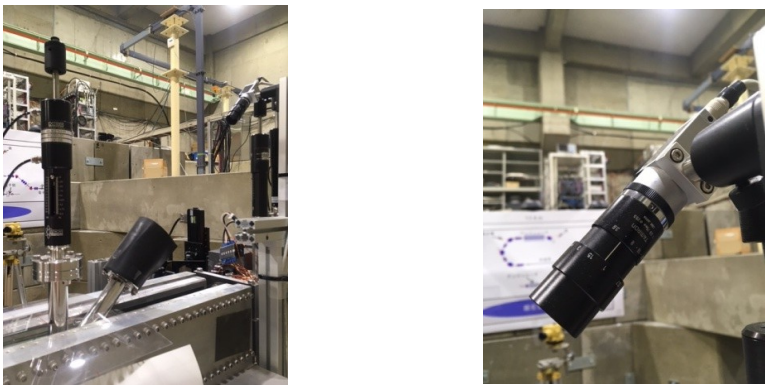

Figure 4.20: Screen monitor to monitor the beam profile and CCD camera (BASLER, acA640).

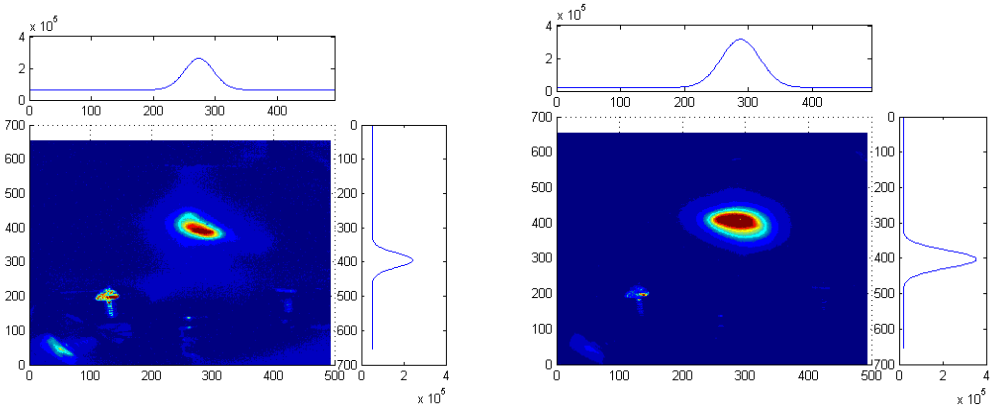

Figure 4.21: Electron beam profile on screen monitor inside undulator at the bunch charge of 60 pC and 160 pC.

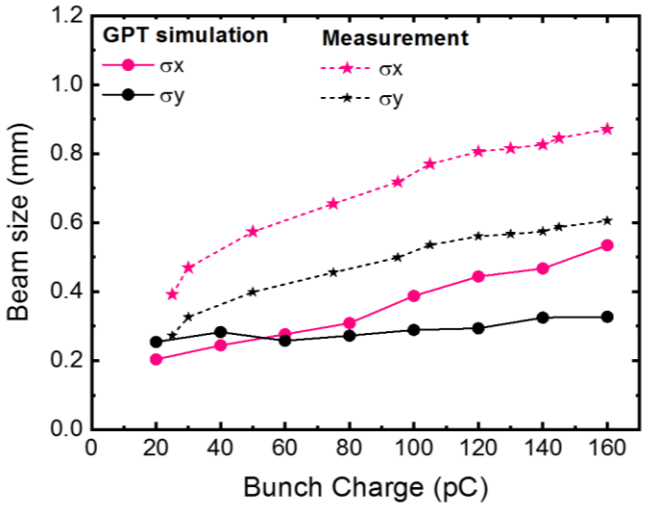

Figure 4.22: Electron beam size inside undulator at gap of 30 mm (0.43 Tesla) compared between simulation and measurement at different bunch charges.

4.3.3 Energy Spread

Besides the bunch length and beam size are important on the enhancement of the radiation power, the energy spread also has a great influence on the radiation power. The energy spread of electron in our source can be simply determined by measuring the angle of deflection of the beams in magnetic field of bending magnet. Upstream bending magnet, the quadrupole magnet is placed for focusing the beam. When the electron beam moves passing through a dispersive region of the bending magnet, electrons with different energies will bend with different deflection angle. The extracted electron beam is cut off by a lead slit going to Faraday cup made of carbon material placed in the air for measuring the bunch charge (Fig. 4.23). The optimum value of machine parameters such as injection phase, solenoid, chicane current, and triplet quadrupole current as mentioned above were used. To estimate the energy spread of electron beam, the bunch charge detected by Faraday cup was measured at different the magnetic field of bending. The relation of bending current and electron beam energy can be converted by the function of E(MeV) = 0.9307I_B(A)-0.4533, where I_B is bending current as reported in [11].

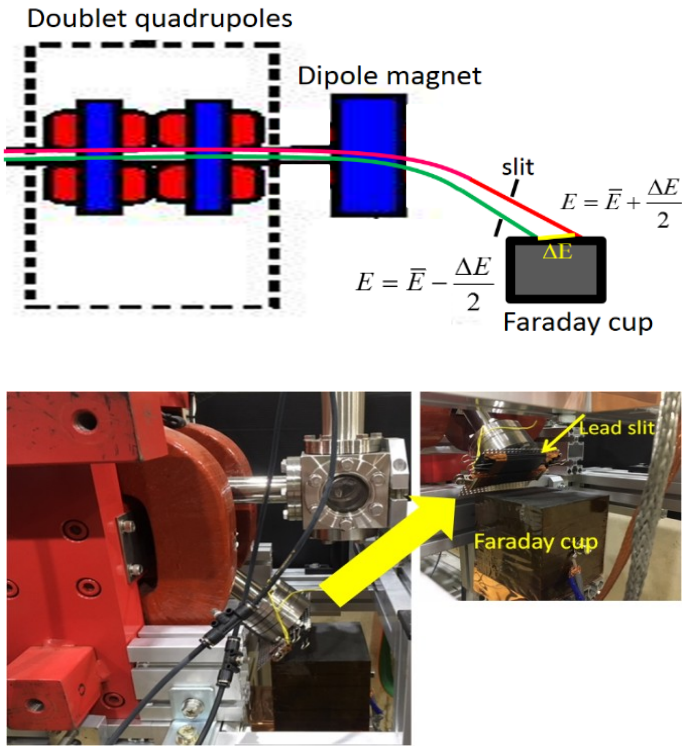

Figure 4.23: Setup of energy spread measurement.

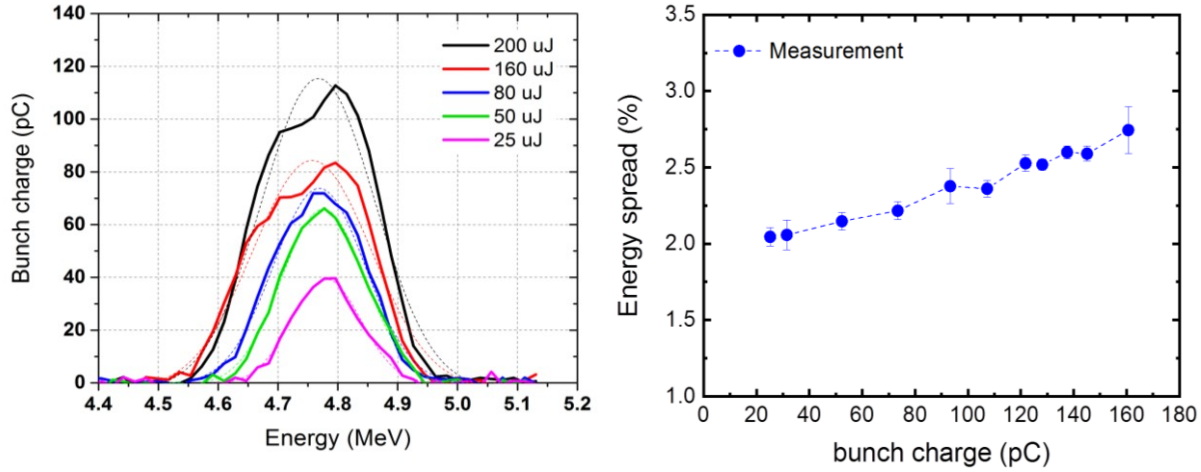

Figure 4.24: (left) bunch charge versus electron beam energy at different laser energy and (right) comparisons of the energy spread between the experiments and the simulation.

In order to study the beam quality degradation, the energy spread of the beam was observed as the function of the bunch charge. The result of relative energy spread as a function of bunch charge is shown in Fig. 4.24(right). The measured energy spread rises up to 3% when increasing bunch charge to 160 pC while the GPT simulation result is about 0.5%. The measurement results are higher than the simulation ones because the CSR effect was not included in the simulation. The emission of CSR also leads to the increase of energy spread and emittance in the bending plane of bunch compression. However, the CSR effect on the increase in energy spread would be able to be minimized by increasing the bending radius or reducing the bend angle.

4.6 Conclusions

The space-charge effect is extremely dominant because of low beam energy source and high charge density. As a result, the electron bunch is easily disturbed and its quality is gradually degraded when reaching to the high charge region. In this chapter, the relative results of the electron beam parameters such as bunch length, beam size and energy spread were investigated as a function of bunch charge. The study showed that the bunch length and energy spread increased as a function of a bunch charge. This would lead to the reducing in THz-CUR power. The trend of measured result was in good agreement with the simulation performed by GPT code. Even the machine condition was optimized in order to increase the quality of electron beam by adjusting the phase injection, solenoid current, and chicane field,

the space-charge force still appeared and disturbed an electron beam in high bunch charge region. Mitigation of the space-charge effect and the optimization of the operational condition are the possibilities to improve the performance of our machine and encourage THz-CUR power enhancement.

The chapter reported in the journal and proceeding as follows

1. S. Krainara *et al*., "Study of the saturation of radiation energy caused by the space charge effect in a compact THz coherent radiation source", *J. Phys.: Conf. Ser.* **2018**, *1067*, 032022.
2. S. Krainara *et al*., "Development of compact THz coherent undulator radiation source at Kyoto University", in *Proc. FEL'17*, USA, MOP049, pp. 0-3, (2017).

4.7 References

[1] K. J. Kim, "RF and space-charge effects in laser-driven rf electron guns", *Nucl. Instrum. Methods A* **275**, pp. 201–218 (1989).

[2] M. Ferrario, *et al*., "Space Charge Effects", CERN Yellow Report CERN-2014-009, pp.331-356 (2014).

[3] S. Krainara, *et al*., "Study of the saturation of radiation energy caused by the space charge effect in a compact THz coherent radiation source", *J. Phys.: Conf. Ser.* **1067**, 032022 (2018).

[4] S. Krainara, *et al*., "Development of compact THz coherent undulator radiation source at Kyoto University", in *Proc.* of *FEL'17*, USA, MOP049, pp. 0-3, (2017).

[5] K. Honkavaara, *et al*., "Bunch length measurements at the Tesla Test Facility using a streak camera", in *Proc.* of PAC. USA, 18-22 June, pp 2341- 2343 (2001)

[6] "User manual version 3.2 General Particle Tracer", Pulsar Physics, NL-5614 BC Eindhoven, The Netherlands.

[7] S. B. van der Geer, *et al.*, "3D Space-charge model for GPT simulations of high-brightness electron bunches", Technical Report TESLA Report 2003-04 (2003).

[8] K. Hyun, *et al*., "Longitudinal Laser Pulse Shaping for Low-Emittance Electron-Beam Generation", *Journal of the Korean Physical Society* **54**(1), pp.381-385 (2009).

[9] C. Settakorn, "Generation and Use of Coherent Transition Radiation from Short Electron Bunches", PhD thesis Stanford University (2001).

[10] B. Schmidt, *et al.*, "Longitudinal Bunch Diagnostics using Coherent Transition Radiation Spectroscopy", tech. rep. DESY-18-027: arXiv:1803.00608 (2018).

[11] S. Suphakul, "Development of Compact Accelerator-Based Terahertz Radiation Source at Kyoto University", PhD Thesis, Kyoto University (2017).

[12] B. Qin, *et al.*, "Status of the planar undulator applied in HUST THz-FEL oscillator", in *Proc.* of FEL, New York, USA, TUPSO62, pp. 372-375 (2013).

[13] Y. Lei, *et al.*, "Optimization of the lattice function in the planar undulator applied for terahertz FEL oscillators", *Chi. Phys. C.* **38**, 037004 (2014).

Chapter 5

Impact of the photocathode excitation laser transverse/longitudinal distribution on the electron beam qualities

5.1 Introduction

Space-charge force plays a critical role that depends not only on bunch charge, size, and energy of the electron bunch but also on the laser shape and pulse width. This effect has an impact on emittance. A distortion of the phase space occurs because of the transverse defocusing force, thus leading to the emittance growth. This distortion can be minimized by manipulating the beam envelope with focusing solenoid magnet placed at downstream of the gun but cannot for the non-linear effect [1]. For our case, the space-charge force will lead to the distortion of longitudinal phase space, which is significant on the bunch compression as described in Chapter 4. The manipulation of laser pulse may assist in overcoming space-charge effect.

In this chapter, the main purpose is to find a way to mitigate the space-charge effect. The methods and results based on detailed simulations on the manipulation of transverse and longitudinal laser distributions are presented. Since the result of THz-CUR properties was

limited by the reduction of the beam quality due to nonlinear space-charge effect, the method of manipulation of laser shape will be applied to solve the problem mentioned. An increase of electron beam energy can reduce the space-charge force and be helpful to enhance the radiated power. However, our source has a limitation of RF power, and also the THz-CUR project is targeting a compact system, so using an additional acceleration tube cannot be an acceptable means of increasing the electron energy. Therefore, to eliminate the problem addressed above, it is necessary to study how the laser shape is significant for the bunch compression. The manipulation of transverse and longitudinal laser distributions can be done by enlarging the laser pulse widths and changing the laser transverse profile from Gaussian to a truncated-Gaussian distribution. Section 5.1 demonstrates clearly how the space-charge effect impacts the electron beam quality and exhibits the process of bunch compression. For a better understanding, the dependences of the electron beam quality on the operating conditions, such as the distributions of the laser, including laser pulse width and transverse size, have been investigated and are shown in Section 5.2. Section 5.3 is dedicated to the results of compressed bunch length and longitudinal particle distribution after manipulating the laser distributions. Finally, in Section 5.4, we make conclusions on the results.

5.2 Electron beam disturbed by space-charge effect

5.2.1 Longitudinal phase space before compression

In order to get a suitable energy chirp, the longitudinal phase space was optimized with the RF phase and the solenoid field. The optimization is to obtain a small emittance in both planes at RF gun exit and to preserve a linear energy chirp for the bunch compression in a chicane. In order to understand the electron beam behavior with the space-charge effect, Figure 5.1 shows the longitudinal particle distribution at the chicane entrance comparing between turning off and turning on the space-charge effect from general particle tracer (GPT) simulation with the present laser distribution of our THz-CUR source. The optimal RF phases would be 20 and 10.5 degrees, and the solenoid fields were optimal at 0.162 and 0.103 Tesla for the cases of turn off and turn on space-charge, respectively. Although the solenoid focusing can be used especially for the compensation of the linear space-charge force, it cannot be used for the nonlinear space-charge force on the cathode surface.

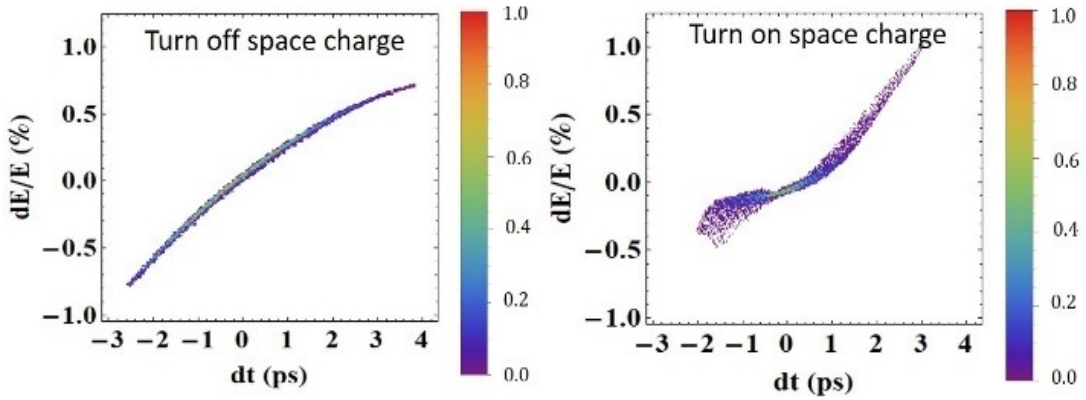

Figure 5.1: Longitudinal distribution at the chicane entrance in the case of turning off and turning on the space-charge effect at 60 pC charge.

Figure 5.2a shows the longitudinal phase space distribution at different bunch charges given by GPT simulation at the chicane entrance in order to check the influence of the nonlinear space-charge force on an electron bunch. Although the laser injection phase and the solenoid field have been set to the optimum point for finding the suitable energy chirp before the compression process, the distortion of the electron bunch occurs due to the space-charge force or the charge repulsion force. It was found that the bunch's energy chirp decreased with the increase of the bunch charge owing to the large space-charge force. The bunch's tail loses energy while the head gains energy to decrease the energy chirp.

In the transverse space, the coupling effect between the transverse and longitudinal emittance directly leads to the evolution of particle distribution to disturb the energy chirp and results in bunch lengthening. The perturbation of bunch length caused by the beam divergence at the gun exit can be simply described by Equation 5.1 [2, 3]:

$$\Delta\sigma_z = \frac{L}{2}(x'^2 + y'^2) \tag{5.1}$$

where L is the distance of the drift space and x' and y' are the beam divergence in the horizontal and vertical planes, respectively. In general, the transverse emittance blow-up at higher bunch charge leads to the increase of bunch length, according to Equation (5.1). Therefore, the effect of beam divergence is one of the factors preventing the generation of a short electron bunch. Reducing the beam divergence is a powerful process to prepare the

chirp for compressing the electron bunch, which can be obtained by the manipulation of the laser distribution.

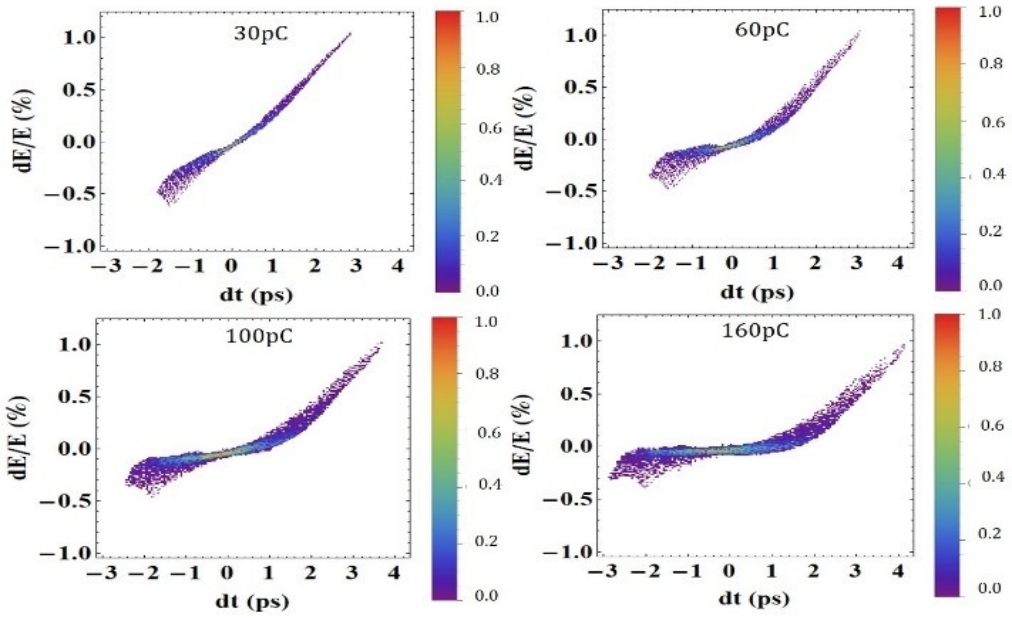

(**a**)

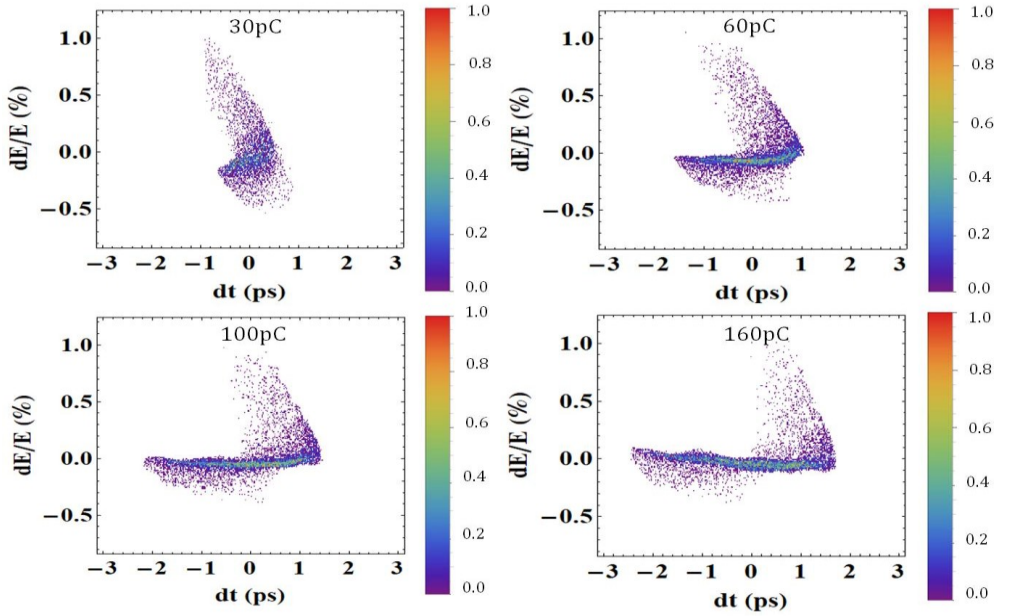

(**b**)

Figure 5.2: Energy–time phase space with turning on the space-charge effect with the bunch charge of 30 pC, 60 pC, 100 pC, and 160 pC (a) before and (b) after the bunch compression chicane if the cathode is excited by a laser pulse width of 5.8 ps-FWHM and Gaussian profile.

5.2.2 Bunch compression with negative R_{56} chicane

In the general approach to bunch compression, the first-order momentum compaction R_{56} has to match with the bunch's energy chirp, h by $R_{56} = -1/h$. Our chicane bunch compressor was designed to compress a bunch with a negative linear longitudinal dispersion ($R_{56} < 0$) and, thus, a positive energy chirp ($h > 0$). The energy chirp of this machine is mainly induced by the laser injection phase, which is determined by the acceleration efficiency of the electron beam. The diagram of the bunch compression chicane and the evolution of the longitudinal phase space are presented in Figure 5.3. The tail of the bunch with higher energy passes through the chicane with a shorter path length compared to the head with lower energy. When the electron bunch disturbed by the space-charge effect passes through the dispersive section of the bunch compressor, the electron beam quality is extremely degraded, resulting in the diminishment of an effective bunch compression [4].

The evolution of longitudinal phase space or the change in bunch length after bunch compression can be determined by Equation 5.2 [5, 6]:

$$\sigma_{zf} = \sigma_{zi} + R_{56}\delta E + T_{566}\delta E^2 + U_{5666}\delta E^3 + f(T_{511}, \dots, T_{565}) \tag{5.2}$$

where σ_{zi} and σ_{zf} are the bunch length before and after compression, respectively; the coefficients of the momentum compaction factor are in terms of R_{56}, T_{566}, and U_{5666}; and δE is energy spread. The higher-order terms of T_{566} and U_{5666} can be simply defined as $-3R_{56}/2$ and $2R_{56}$, respectively. The energy chirp must be positive or the R_{56} should be negative so as to shorten the bunch length. However, the bunch lengthening is also caused by the beam divergence, which largely depends on the second-order effects, $f(T_{511}, \dots, T_{565})$ consisting of the transfer matrix coefficients from T_{511} to T_{565}, which can be explained as $T_{511}\sigma_{\mathrm{x}}^2$, $T_{512}\sigma_{\mathrm{x}}\sigma_{\mathrm{x}'}$, $T_{522}\sigma_{\mathrm{x}'}^2$, $T_{533}\sigma_{\mathrm{y}}^2$, $T_{534}\sigma_{\mathrm{y}}\sigma_{\mathrm{y}'}$, and $T_{544}\sigma_{\mathrm{y}}^2$. The terms σ_x and σ_y are referred to as the electron beam size in the horizontal and vertical planes, respectively, within a standard deviation by assuming its Gaussian distribution, and the transverse divergences are defined in terms of $\sigma_{\mathrm{x}'}$ and $\sigma_{\mathrm{y}'}$. The increase of the bunch length can be caused by the transverse emittance blow-up due to the space-charge effect since the parameters of beam size and transverse divergence are linked to the transverse emittance.

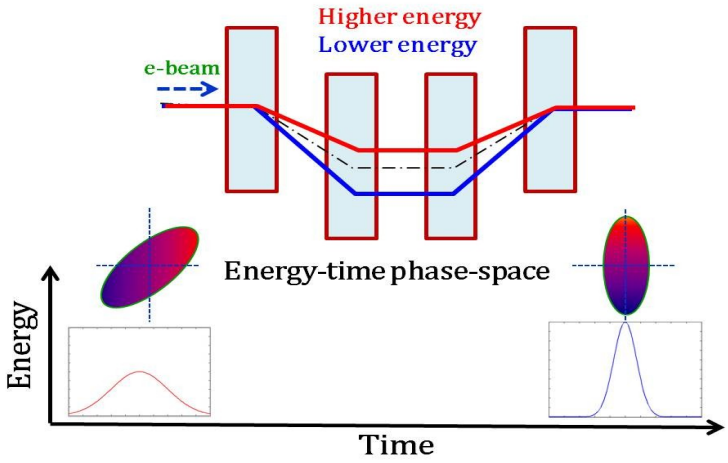

Figure 5.3: Magnet arrangement in the magnetic chicane and the evolution of energy–time phase space during passing though the chicane.

According to the optimization of the machine conditions of 5.8 ps-FWHM and Gaussian profile, we scanned the machine parameters, such as the RF phase, solenoid field, and chicane field. The method used for optimization was to calculate the space-charge factor as the functions of the RF phase and solenoid field, and then to consider a suitable energy chirp for compression, which would be close to the value of the energy chirp in the case of no space-charge. The detail of the optimization was explained in chapter 4. It was found that the optimal RF phases would be 20 and 10.5 degrees, and the solenoid fields were optimal at 0.162 and 0.103 Tesla to provide a suitable energy chirp for the bunch compression for the cases of turning off and turning on the space-charge effect, respectively. Obviously, the longitudinal particle distribution is not completely rotated after passing through the chicane magnet, even with careful adjustment to find the optimum chicane magnetic field (Fig. 5.2b)**.** As explained above, the emittance blow-up or the beam divergence is gradually expanded on account of the space-charge effect causing the rotation of the longitudinal phase space and disturbing the electron bunch. This effect can be minimized by shaping the laser distribution both in transverse and longitudinal directions.

5.3 Manipulation of transverse/longitudinal laser distribution

The photocathode electrons have been used in many facilities, such as free electron laser (FEL) sources, for producing short bunch length with high charge [7–10]. However, a

problem of the high space-charge effect in the low-energy region is causing emittance blow-up. The electron beam emittance has been minimized as much as possible in order to reach the higher power. Therefore, to keep the emittance low, the space-charge effect must be substantially mitigated. The technique of shaping the laser distribution in order to reduce the space-charge effect causing emittance has been reported in many studies [10–14]. The drive laser pulse must be expanded or made uniform before illuminating the cathode to generate the best emittance of the electron beam. Moreover, in Ref. [15], it was reported that the transverse emittance at the Linac Coherent Light Source (LCLS) injector was reduced with applying the truncated-Gaussian profile, which can be done simply by clipping using an aperture [16]. The space-charge force is more linear and can be compensated by applying a solenoid field. If the space-charge effect is not eliminated, it can disturb the electron bunch along the beam transportation [17]. At other facilities, the mitigation of space-charge force by manipulating the laser pulse could be as a helper for achieving a low emittance. For our source, this method could be applied to control the electron bunch or the energy chirp before bunch compression. With the reduction of this effect, the energy chirp would be suitable and could be successfully performed for bunch compression to obtain a short bunch length.

To intentionally restrain the space-charge effect, the manipulation of the drive laser pulse both in the transverse and longitudinal directions before injecting the cathode is required for producing the short electron bunch length because the laser distributions determine the longitudinal and transverse distributions of the electron beam upon emission. This can help to reduce the longitudinal emittance due to the higher-order effects and also to avoid inducing the increase of the bunch length. The cathode laser condition determines an initial configuration of electrons at the cathode.

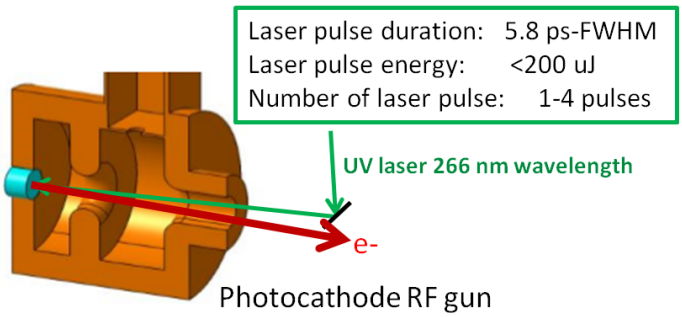

Figure 5.4: Layout of laser exciting the cathode in RF gun.

It is well known that the longitudinal and transverse distributions of the exciting laser pulses have a significant impact on the electron beam quality and source performance because the laser distributions determine the longitudinal and transverse distribution of the electron beam emission. In this study, we have investigated the electron beam quality at the difference of transverse laser distribution between Gaussian and truncated-Gaussian profiles, and have also studied the dependence of the compressed bunch length on the laser pulse width. The laser parameters used are listed in Table 5.1. The layout of laser drive photocathode to generate electrons is shown in Fig. 5.4.

Table 5.1: Distributions of a laser illuminating the cathode with the bunch charge of 160 pC and 300 pC.

Transverse laser size of 0.5 mm-rms	Laser pulse width FWHM
Gaussian	5.8 ps, 10 ps, 15 ps, 20 ps
truncated-Gaussian	5.8 ps, 10 ps, 15 ps, 20 ps

The laser distributions illuminating the cathode are examined in both the transverse and longitudinal directions as follows:

1. **Transverse laser profile**: The transverse truncated-Gaussian profile can be modified by clipping the drive laser of the Gaussian profile with an aperture before irradiation. The laser spatial distribution has to be cut at the center, as shown in Figure 5.5(top). The intensity laser for the transverse profile before injecting the cathode is presented in Figure 5.5(bottom). An analytical model of the truncated-Gaussian beam to express the charge density (ρ) referring to the space-charge force can be written as the following equation [15]:

$$\rho = \frac{Q}{(2\pi)^{3/2}\sigma_x^2 Erf\left(r_a/\sqrt{2}\sigma_x\right)^2\sigma_z} e^{-((x^2+y^2)/2\sigma_x^2)-(z^2/2\sigma_z^2)} \tag{5.3}$$

where Q is the total charge, *Erf* is an error function, σ_x and σ_z are the rms beam sizes in the transverse and longitudinal directions, respectively, and r_a is the aperture radius. This equation clearly shows that the charge density depends on the bunch charge (in both planes), which can be controlled by the injection laser in a photocathode RF gun for $x^2 + y^2 < r_a^2$. The

charge density is equal to zero ($\rho = 0$) if $x^2 + y^2 > r_a^2$, where the spatial distributions in the x and y planes are determined as Gaussian distributions.

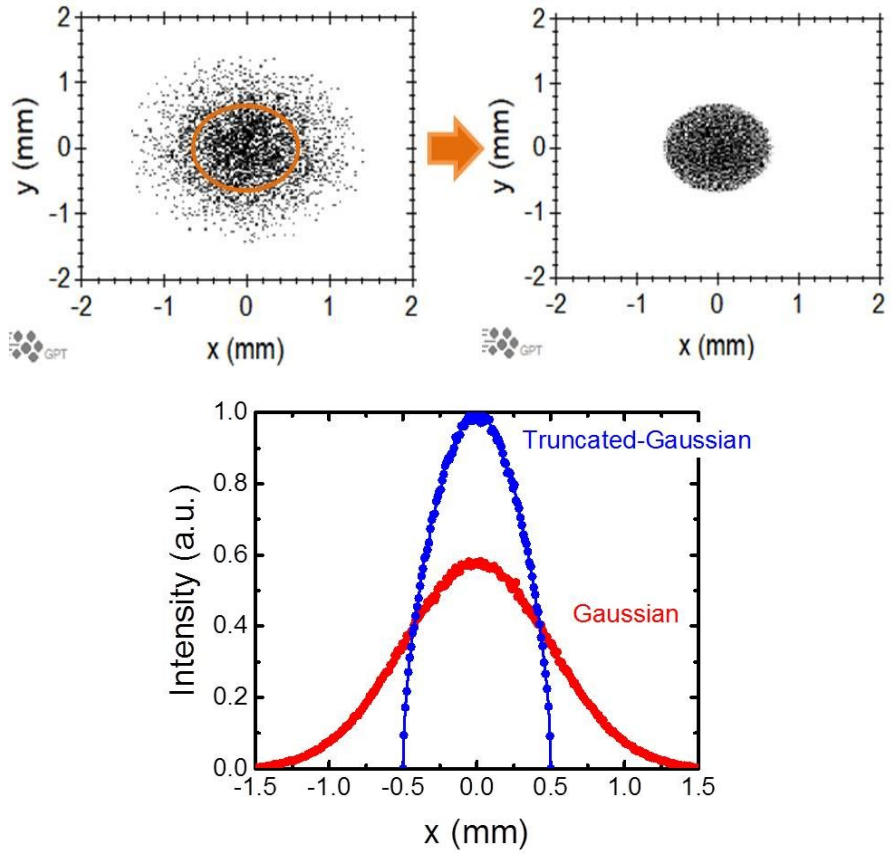

Figure 5.5: (top) Transverse laser profile: (left) Gaussian and (right) truncated-Gaussian clipped with aperture size of 0.5 mm; and (bottom) laser distribution for the transverse profile before injecting the cathode.

Normally, the emittance blow-up due to the linear space-charge effect could be compensated by the solenoid field. In order to mitigate the nonlinear space-charge effect, the ratio between the beam size and aperture size (σ_x/r_a) should be the factor of 1 to obtain a linear space-charge force. That means the laser profile should be truncated at 0.5 mm whenever the radius of spatial distribution is σ_x = 0.5 mm in the Gaussian distribution. The truncated-Gaussian profile has a more linear space-charge force in comparison to the Gaussian profile [18]. The optimization of the transverse laser size is to correct the radial RF field effects and the nonlinear space-charge effect [19]. The emittance has been investigated versus the aperture size, as plotted in Figure 5.6. To achieve a reasonable aperture size for

this condition, the spatial distribution has to be clipped by using the aperture radius of 0.5 mm. The transverse emittance was compensated and minimized from 2.6 to 1.2 mm-mrad. The measured result in Ref. [15, 19] reported that the quality of the electron beam (emittance) was successfully improved with the truncated-Gaussian profile. Reducing the aperture size also makes the result of longitudinal emittance gradually decrease as well. An electron beam with low transverse emittance and low longitudinal emittance impacts the bunch compression to attain a short electron bunch.

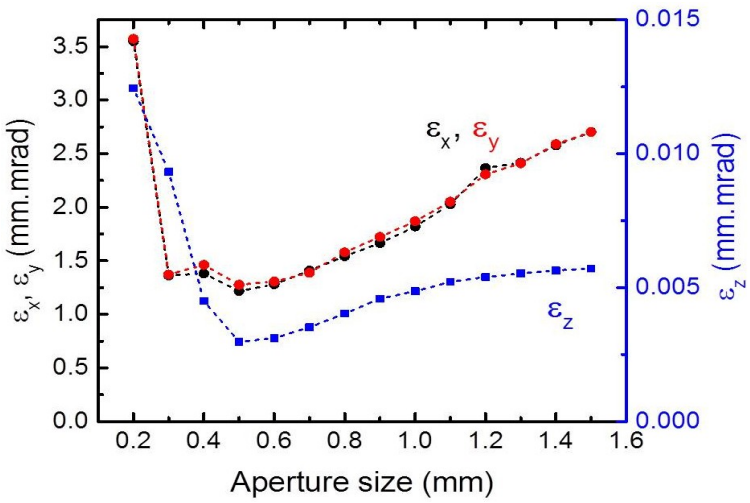

Figure 5.6: Transverse and longitudinal emittances at different rms. transverse radius at the entrance of bunch compression with the bunch charge of 160 pC and the laser pulse width of 5.8 ps-FWHM.

2. **Laser pulse width**: The laser pulse width was enlarged from 5.8 ps-FWHM to 10 ps-FWHM, 15 ps-FWHM, and 20 ps-FWHM with Gaussian distribution as plotted in Fig. 5.7. Since the laser pulse width can be defined as the initial length of the electron bunch, the longitudinal bunch can be deformed more easily by the shorter bunch length owing to a stronger space-charge effect in the longitudinal direction. The expanding of the pulse width would have a low effect on electron beam dynamics because of lower charge density of the electron bunch. In practice to elongate the longitudinal laser pulse, the longer laser pulse width will be provided by using the pulse stacking system reported in Ref. [14] and will be presented in the next Chapter.

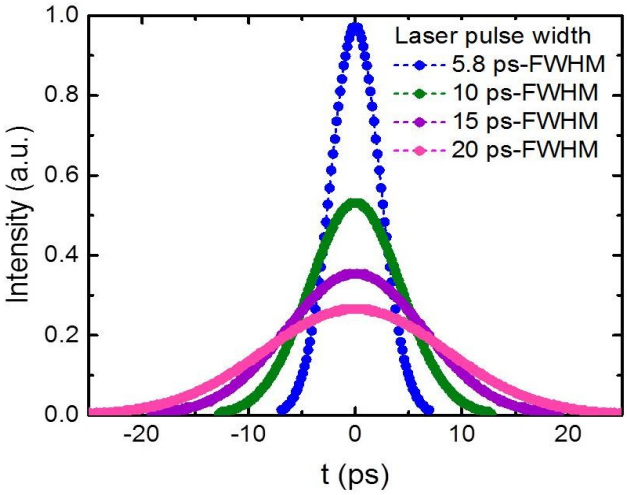

Figure 5.7: Dependence of the longitudinal distribution on the laser pulse width before irradiation with a fixed bunch charge.

5.4 Results and discussion

5.4.1 Longitudinal particle distribution

According to manipulation of the laser distributions before irradiating the cathode to reduce the space-charge effect, it was found that the longitudinal phase space distribution of the electron bunch at the entrance of the chicane seems to be similar with the case of turn off space-charge and has a high chirp of energy–time, as shown in Fig. 5.8. As a result, the electron bunch can be compressed to reach a higher peak current after passing through the chicane magnet. The effective bunch compression can be investigated from the peak current and the longitudinal particle distribution.

Figure 5.8 clearly presents the longitudinal phase space simulated using the truncated-Gaussian profile with the pulse width of 5.8 ps-FWHM and 10 ps-FWHM in the case of the bunch charges of 160 pC and 300 pC. It is interesting to note that the space-charge force using the laser profile of truncated-Gaussian distribution may be more linear and lower than that of the Gaussian profile the same as the result reported in [15, 19]. The reduction of the space-charge effect is not only dependent on the laser transverse profile, but also gets lower with a longer laser pulse width.

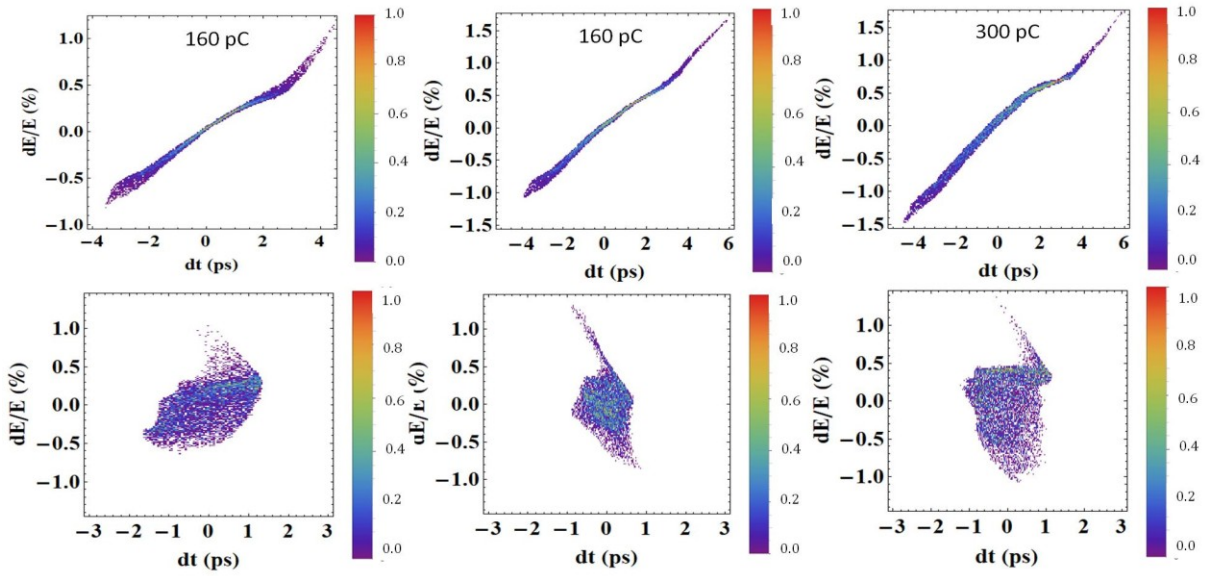

Figure 5.8: Longitudinal phase space distribution of the electron bunch at the entrance (top) and the exit (bottom) of the chicane magnet, with truncated-Gaussian distribution with the laser pulse width of (left) 5.8 ps-FWHM, 160 pC; (middle) 10 ps-FWHM, 160 pC; and (right) 10 ps-FWHM, 300 pC.

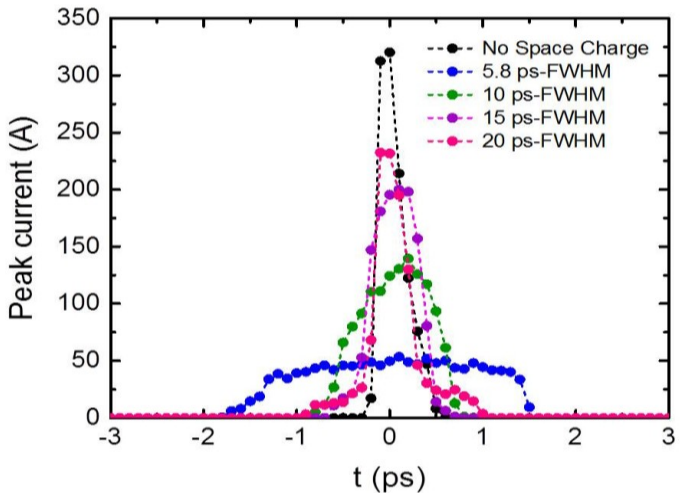

Figure 5.9: Longitudinal particle distribution after bunch compression for the different laser pulse widths with the truncated-Gaussian profile (r_a = 0.5 mm) in the case of the bunch charge of 160 pC.

Figure 5.9 illustrates the longitudinal particle distribution versus peak current in a variety of laser pulse widths**.** Obviously, the longitudinal particle distribution with high peak current and narrow distribution can be obtained when increasing the laser pulse width. This result

clearly shows that the space-charge effect deforming the electron bunch can be considerably lessened with expanding the laser pulse width together with using the truncated-Gaussian profile. Using 20 ps-FWHM laser pulse width and truncated-Gaussian profile, the longitudinal electron distribution can be compressed and the bunch length is almost similar the case of turning off space-charge effect. Therefore, this condition of laser distribution would be enough for mitigating the space-charge effect for the bunch charge of 160 pC.

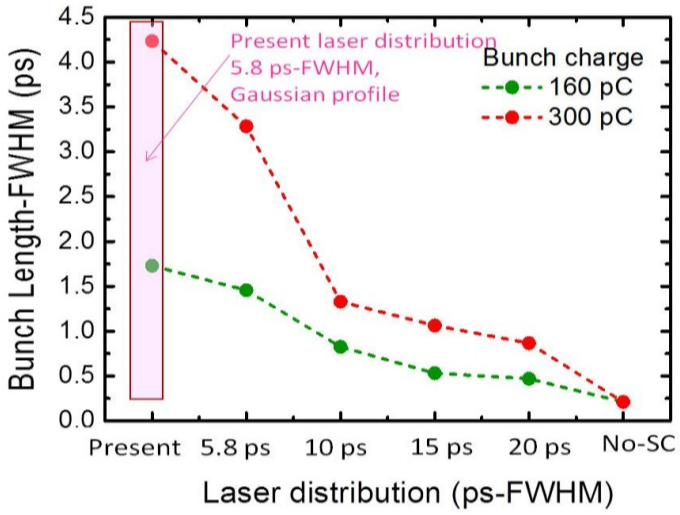

Figure 5.10: Comparison of the bunch length with the present laser distribution (5.8 ps-FWHM, Gaussian profile) and the laser pulse width of 5.8 ps-FWHM, 10 ps-FWHM, 15 ps-FWHM, and 20 ps-FWHM with a truncated-Gaussian profile, and no space-charge effect at the bunch charge of 160 pC and 300 pC.

5.4.2 Electron bunch length

From the longitudinal phase space after compression, it was found that the electron bunch can be compressed to achieve a shorter length and a higher peak current by using the long laser pulse width and truncated-Gaussian profile. In order to estimate the bunch length, the longitudinal particle distribution in Fig. 5.9 was converted to the bunch form factor by using a fast Fourier transform (FFT) with high frequency resolution, and was fitted with a function of a bunch form factor with Gaussian distribution ($f(\omega,\sigma) = \exp(-\omega^2\sigma^2)$). Figure 5.10 shows the decreases of the simulated bunch length when keeping the charge constant at 160 pC. By expanding the laser pulse width from 5.8 ps-FWHM to 10 ps-FWHM, the electron bunch was compressed to 0.82 ps-FWHM with using the truncated-Gaussian profile. With the

laser pulse width to 20 ps-FWHM, the compressed electron bunch was shorter than 0.5 ps-FWHM. For the bunch charge of 300 pC, the bunch charge was about 1.0 ps-FWHM with using the laser pulse width of 20 ps-FWHM and trauncated-Gaussian profile.

It is worth noting that the length of the electron bunch can be compressed to 0.21 ps-FWHM in the case of turning off the space-charge effect with the present laser distribution used in the THz-CUR source. This result would suggest that this is the minimum bunch length available in this source. In order to respond to the requirement of the enhancement of the radiated power in MW-class quasi-monochromatic THz pulses, we have also studied the compression of the electron bunch in the case of increasing the bunch charge to 300 pC. It can be seen that with the 5.8 ps-FWHM laser pulse width, the electron bunch was not successfully compressed, even when using the truncated-Gaussian distribution. The space-charge effect still greatly disturbs the electron bunch. However, the length of the compressed electron bunch was gradually shortened when expanding the laser pulse width.

5.5 Conclusions

In this study, we investigated bunch length as a function of the parameters of the laser, including the pulse width and the transverse distribution, by using the numerical simulation code GPT for mitigating the space-charge effect in a THz-CUR system. It was found that the most powerful way to mitigate the space-charge effect in the THz-CUR system at Kyoto University is to manipulate the laser distribution both in the transverse and longitudinal planes for preventing the degradation of electron beam quality. The high efficiency of chicane bunch compression can be achieved by controlling the transverse laser profile on the cathode with the truncated-Gaussian distribution. However, increasing the laser pulse width can obtain the shortening of the length of the compressed electron bunch. The examination of the transverse truncated-Gaussian distribution, as well as the enlargement of the laser pulse width to generate the higher radiated power of THz-CUR, will be performed experimentally and presented in next Chapter.

The chapter reported in the journal and proceeding as follows

1. S. Krainara *et al*., "Manipulation of laser distribution to mitigate the space-charge effect for improving the performance of a THz Coherent Undulator Radiation source", *Particles* **1**(1), pp.238-252 (2018).
2. S. Krainara *et al*., "Mitigation of the space charge effect for improving the performance of THz-CUR source"" , in *Proc. PASJ Conf.*, WEP007, (2018).

5.6 References

[1] J. Yang, *et al*., "Experimental studies of photocathode RF gun with laser pulse shaping", in *Proc.* of EPAC'02, Paris, France, 3-7 June, pp. 1828-1830 (2002)

[2] X. J. Wang and X. Chang, "Femto-seconds kilo-ampere electron beam generation", *Nucl. Instrum. Methods A* **507**, pp. 310–313 (2003).

[3] X. J. Wang and I. Ben-Zvi, "Longitudinal emittance compensation in a photocathode RF gun injector", in *Proc.* of PAC'97, Vancouver, BC, Canada, 12–16 May, p. 6259326 (1997).

[4] A. He, *et al*., "Design of low energy bunch compressors with space charge effects", *Phys. Rev. ST Accel. Beams* **18,** 014201 (2015).

[5] J. Byrd, "Bunch Compressors. Presented at Lecture of Short Bunches in Accelerators: USPAS", Boston, MA, USA, 21–25 June, (2010).

[6] K. Kan, *et al*., "Effect of emittance and space-charge in femtosecond bunch compression", *Nucl. Instrum. Methods A* **597**, pp. 126–131 (2008).

[7] G. Pencoa, *et al.,* "Optimization of a high brightness photo injector for a seeded FEL facility", *J. Instrum.* **8**, P05015 (2013).

[8] K. C. Harkay, *et al*., "Photocathode studies for ultra-low-emittance electron sources", in *Proc.* of PAC, Vancouver , Canada, 4–8 May, pp. 458–460 (2009).

[9] K. Togawa, *et al.,"*CeB6 electron gun for low-emittance injector", *Phys. Rev. ST Accel. Beams* **10**, 020703 (2007).

[10] R. Akre, *et al*., "Commissioning the Linac Coherent Light Source injector", *Phys. Rev. ST Accel. Beams* **11**, 030703 (2008).

[11] B. L. Beaudoin, *et al*., "Longitudinal bunch shaping of picosecond high-charge MeV electron beams", *Phys. Plasmas* **23**, 103107 (2016).

[12] K. Hyun, *et al.,* "Longitudinal laser pulse shaping for low-emittance electron-beam generation", *J. Korean Phys. Soc.* **54**, 381–385 (2009).

[13] J. Yang, *et al.,* "Low-emittance electron-beam generation with laser pulse shaping in photocathode radio-frequency gun", *J. Appl. Phys.* **92**, 1608 (2002).

[14] C. Kim, *et al.,* "Laser pulse shaping for generation of low-emittance electron beam", in *Proc.* of FEL, Gyeongju, Korea, 24–29 August, pp. 278–281 (2008).

[15] F. Zhou, *et al.,* "Impact of the laser spatial distribution on the LCLS photocathode gun operation", *Phys. Rev. ST Accel. Beams* **15**, 090701 (2012).

[16] W. W. Li, *et al.,* "Generation and measurement of sub-picosecond electron bunch in photocathode RF gun", in *Proc.* of IPAC, Shanghai, China, 12–17 May, pp. 372–374 (2013).

[17] T. Miyajima, *et al.,* "Low emittance electron beam transportation in compact ERL injector", in *Proc.* of IPAC, Dresden, Germany, 15–20 June, pp. 3104–3106 (2014).

[18] L. Serafini, "Improving the beam quality of RF guns by correction of RF and space-charge effects", *AIP Conf. Proc.***279**, 645 (1992).

[19] F. Zhou, *et al.*, "Characterizing and Optimization Photocathode Laser Distributions for Ultra-Low Emittance Electron Beam Operations", SLAC-PUB-16436; U.S. Department of Energy, Office of Science: CA, USA, (2015).

Chapter 6

Improvement of THz-CUR source performance by mitigating the space-charge effect

In the previous chapter, the method for reducing the space-charge force in an electron bunch was proposed. Here, the experiments to pursue the quality of the higher beam were carried out by changing the transverse laser profile to the truncated-Gaussian distribution, the longitudinal pulse to flat-top shape, and also increasing the laser pulse width. The expected radiation power from the simulation bunch form factor is presented in section 6.1. The examination of the transverse truncated-Gaussian distribution as well as the enlargement of the laser pulse width, are described in section 6.2. The first experimental observations of the properties of the electron beam and coherent radiation are presented in this section as well. Section 6.3 presents the conclusions.

6.1 Expected radiation power of the THz-CUR at 0.16 THz [1]

Figure 6.1(left) shows the dependence of the bunch form factor on the laser condition. The bunch form factor was converted from the longitudinal particle distribution presented in Chapter 5. The conditions of laser distribution consist of the laser pulse width of 5.8 ps-

FWHM, 10 ps-FWHM, 15 ps-FWHM, and 20 ps-FWHM with a truncated-Gaussian profile, and no space-charge effect. The improvement of the THz-CUR source performance can be confirmed by calculation of the radiated power relating to the value of bunch form factor. The radiated power can be given by integrating the energy spectral density over the frequency, ω, and the solid angle, φ, and by dividing by the radiation pulse width ($N_u\lambda_r/c$). The spectral bandwidth of the CUR radiation ($\Delta\omega/\omega_0$) is about 10%, as calculated from $1/N_u$.

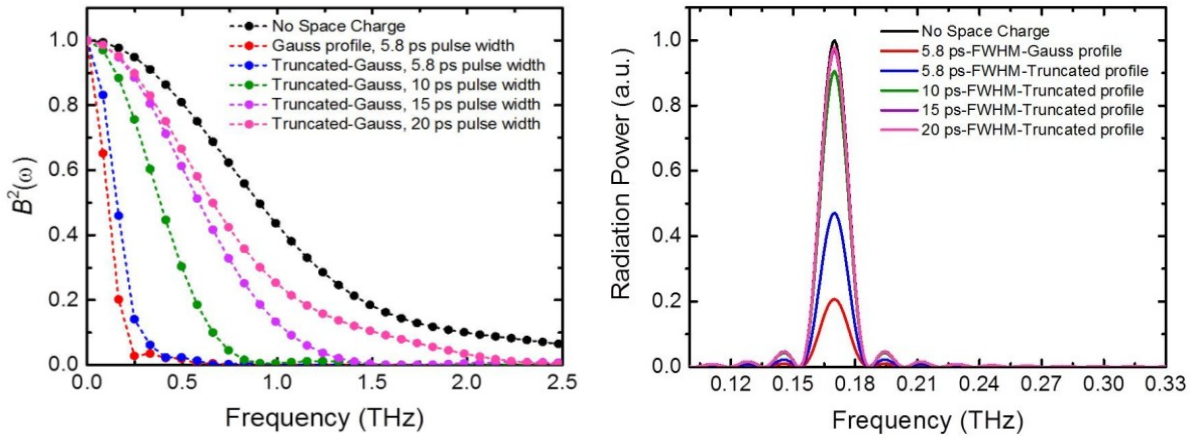

Figure 6.1: (left) Variations in the bunch form factor as a function of the radiation frequency at different laser pulse widths and (right) radiation power spectrum at different laser pulse widths with bunch charge of 160 pC at 0.16 THz and electron energy of 4.6 MeV.

As shown in Fig. 6.1(right), the radiated power increased by 127%, 338%, 369%, and 373% with the transverse profile of truncated-Gaussian distribution and the longitudinal laser distributions at 5.8 ps-FWHM, 10 ps-FWHM, 15 ps-FWHM, and 20 ps-FWHM, respectively. The radiated power raised up to 385% by turning off the space-charge effect. All cases were compared with the power result calculated from the bunch length with the laser pulse width of 5.8 ps-FWHM and the Gaussian transverse profile.

In the experiment, the radiation pulse energy was measured as a function of the bunch charge, as shown with red dots in Fig. 6.2. Despite the saturation of radiation energy, the CUR was still generated with the pulse energy of 1.2 μJ with the bunch charge of 160 pC. The result of using the truncated-Gaussian distribution indicated that the compressed electron bunch is shorter and results in higher radiated power than that when using the Gaussian profile. By applying the truncated-Gaussian profile, the radiation energy is expected to increase from 1.2 μJ to 2.7 μJ, as presented in a blue dot. The result is in good agreement

with the quadratic function of radiation energy versus the bunch charge ($W \propto Q^2 f(\omega)$) to meet the theory of the generation of the CUR. Therefore, the saturation problem of the radiation energy would disappear by using the truncated-Gaussian profile. As shown in Fig. 6.3, enough CUR power at 0.65 THz is successfully generated by using the laser pulse width longer than 10 ps-FWHM.

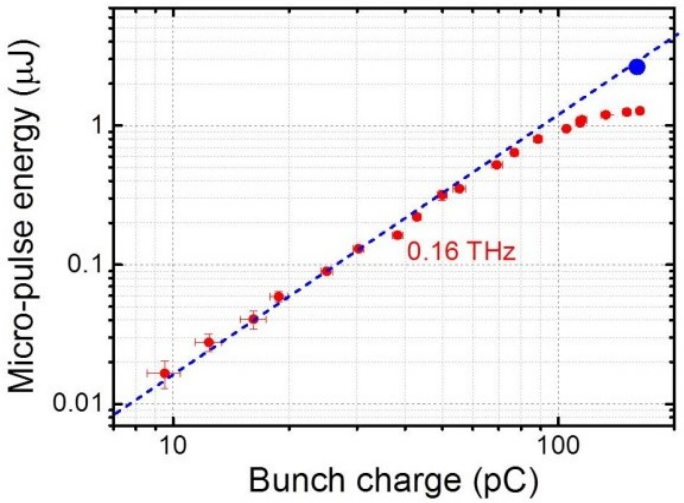

Figure 6.2: Improvement of the saturation of radiation energy at the frequency of 0.16 THz. The red dots are the measured results, and a blue dot is an estimate of the radiation energy for applying a truncated-Gaussian profile.

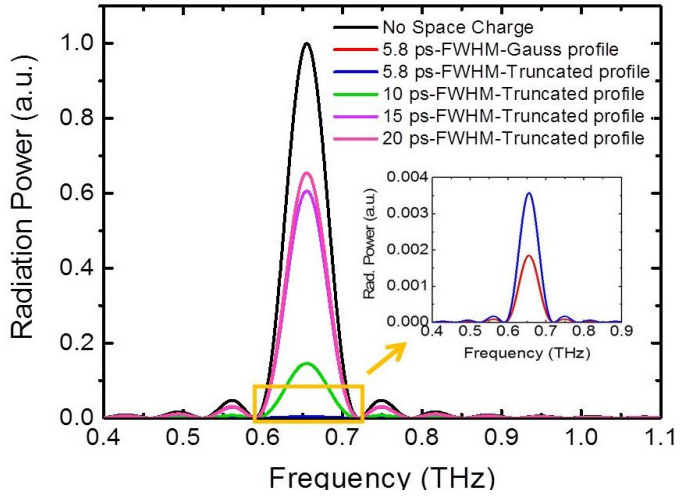

Figure 6.3: Calculated radiation power spectrum at the frequency of 0.65 THz with different laser distributions.

According to the result from the experiment, the THz radiation with the bunch charge of 160 pC from our source can be generated with the peak power of 20 kW at 0.16 THz using

the laser parameters of 5.8 ps-FWHM and the Gaussian profile. The expected radiation power is estimated from the measured peak power, and the result presents in Fig. 6.4. Using of the laser pulse width of 10 ps-FWHM with the transverse truncated-Gaussian profile, the peak power based on the measurement increased greatly up to about 87 kW and 250 kW with the bunch charge of 160 pC and 300 pC, respectively. The result supports the idea of the mitigation of the space-charge effect for achieving an efficient bunch compression to successfully compress the short electron bunch. The THz-CUR can be generated with the peak power of several hundred kW with the bunch charge of 300 pC.

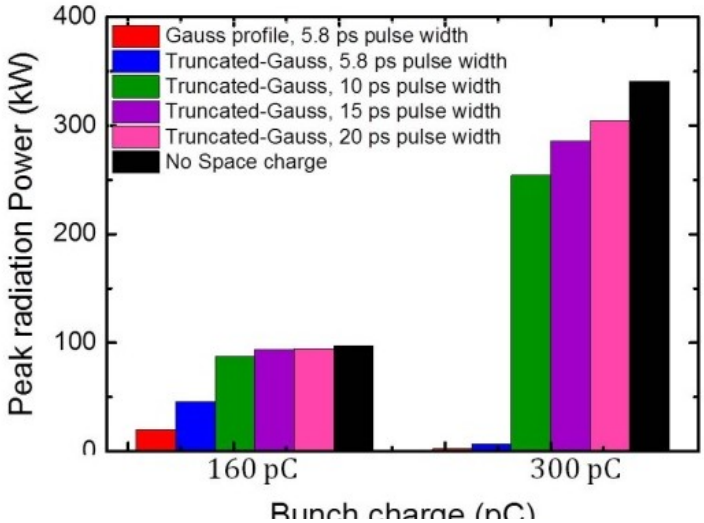

Figure 6.4: Expected radiation peak power at the fundamental frequency of 0.16 THz with the bunch charge of 160 pC and 300 pC.

6.2 Measurement of the manipulation of transverse and longitudinal laser distributions

A laser pulse stacking (LPS) system has been implemented for providing longer laser pulses before illuminating the cathode [2-5]. An iris aperture has been installed to change the transverse profile of the laser beam from Gaussian to truncated-Gaussian distribution before going to excite the cathode. Here the impacts of the transverse truncated-Gaussian distribution and the enlargement of the laser pulse width on the quality of the electron beam and the radiation energy were investigated.

6.2.1 Experimental setups

6.2.1.1 Manipulation of longitudinal laser distribution by using the laser pulse stacking

The longitudinal flat-top laser pulse distribution can be obtained by using the LPS. The setup of LPS is presented in Fig. 6.5. The LPS is composed of a polarizing beam splitter (PBS, PCBS-MF-266-100-FS), a half-wave plate (λ/2 Plate, WPH10M-266), two quarter-wave plates (λ/4 Plate, WPQ10M-266), a fixed mirror, and an optical delay for the delay time adjustment. At first, a UV laser with the pulse width of 5.8 ps-FWHM propagates to a half-wave plate before going to a polarization beam splitter. The laser pulse is divided into s-polarized pulse and p-polarized pulse. The laser intensity is varied by means of wave plate. The laser pulse length is tunable by adjusting the optical delay time of the LPS system. Due to the laser beam hitting the surface of optical components, the loss of laser intensity can occur when passing through the LPS.

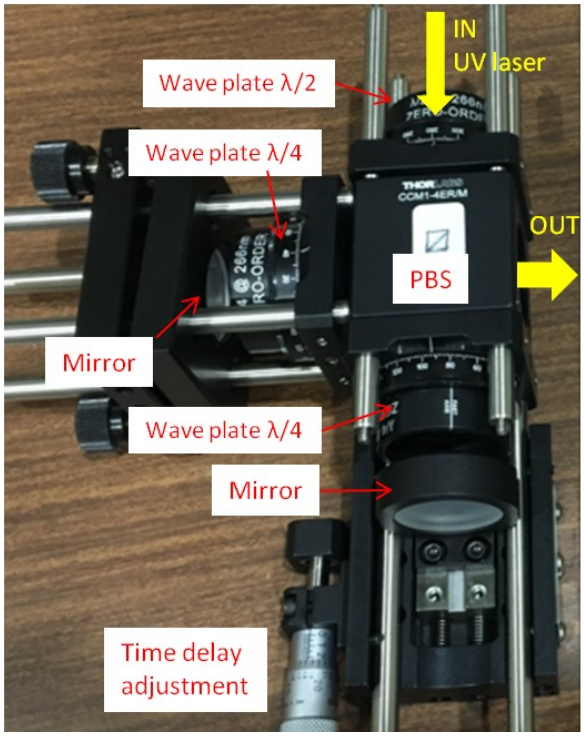

Figure 6.5: Laser pulse stacking (LPS) system.

(a) Single stage of laser pulse stacking (1 stage, 2 pulses)

1. Experimental setup

The schematic of a single stage of laser pulse stacking is shown in Fig. 6.6. The width of each laser pulse is 5.8 ps-FWHM after the wavelength conversion to 266 nm. Using the single stage of LPS, two pulses can be created as shown in Fig. 6.6(right). After the laser pulse passing through the PBS, the pulse propagating from the M side (fixed mirror) is a p-polarized pulse, while the laser pulse from the T side (mirror with time delay adjustment) is s-polarized pulse. An optical path difference can be adjusted by the time delay of T side. A laser intensity of only 75% could travel through the pulse stacker to the cathode. By inserting a fluorescence screen in the front of T side, only p-polarized pulse reflected from the M side was taken out. Also, the only s-polarized pulse was extracted from the T side when blocking the laser pulse with the fluorescence screen prior to the M side.

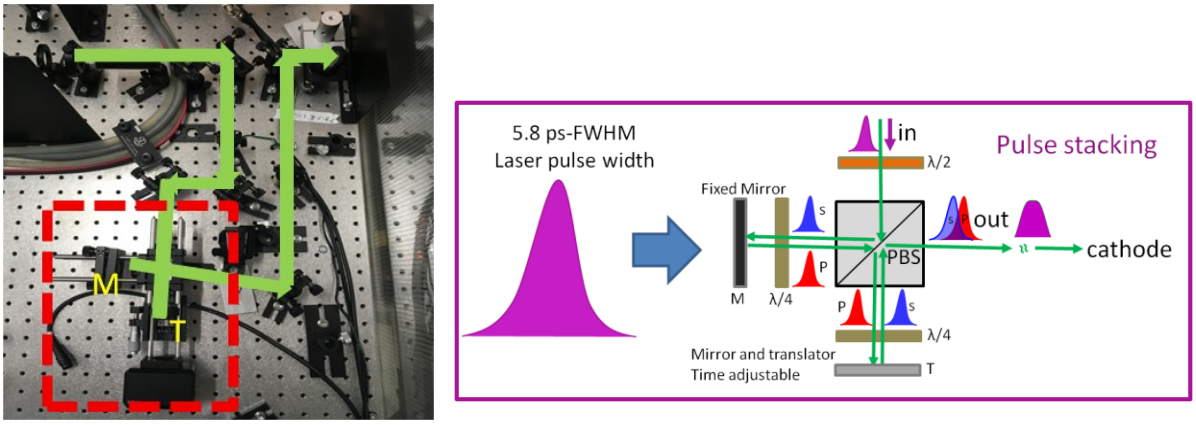

Figure 6.6: (left) Setup of single stage of laser pulse stacking and (right) longitudinal laser distribution from laser pulse stacking.

2. Pulse width estimation

In the photocathode RF gun, the bunch charge of electron beam depends on the incident laser phase. Therefore, the relation between the bunch charge and RF phase can be used to estimate the duration of two laser pulses. So as explained, only each polarization pulse is emitted on the cathode, the bunch charge for each pulse can be measured as a function of the injection phase. The measurement result is shown in Fig. 6.7 presented for the case of the laser energy of 60 μJ/4pulses. The results of p-polarized pulse and s-polarized pulse are presented in the pink and blue lines, respectively. The phase difference of two pulses was about 5 degrees with 2σ time delay. Since the time period of RF pulse is 350 ps for 360

degrees (2π), a time difference is about 1 ps for the phase difference of 1 degree approximately (Fig. 6.8). As mentioned above, the time difference between p-polarized pulse and s-polarized pulse should be about 5 ps and the combined pulse becomes a quasi-flattop distribution with the pulse width of about 10 ps-FWHM as drawn in Fig. 6.9.

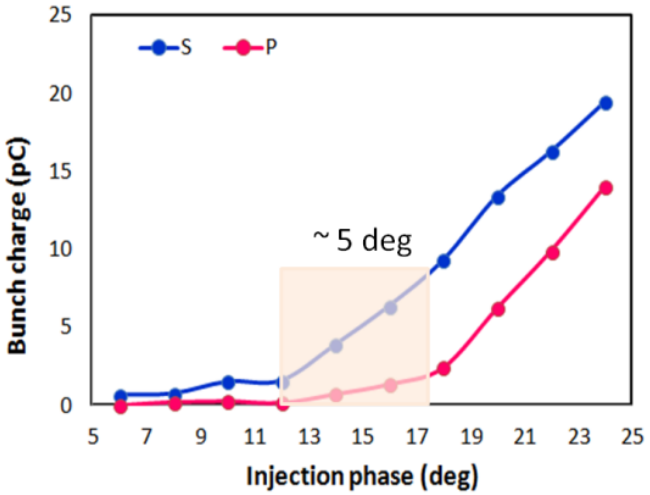

Figure 6.7: RF phase vs. electron bunch charge.

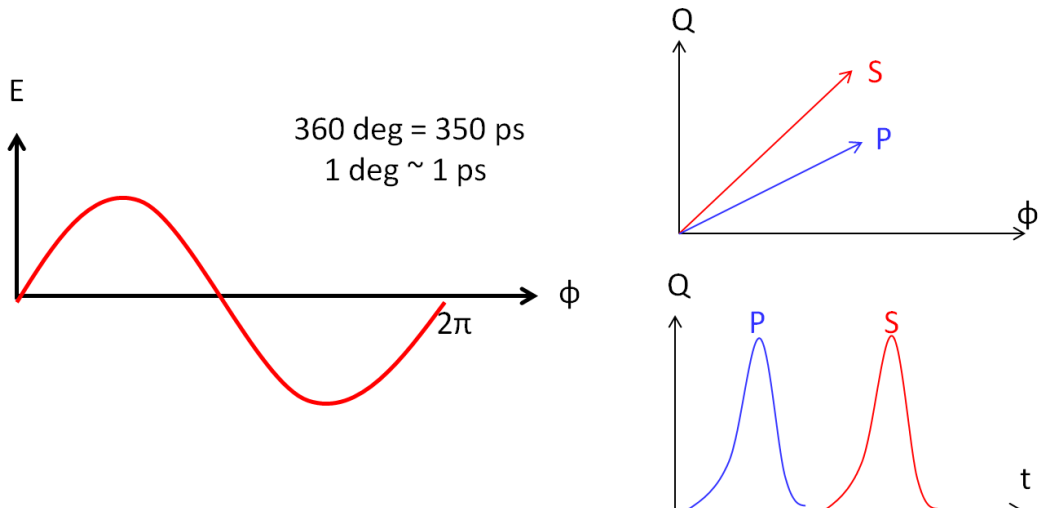

Figure 6.8: Relationship of bunch charge, injection phase and time.

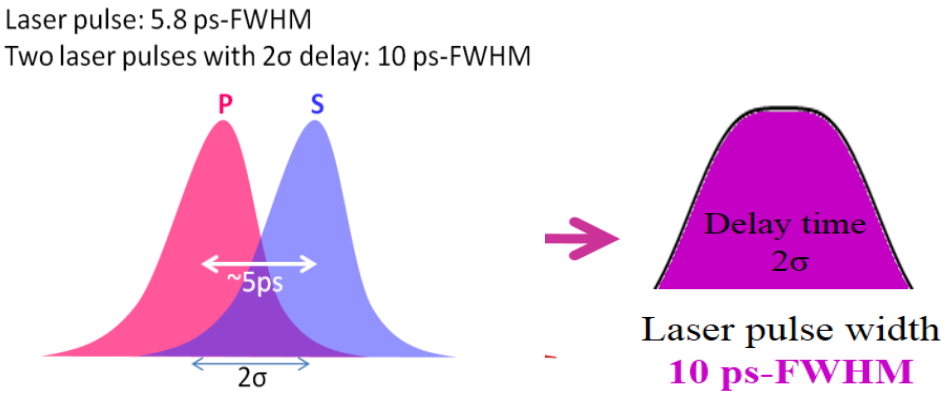

Figure 6.9: Two pulses overlapping with delay time of 5 ps for a laser of 10 ps-FWHM flat-top shape.

(b) Double stages of laser pulse stacking (2 stages, 4 pulses)

Experimental setup and time delay adjustment

The double stages of LPS were set up and installed as shown in Fig. 6.10. To expand the laser transverse size on LPS, the couple lenses consisting of a convex lens (LA4148-UV coated Fused Silica Plana) and a Plana-concave (LC4252-UV coated UVFS) have been installed at downstream of the LPS system. The large laser size allows the decrease of laser density, which can reduce the cause to damage the polarization beam splitter. However, the change of laser size on the cathode may change and will disturb to the electron emission.

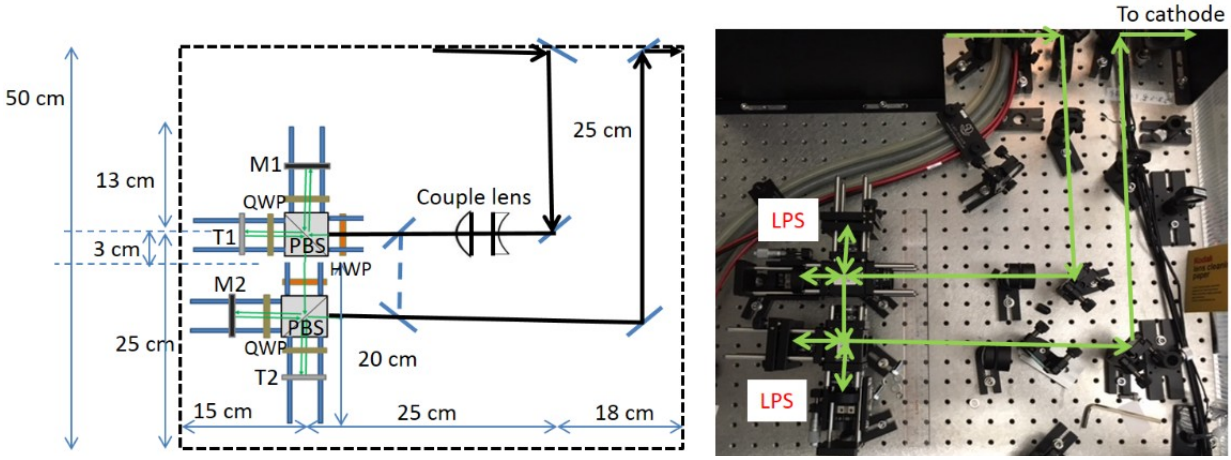

Figure 6.10: Schematic diagram of double stages of laser pulse stacking.

In the step of testing, one pulse of 5.8 ps-FWHM with 40 μJ/pulse was divided into 4 pulses. Each laser pulse was balanced to obtain the same intensity of 10 μJ/pulse by rotating

the angle of wave plates. The overall transmission through the pulse stacker system was about 50%. In order to measure the pulse duration, the method used is the same as used for a single stage of LPS but more complicated. The optical components used for the measurement of each laser pulse are listed in Table 6.1. In order to obtain a 20 ps-FWHM laser pulse width, the time delay has to be adjusted to be 10 ps for the distance of pulse P1 and pulse P2, and the time delay of 5 ps for pulse S1 and pulse P1.

Table 6.1: Optical component used for the measurement of laser pulse duration

Pulse	Mirror used
S1	M1 and T2
P1 (Ref.)	M1 and M2
S2	T1 and T2
P2	T1 and M2

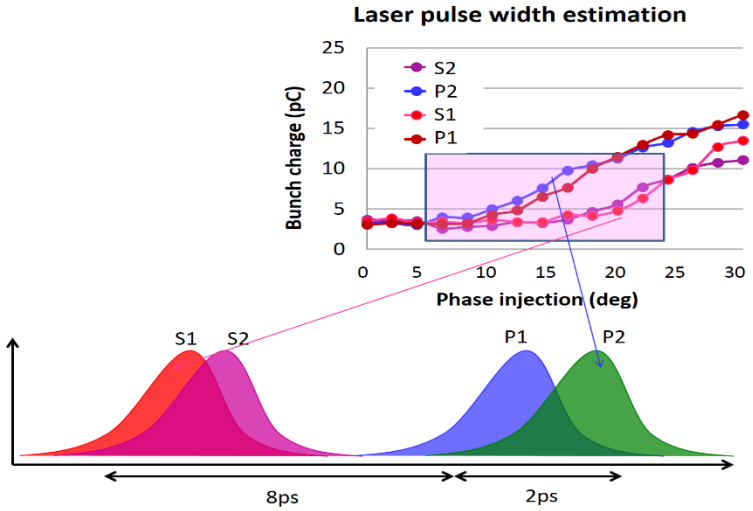

Figure 6.11: Pulse duration in case of the time scale T1 and T2 fixed at 0.2 inch.

Figure 6.11 shows the measured results of the bunch charge and the relative laser injection phase with the initial time scale of T1 and T2 of 0.2 inches. It was found that the phase differences between S1 and P1 were 8 degrees (8 ps time difference) and 2 degrees (2 ps difference) for the P1 and P2 pulses. The optical time delays have to be adjusted as

detailed in Fig. 6.12. The pulse P1 was set and fixed as a reference. Time delays of T1 and T2 were used to adjust the pulse duration of pulse P2 and pulse S1, respectively while the pulse S2 changed automatically.

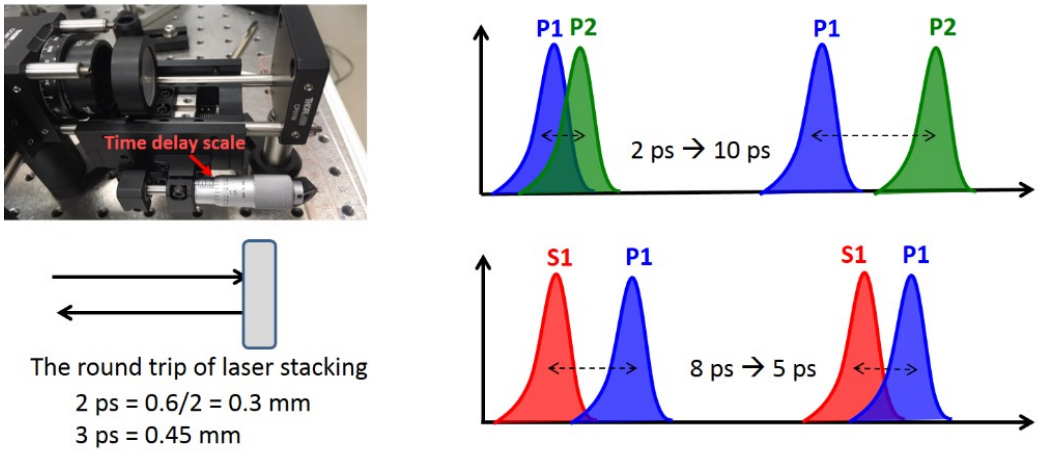

Figure 6.12: Time delay adjustment and the pulse duration arrangement for double stages of laser pulse stacking to obtain 20 ps-FWHM.

Figure 6.13 shows the pulse duration after time delay adjustment. The pulses of S1, P1, S2, and P2 start generating electrons at the phase of 5 degrees, 10 degrees, 15 degrees, and 20 degrees, respectively. According to the phase difference of 15 degrees, the pulse width is about 20 ps-FWHM obtained from this setup. Using the double stages of LPS, the laser pulse can be generated with the 20 ps-FWHM laser pulse of flat-top shape.

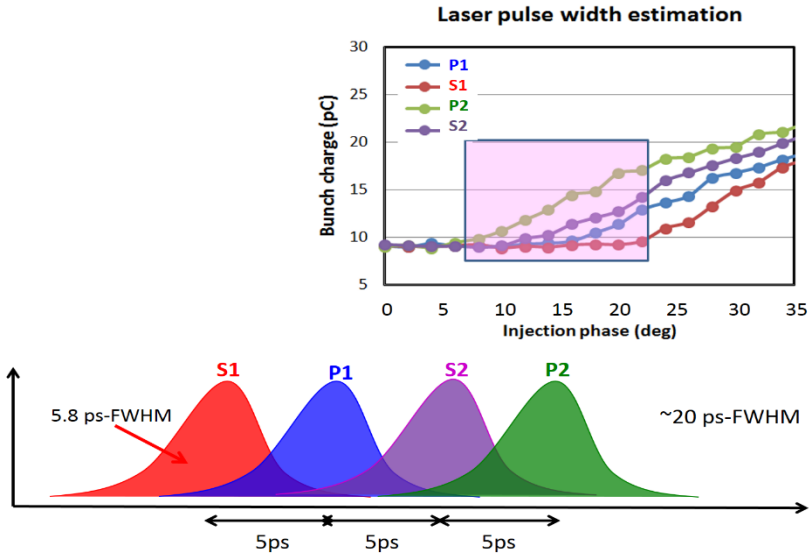

Figure 6.13: a 20 ps-FWHM pulse duration after time delay adjustment.

Although each laser pulse was set the same intensity at 10 μJ/pulse by adjusting the angle of wave plates for the case of the laser intensity with 40 μJ/pulse of 5.8 ps-FWHM, it was found that each pulse could not be emitted with the same charge. The electron bunch shape looks like Trapezoid instead of flat-top distribution as shown in Fig. 6.14. This may be caused by the RF field effect at the beginning of acceleration. However, the study performed by GPT simulation showed that the change of electron shape from flat-top to Trapezoid has no influence on the bunch compression in the bunch charge region lower than 100 pC as shown in Fig. 6.15. The result of electron bunch length is not significantly different at bunch charge of 100 pC.

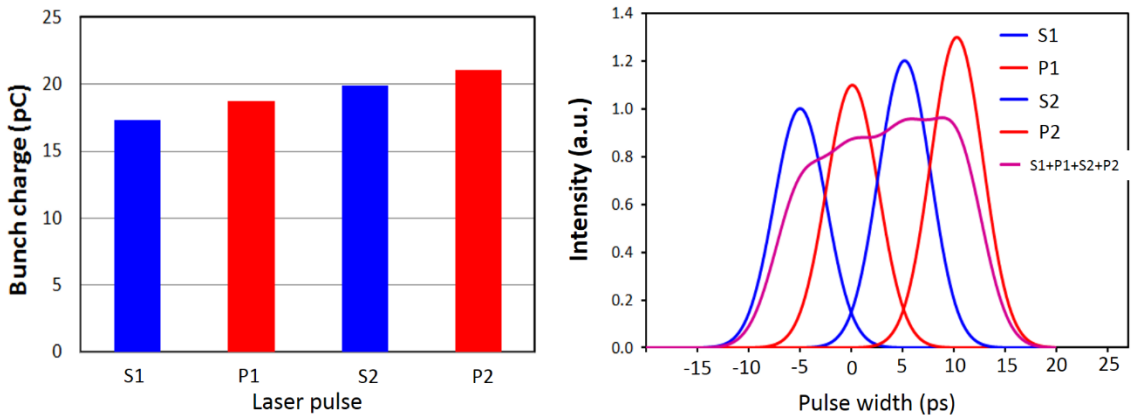

Figure 6.14: Electron bunch shape with the use of double stages of pulse stacking.

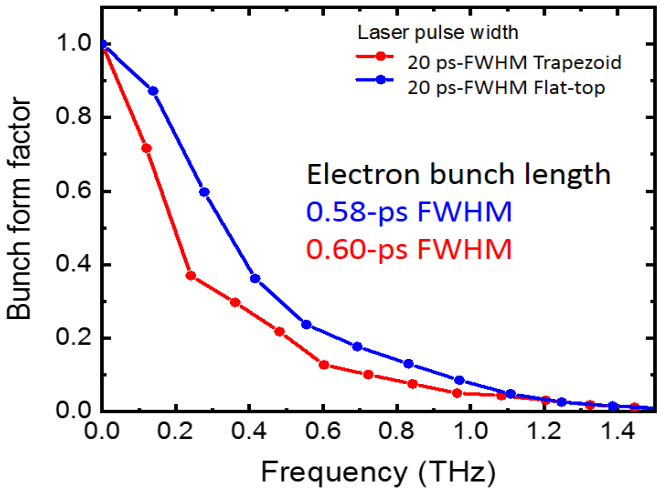

Figure 6.15: Bunch form factor performed by GPT simulation at bunch charge of 100 pC.

6.2.1.2 Truncated-Gaussian laser distribution by aperture clipping

As a result, presented in the previous chapter, we found that the injection of UV laser with the truncated-Gaussian distribution on the cathode is one of the possibilities to get the high efficiency of chicane bunch compression thanks to the reduction of nonlinear space-charge force. In this measurement, the laser pulse width was kept constant at 10 ps-FWHM. Figure 6.16 shows the layout of the iris aperture installation. The transverse truncated-Gaussian profile can be made by clipping a Gaussian laser profile with an aperture before irradiating the cathode.

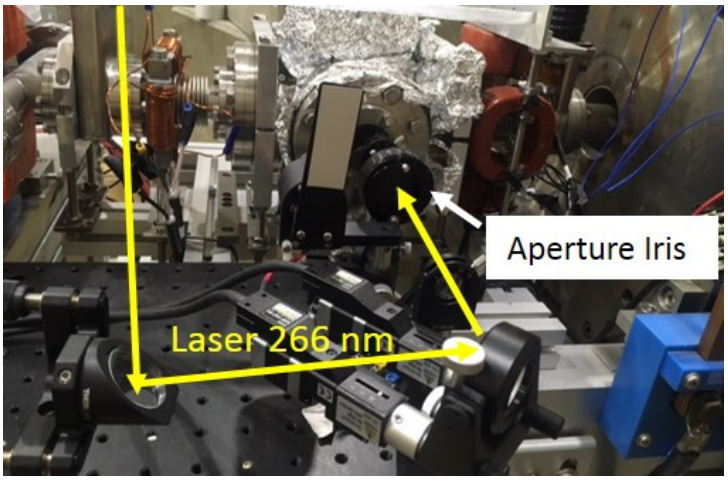

Figure 6.16: Layout of installation of iris aperture.

According to the simulation study, the ratio between the radius of laser size and aperture size (σ_x/r_a) should be the factor of 1. That means the laser profile should be truncated at 0.5 mm whenever the radius of laser spatial distribution is σ_x = 0.5 mm. Unfortunately, the larger size of 0.75 mm-radius was used instead of 0.5 mm-radius of the aperture to make truncated-Gaussian profile because of the high charge fluctuation during the measurement. The setup of iris aperture is shown in Fig. 6.17. The measurement of charge fluctuation is shown in Fig. 6.18 and the result is listed in Table 6.2. The transverse profile can be simply estimated from the size of aperture as shown in Fig. 6.19. However, the laser profile in the real experiment is necessary to be measured. In order to keep the same bunch charge, the laser energy of 50 μJ/pulse was used to excite the cathode in order to generate the electron bunch charge with 80 pC for the case of 0.75 mm aperture while the laser energy used was only 40 μJ/pulse for Gaussian distribution (Fully open aperture).

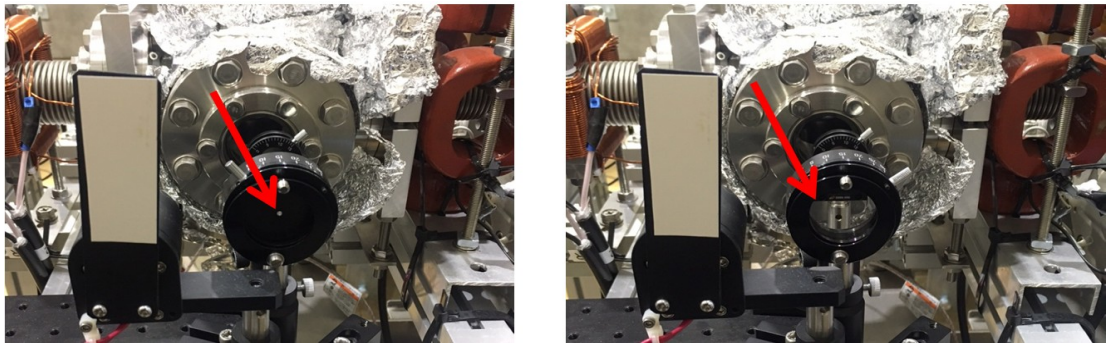

Figure 6.17: Aperture clipping for making a truncated-Gaussian distribution of transverse laser profile for (left) the close aperture of 0.75 mm-radius and (right) fully open aperture.

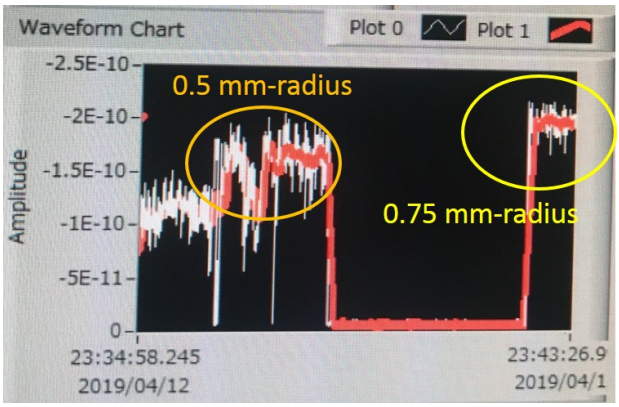

Figure 6.18: Photograph of variation of total charge between 0.5 mm-radius and 0.75 mm-radius aperture size.

Table 6.2: Bunch charge fluctuation after using aperture clipping for the manipulation of the transverse laser distribution.

Aperture size (cm)	Bunch charge (pC)
Fully open	85.05 ± 3.181 pC
0.75 mm-radius	83.38 ± 4.830 pC
0.5 mm-radius	73.17 ± 8.581 pC

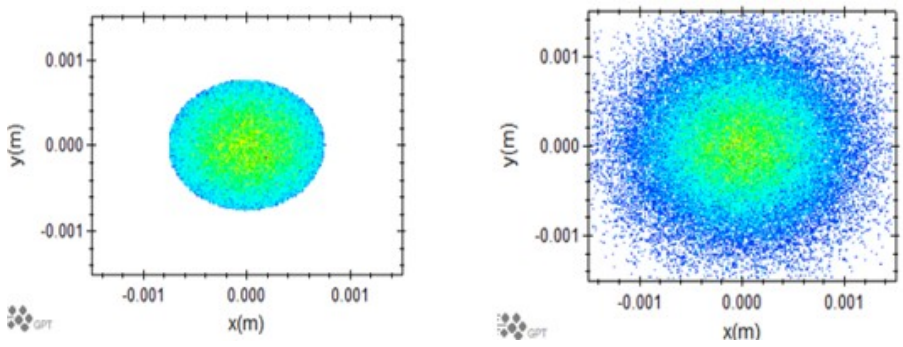

Figure 6.19: Transverse laser profile for (left) the close aperture of 0.75 mm-radius and (right) fully open aperture.

6.2.2 Results and discussion

6.2.2.1 Bunch length estimation

The bunch length can be estimated from CTR spectrum. The details of measurement were explained in Chapter 4. Here, the inconel coated pellicle beam splitter was used instead of the sapphire plate beam splitter (BS) because the radiation is not absorbed in the frequency range lower than 1 THz but this BS has low intensity-transmission efficiency. The CTR interferogram for each bunch charge was measured and varied with the range of path difference from −0.4 cm to +0.4 cm and a step size of 0.05 cm (Fig. 6.20(left)). The amount of electron charge was adjusted by changing the energy of UV laser on the cathode. The laser energies used were 15 μJ and 50 μJ/pulse for the electron generation with the bunch charge 30 pC and 90 pC, respectively. The machine parameters for providing the maximum intensity CTR were the injection phase of 12 degrees, solenoid current of 100 A, and chicane current of 5.7 A. Figure 6.20(right) shows the bunch form factor from the CTR power spectrum. It was obtained by the fast Fourier transform of the measured CTR interferogram. It can be seen that the bunch form factor at 90 pC is lower than that at 30 pC. The bunch length at 30 pC charge is about 0.87 ps-FWHM longer than that from GPT simulation (0.4 ps-FWHM).

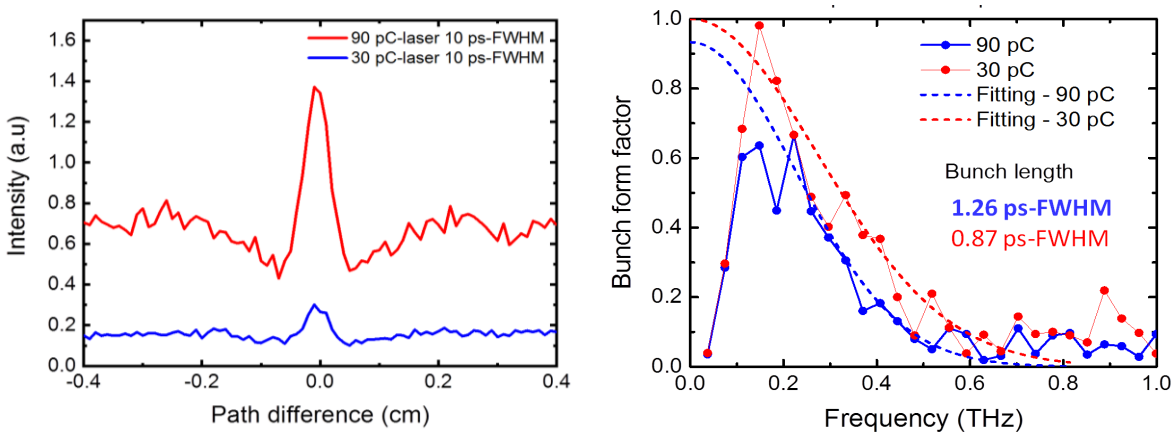

Figure 6.20: (left) CTR interferogram and (right) CTR power spectrum (bunch form factor) for the bunch charge of 30 pC and 90 pC with single stage of LPS.

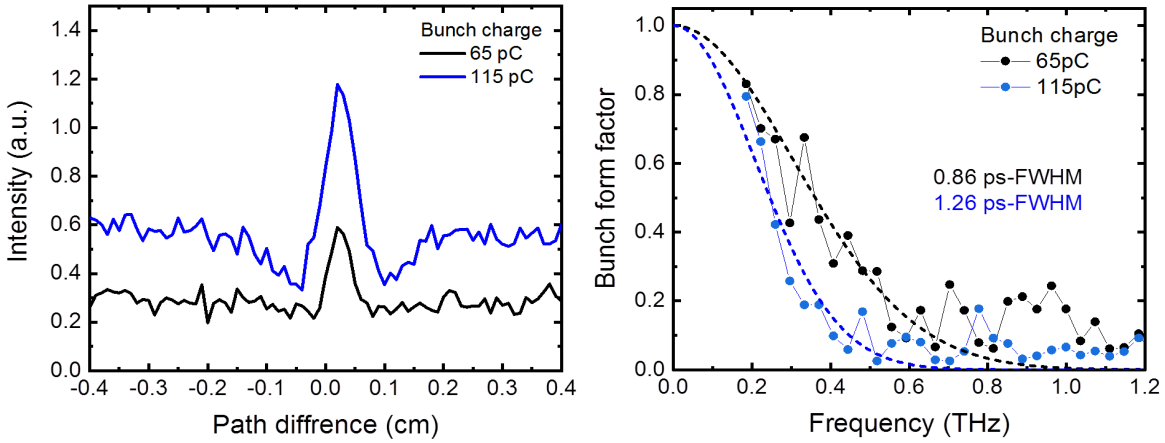

Figure 6.21: Using laser pulse width of 20 ps-FWHM, CTR interferogram and CTR spectrum with the bunch charge of 65 pC and 115 pC.

In Fig. 6.21 one can see the bunch form factor using the 20 ps-FWHM performed from CTR. With the bunch charge of 65 pC, the bunch form factor was increased and the maximum frequency of about 1.0 THz was obtained, but it was limited at 0.7 THz for the bunch charge of 115 pC. The estimated bunch lengths were about 0.86 ps-FWHM and 1.26 ps-FWHM for 65 pC and 115 pC, respectively. At the bunch charge of 115 pC, the bunch length can be shortened 37% when enlarging the laser pulse width 5.8 ps Gaussian to 20 ps-FWHM flat-top shape.

Figure 6.22 shows the bunch form factor estimated from CTR spectrum at different laser distributions and at the bunch charge of 80 pC. It was found that the bunch form factor using 10 ps-FWHM laser pulse is higher than that from 5.8 ps-FWHM. The electron bunch length

was compressed to 1.26 ps at a charge of 80 pC. This result guarantees that the space-charge effect is mitigated by changing the longitudinal laser distribution. The use of truncated-Gaussian laser profile allows us to get higher bunch form factor than that from a Gaussian profile. The bunch form factor can cover the frequency up to 0.8 THz. The electron bunch length generated with truncated-Gaussian laser profile was about 0.92 ps-FWHM and shorter than that with Gaussian distribution.

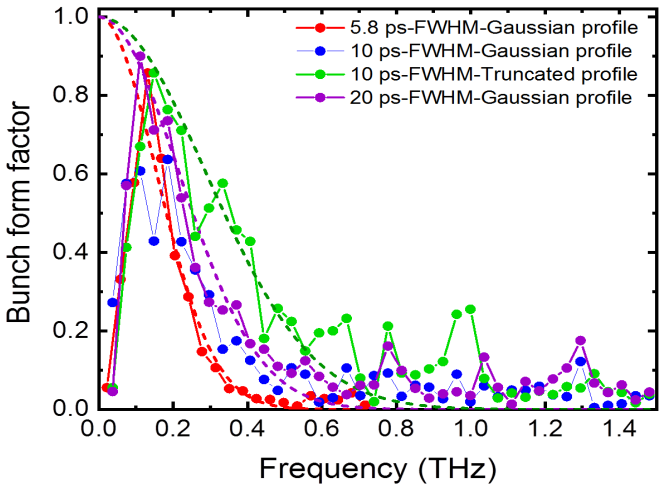

Figure 6.22: Comparison of bunch form factor estimated from CTR at the bunch charge of 80 pC.

Table 6.3: Compressed electron bunch length at the bunch charge of 80 pC.

Condition of laser distributions	Compressed electron bunch length
Laser pulse width of 5.8 ps + Gaussian profile	1.58 ps-FWHM
Laser pulse width of 10 ps + Gaussian profile	1.26 ps-FWHM
Laser pulse width of 10 ps + truncated profile	0.92 ps-FWHM
Laser pulse width of 20 ps + Gaussian profile	1.15 ps-FWHM

6.2.2.2 Total radiation energy

The experiment setup for measuring the total radiation energy was detailed in chapter 3. The measurement was performed at the undulator gap of 50 mm for generating THz-CUR at the frequency of 0.51 THz. The detector installation has to be considered at the same position for all cases. Figure 6.23 shows the dependence of total radiation energy at different laser pulse distribution. With the laser pulse of 10 ps flat-top, the radiation energy using truncated-Gaussian profile can be increased by 70% compared to Gaussian distribution at the same bunch charge of 80 pC. The total radiation energy for the case of 20 ps laser pulse width is lower than that with using 10 ps-FWHM laser pulse width. However, in the bunch charge region higher than 80 pC, the total radiation energy seems higher than that with using the original laser pulse of 5.8 ps-FWHM Gaussian shape. As a result, applying the laser distribution with 10 ps-FWHM laser pulse width and truncated-Gaussian profile would be a reasonable and acceptable condition for the present situation of our machine.

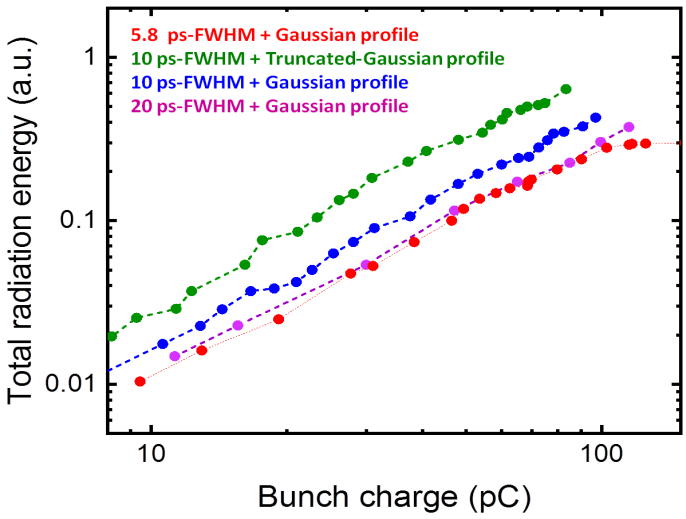

Figure 6.23: Total radiation energy of THz-CUR with the undulator gap of 50 mm (0.51 THz) as a function of bunch charge by using truncated-Gaussian and Gaussian transverse distribution.

In addition, the generation of bunch charge using 0.75 mm aperture radius is more stable than that with 0.5 mm-radius because of lower charge fluctuation (Table 6.2). The radiation intensity deviation using an aperture size of 0.75 mm-radius is about 50% lower than that with 0.5 mm-radius as shown in Fig. 6.24. It causes by the stability of laser pulse when passing through the iris aperture.

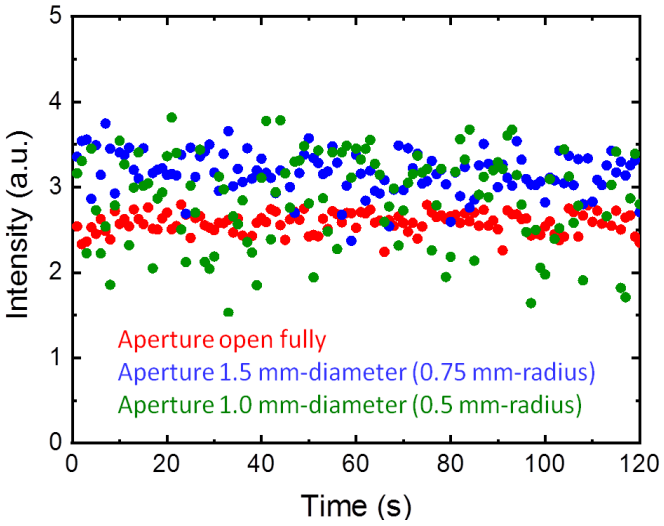

Figure 6.24: Comparison of intensity on the aperture size of open aperture fully, 0.75 mm-radius, and 0.5 mm-radius with fixed bunch charge of 80 pC.

6.2.2.3 Discussion

After applying a longer flat-top laser pulse width and changing the laser transverse profile to truncated-Gaussian distribution, a shorter bunch length was successfully generated. At the bunch charge of 90 pC, the result of bunch form factor obtained from CTR measurement using 10 ps-FWHM laser pulse width is in good agreement with performed from GPT simulation but not for the bunch charge of 30 pC (Fig. 6.25). It was found that at the low bunch charge region, the bunch length was twice longer than that from GPT simulation. The reason for that is maybe because of transverse bunch form factor. The effect of the transverse size of the electron bunch has a significant impact on the total bunch form factor. Sufficient focusing of the electron beam is necessary to suppress transverse effects, otherwise, it will disturb to the total bunch form factor. In the real measurement, the transverse and longitudinal size effects could not be separated.

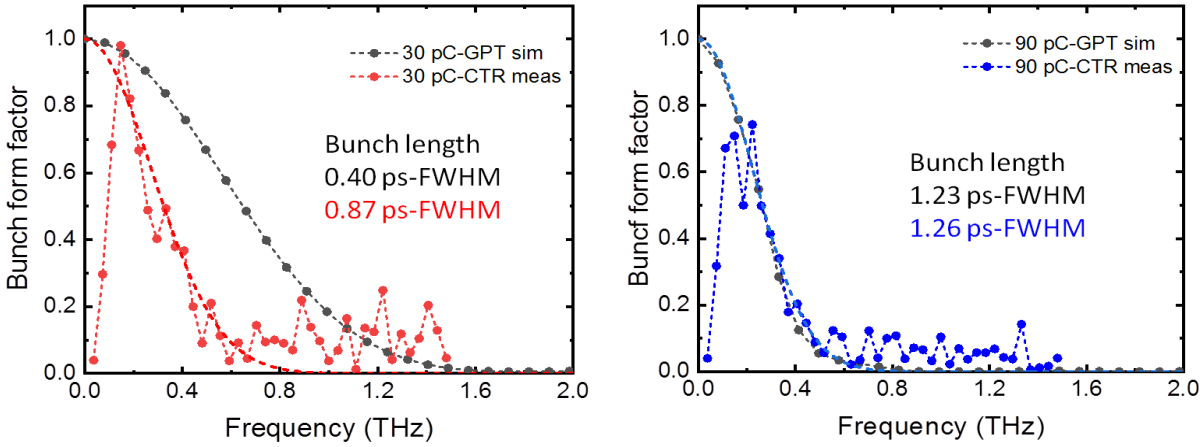

Figure 6.25: Comparison of bunch form factor obtained from CTR measurement and GPT simulation at the bunch charge of (left) 30 pC and (right) 90 pC.

For coherent radiation, the bunch form factor from the normalized three-dimensional particle distribution $S_{3d}(\vec{r})$ is given by [6]

$$f(\vec{k}) = \left| \int S_{3d}(\vec{r}) e^{i\vec{k}\cdot\vec{r}_j} d^3r \right|^2 \tag{6.1}$$

The total bunch form factor can be obtained in the form

$$f_{3d} = B_{3d}^2(k_x, k_y, k_z) = e^{-\sigma_z^2 k_z^2} e^{-\sigma_{x,y}^2 (k_x^2 + k_y^2)} \tag{6.2}$$

where $k_x^2 + k_y^2 = (\omega \sin\theta / c)^2$, $k_z = \omega \cos\theta / c$, ω is the angular radiation frequency, θ is the observation angle of $1/\gamma$.

From GPT simulation, Figure 6.26 shows that the bunch form factor is not dependent on transverse beam size because the transverse beam size can be completely focused to 0.2 mm in both horizontal and vertical directions by using Triplet quadruples. Since the beam size at CTR station could not be measured, the beam size was estimated from the electron beam on the screen monitor inside undulator as shown in Chapter 4. Assuming the beam size in the real experimental condition would be about 1.0 mm and 0.5 mm in horizontal and vertical directions, respectively. Figure 6.27 shows the transverse beam size of the electron bunch has a significant influence on the total bunch form factor, especially with a short bunch length. For the case of 0.5 ps-FWHM bunch length, the longitudinal bunch form factor lies over 1.5 THz frequency (blue line) but the range of covering the frequency reduces less than 1 THz after including the transverse beam size. Due to the large transverse beam size, the measured bunch form factor was lower than that from GPT simulation even the beam optics

were optimized by using Triplet quadrupoles. There is reasonably good agreement between the decrease of transverse bunch form factor and the total bunch form factor obtained from the beam size in the actual machine.

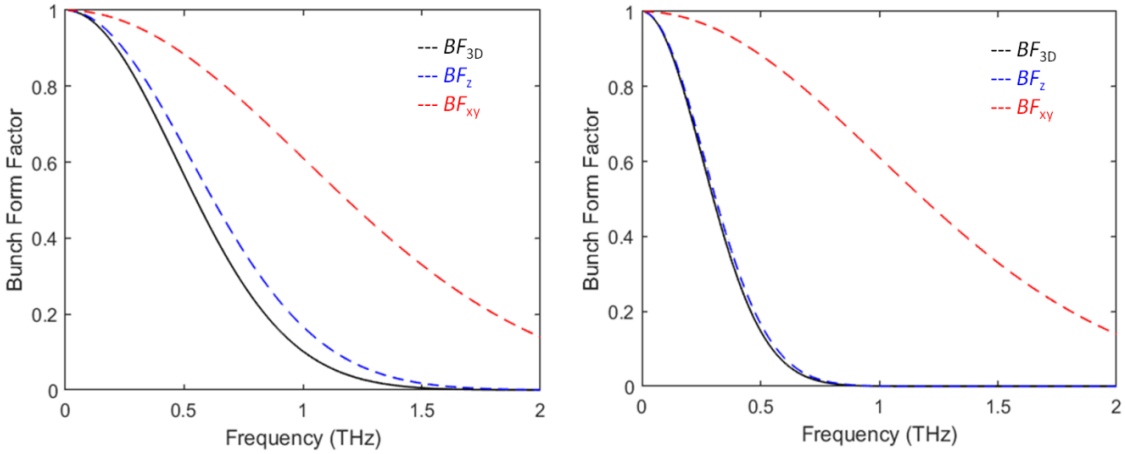

Figure 6.26: Bunch form factor with the bunch length of (left) 0.5 ps-FWHM and (right) 1.0 ps-FWHM with transverse beam size simulated from GPT code at CTR station.

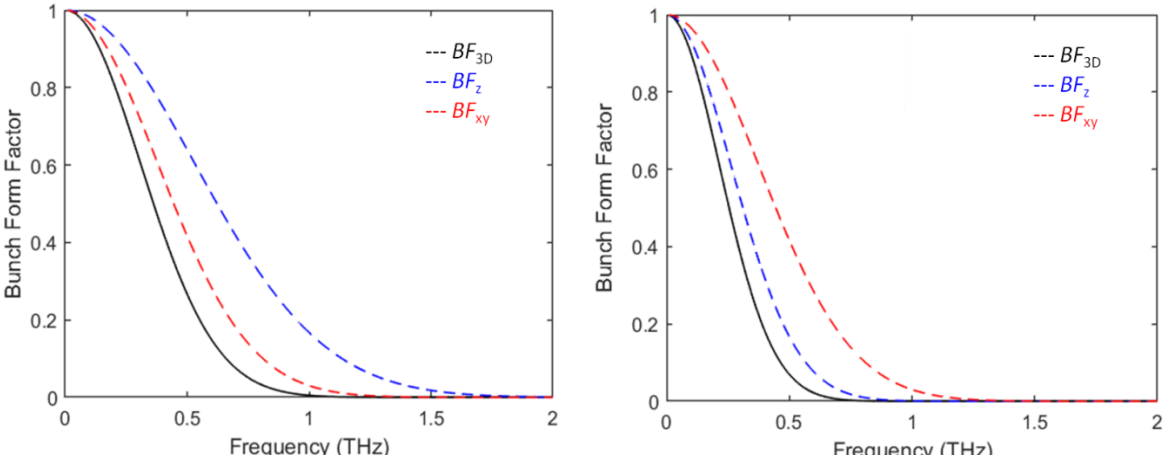

Figure 6.27: Bunch form factor with the bunch length of (left) 0.5 ps-FWHM and (right) 1.0 ps-FWHM with transverse beam size estimated on screen monitor located inside undulator.

As discussed in Chapter 4, significant improvements of source performance have been achieved by the high quality of electron beam. In actual machine condition, the generation of coherent undulator radiation depends on the electron beam quality affected by many parameters such as space-charge effect, RF effect, energy spread, etc. Figure 6.28 shows the measured results of the energy spread at different laser conditions. It was found that the energy spread with the laser pulse width of 20 ps-FWHM is increased by 70% more than that

using the 5.8 ps-FWHM laser pulse. While the energy spread keeps unchanged when increasing laser pulse width from 5.8 to 10 ps-FWHM and changing the laser transverse profile from Gaussian to truncated-Gaussian distribution.

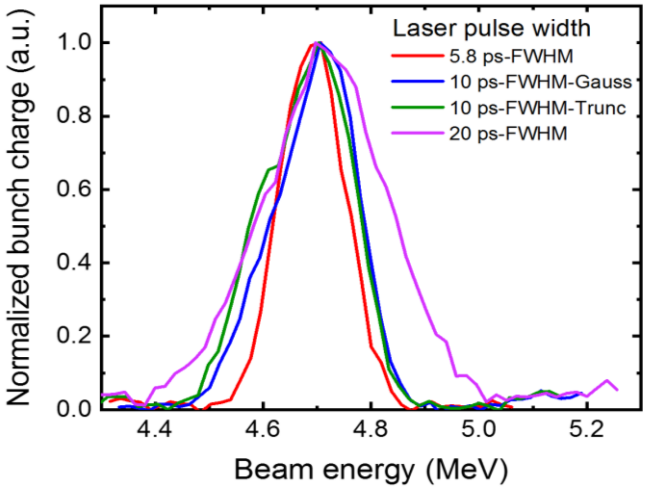

Figure 6.28: Bunch charge as a function of electron beam energy for estimating energy spread.

Although a long laser pulse width can reduce the space-charge force, it leads to the large energy spread and emittance. The emittance induced RF effect is dominant with $c\sigma_x^2\sigma_z^2$, given by [7]

$$\varepsilon_{rf} = 4\sqrt{2}\pi^3 \frac{\alpha f^3}{c}\sigma_x^2\sigma_b^2 \tag{6.3}$$

It can be easily written in practical unit

$$\varepsilon_{rf}[\text{mm mrad}] = 2.73 \times 10^{-11} E_0[\text{MV/m}]\, f^2[\text{MHz}]\sigma_x^2[\text{mm}]\sigma_b^2[\text{ps}] \tag{6.4}$$

where E_0 is the accelerating field, σ_x and σ_b are rms radius and bunch length, respectively.

Since the enhancement of total radiation energy at high frequency region is dependent on emittance growth, the radiation power with the laser pulse width of 20 ps-FWHM cannot be increased higher than that using 10 ps-FWHM. The reason for that is because the increase of the laser pulse width to 20 ps-FWHM not only results in the decrease of the space-charge contribution to the longitudinal phase space but also increases the emittance growth due to the effect of RF field. Thus the use of laser pulse width to 20 ps-FWHM will be not proper to meet our goal of the enhancement of the radiation power. Increasing a laser pulse width to 20

ps-FWHM, the space-charge effect can be mitigated but RF effect is dominant. The balancing between space-charge effect and RF effect is needed in order to reduce the bunch length and also other properties of electron beam.

Moreover, the spatial distribution was measured and carried out at the bunch charge of 115 pC and the undulator gap of 50 mm. The result of spatial distribution is illustrated in Fig. 6.29 at different laser pulse width. It was found that the spatial distribution when using 20 ps-FWHM laser pulse width is larger than that of 5.8 ps-FWHM laser pulse width. The overlap factor calculated from spatial distribution using laser pulse 20 ps-FWHM is about 0.37 while the overlap factor using laser pulse 5.8 ps-FWHM is about 0.5. This may be because the quality of electron beam is degraded.

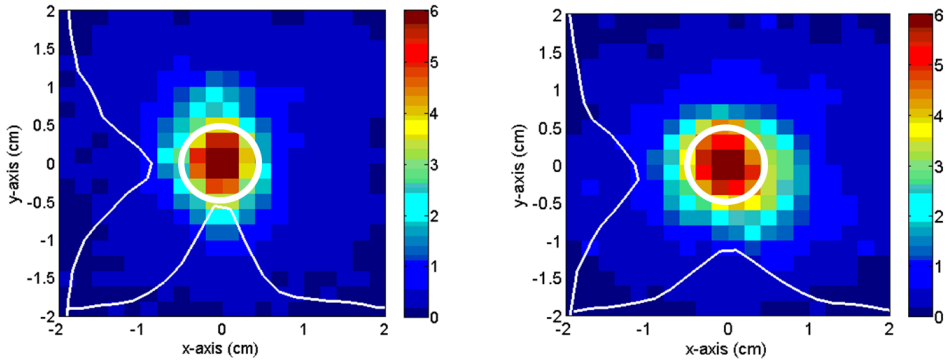

Figure 6.29: Spatial distribution with the bunch charge of 115 pC between using (left) 5.8 ps-FWHM and (right) 20 ps-FWHM.

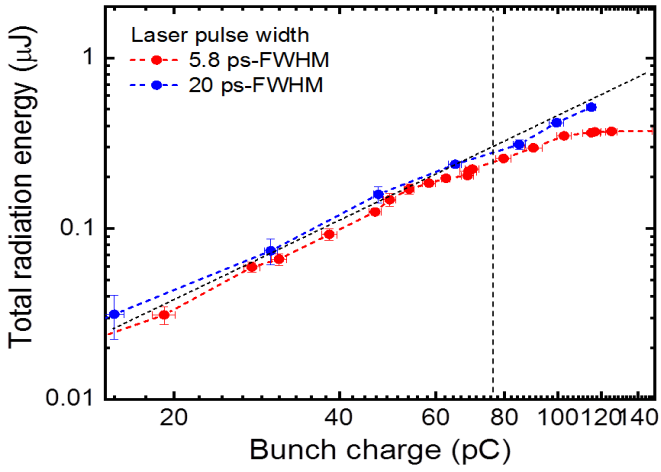

Figure 6.30: Total radiation energy at a frequency of 0.51 THz (Undulator gap of 50 mm).

In order to estimate the total radiation energy, spatial distribution should be taken into account. The plot of the total radiation energy as a function of bunch charge in Fig. 6.30 is

compared between the use of laser pulse widths of 5.8 ps-FWHM and 20 ps-FWHM. At the bunch charge of 115 pC, the total radiation energy increases by 30% compared to the case of using 5.8 ps-FWHM. However, to avoid the effect as mentioned above, the use of 10 ps-FWHM laser pulse and truncated-Gaussian profile would be a good condition for enhancement of THz radiation power, guaranteed from the measured result of THz-CUR intensity in Figure 6.23. The investigation of total radiation energy at other frequencies is required and will be further measured to confirm the improvement of THz-CUR in the whole frequency range. The other effects perturbing on the radiation would occur and be necessary to be studied more in-depth.

In order to reduce the space-charge effect without resulting in the emittance growth induced RF effect or energy spread, the longitudinal laser pulse width may be kept at 10 ps-FWHM but its shape will be changed from flat-top to ellipsoidal pulse as compared in Fig. 6.31. The study reported in Ref. [8] showed that the ellipsoidal distribution can reduce the space-charge dominated beams and also provide a good quality of electron beam. In addition, the stability of electron beam using the ellipsoidal pulse was proved that it is better than that using other laser shapes.

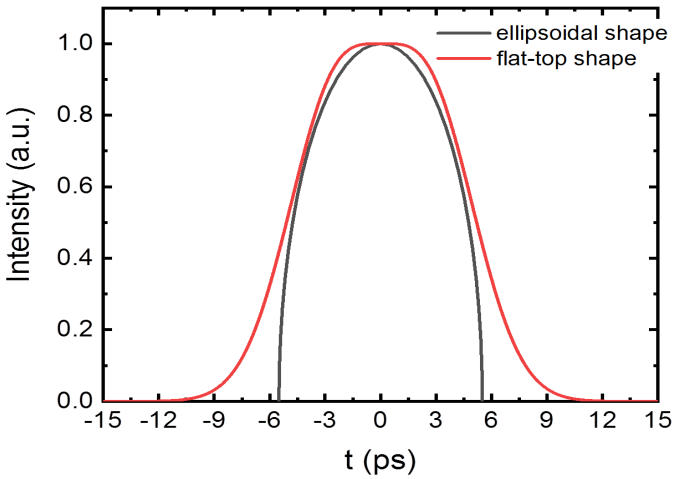

Figure 6.31: Longitudinal laser distribution with quasi-flattop and ellipsoidal shape of 10 ps-FWHM.

Figure 6.32 presents the simulation results of electron bunch length and bunch form factor performed from GPT simulation for the use of quasi-flattop and ellipsoidal shapes of 10 ps-FWHM pulse width. The laser of truncated-Gaussian transverse profile was used both in two cases. With ellipsoidal shape, the bunch form factor is higher than that the case of

quasi-flattop shape and the bunch length can be compressed to 1.30 ps-FWHM, shorter than that from quasi-flattop shape at the bunch charge of 300 pC. Using the longitudinally ellipsoidal shape of 10 ps-FWHM with truncated-Gaussian transverse profile would be a good candidate for the mitigation of space-charge effect and also restrain the emittance growth due to RF effect.

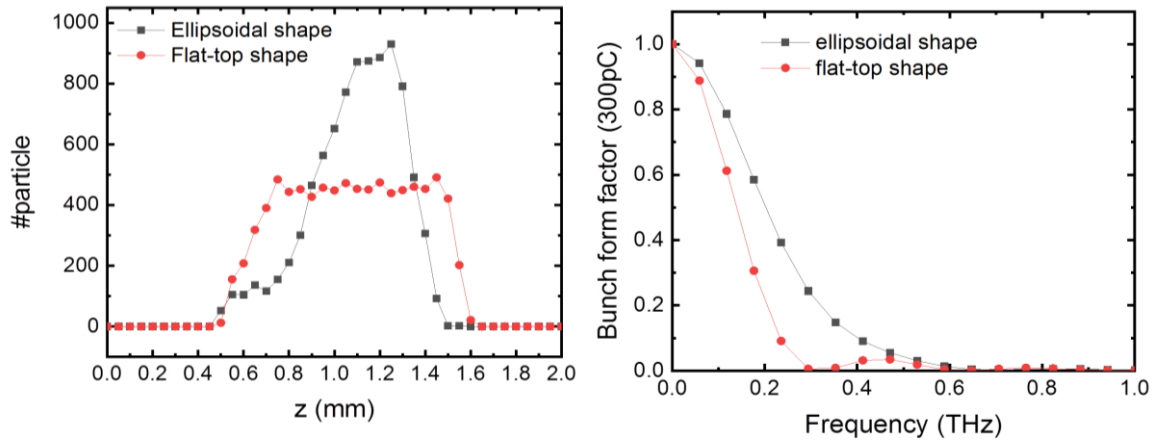

Figure 6.32: (left) Longitudinal particle distribution and (right) bunch form factor for the laser pulse of quasi-flattop and ellipsoidal shape with 10 ps-FWHM and truncated-Gaussian profile at 300 pC bunch charge.

6.3 Conclusions

In this chapter, the improvement of THz source performance was experimentally studied. The techniques of laser pulse shaping in both Transverse and longitudinal directions have been developed and used to mitigate the space-charge effect in electron bunches. The method to manipulate the laser shape would allow decreasing the space-charge force and obtaining the short bunch length electron beam after bunch compression. The measurement result of the bunch form factor at high bunch charge was in good agreement with the simulation result. Although the bunch length with using the laser pulse with 20 ps-FWHM of flat-top distribution was shorter than that using 10 ps-FWHM pulse, the other electron beam properties such as energy spread and emittance got worse in quality. The measured results of the total radiation intensity indicated that the use of 10 ps-FWHM width with truncated-Gaussian profile was higher than that with other ones and the bunch length was shorter than that with other laser's shape. Therefore, the use of a laser pulse of truncated-Gaussian laser profile with 10 ps-FWHM pulse width would be a good candidate of laser condition to

mitigate the space-charge effect and to prevent the trouble of other effects on the generation of THz radiation.

The chapter reported in the journal and proceeding as follows

1. S. Krainara, *et al*., "Manipulation of laser distribution to mitigate the space-charge effect for improving the performance of a THz Coherent Undulator Radiation source", *Particles* **2018**, 1(1), pp.238-252.
2. S. Krainara, *et al*., "Impact of the transverse and longitudinal distributions of the photocathode excitation laser distribution on the generation of THz Coherent Undulator Radiation at Kyoto University", in preparation.

6.4 References

[1] S. Krainara, *et al*., "Manipulation of laser distribution to mitigate the space-charge effect for improving the performance of a THz Coherent Undulator Radiation source", *Particles* **1**(1), pp. 238-252 (2018).

[2] B. L. Beaudoin, *et al*., "Longitudinal bunch shaping of picosecond high-charge MeV electron beams", *Phys. Plasmas* **23,** 103107 (2016).

[3] K. Hyun, *et al.*, "Longitudinal laser pulse shaping for low-emittance electron-beam generation". *J. Korean Phys. Soc.* **54**, pp. 381–385 (2009).

[4] J. Yang, *et al.*, "Low-emittance electron-beam generation with laser pulse shaping in photocathode radio-frequency gun", *J. Appl. Phys* **92**, 1608 (2002).

[5] C. Kim, *et al.*, "Laser pulse shaping for generation of low-emittance electron beam", in *Proc. o*f FEL, Gyeongju, Korea, TUPPH019, pp. 278–281 (2008).

[6] O. Grimm, *et al*., "Transverse electron beam size effect on the bunch profile determination with coherent radiation diagnostics", in *Proc.* of EPAC, Genoa, Italy, TUPC030, pp. 1113-1115 (2008).

[7] C. Travier, "An introduction to photo-injector design", *Nucl. Instrum. Methods Phys. Res. A* **340**, pp. 26-39 (1994).

[8] T. Rublack, *et al.*, "Development of a quasi 3D ellipsoidal photo cathode laser system for PITZ", in *Proc.* of IPAC, Dresden, Germany, WEPRO055, pp. 2069-2071 (2014).

Chapter 7

Physical design of THz-CUR Transport beamline at Kyoto University

7.1 Introduction

Since the dangerous radiations (e.g., gamma rays and neutrons) can be generated during accelerator machine operation, the accelerator source has to be separated into the user station for radiation safety. The transport beamline has to be considered for collecting overall radiation and providing a high transmission ratio of the THz radiation along a long distance from the source to the user station. At Kyoto University, the intense terahertz coherent undulator radiation (THz-CUR) in the frequency range of 0.16–0.65 THz can be generated from a compact accelerator. In this frequency region, THz radiation easily diverges because of having large diffraction. In order to transfer the THz radiation with the high transmission ratio, optical components apart of transport beamline have to be carefully designed and arranged, otherwise, the intensity would extremely lose during traveling to user station. The aim of this study is to present a potential way to control THz radiation especially in low-frequency below 1 THz propagating along THz transport beamline to prevent the loss of intensity THz radiation. Here, the arrangement of optical components for transport beamline would allow THz beam transmitting with high intensity of transmission. The design concept

of the transport system is shown in Section 7.2. Section 7.3 presents the results of beam diameter and intensity of transmission. Section 7.4 describes the potential way to increase the intensity transmission ratio of THz radiation. Finally, conclusions are given in Section 7.5.

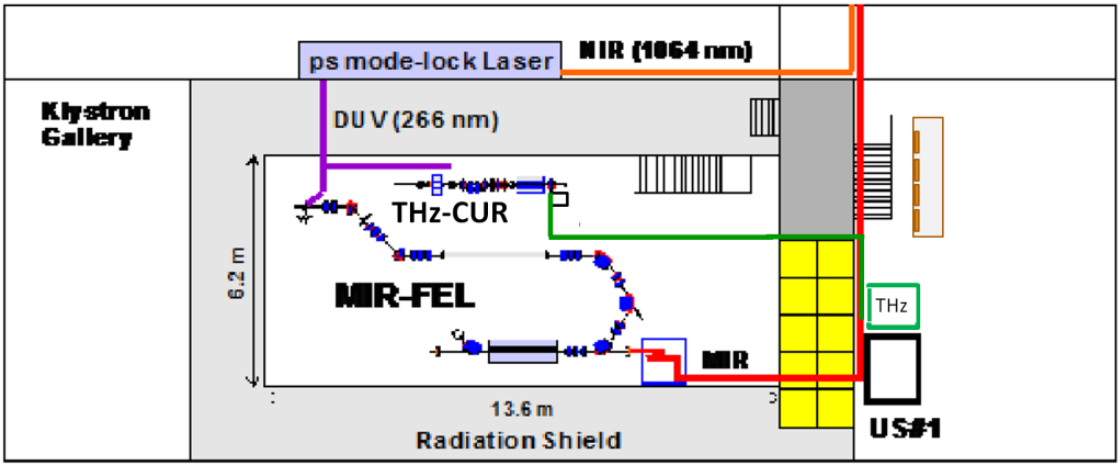

Figure 7.1: Layout of THz-CUR source and the KU-FEL (MIR-FEL) at Kyoto University. The THz transport line in a green line is about 18 meters.

As for propagation of the THz-CUR to the user station, the overall optical path is about 18 meters as drawn in the green line of Fig. 7.1. The source and the user station are separated with a concrete wall for radiation protection. The transport beamline consists of several optical components to transfer the radiation. It is notable that the THz optical path is installed in the air environment because the absorption in the air with normal humidity has no significance for THz radiation in the low-frequency region lower than 1 THz [1].

7.2 Methodology and concept of design

7.2.1 Propagation of THz radiation

In general, an ideal intensity profile of Gaussian beam is assumed for the consideration of THz beam propagation. In order to consider the optic arrangement for a beam transfer, it is important to clearly understand the nature of Gaussian beam for the transport beamline design. The transverse profile of the Gaussian beam has to be defined to determine the characteristics of a THz beam. In this design, the intensity profile is estimated with $1/e^2$ half-width of about 87.5% of incident intensity [2], defined as

$$I = I_0 \exp\left(-\frac{2r^2}{w^2}\right) \tag{7.1}$$

where w is the half-width of the beam to the $1/e^2$ intensity point at some distance from the waist along the propagation axis, and r is the radial distance from the center of the beam.

However, the Gaussian beam profile does not keep its size constant as the beam propagates through free space on z-direction as shown in Fig. 7.2. Owing to radiation diffraction, a Gaussian beam will diverge transversely with angle θ from the beam waist (w_0). The initial beam waist radius referring to a minimum size of beam radius can be simply calculated by

$$w_0 = \frac{\lambda}{\pi\theta} \tag{7.2}$$

where λ is the radiation wavelength and θ is the beam divergence.

The calculation for the new beam waist radius of radiation propagation can be given by [3]

$$w_0' = w_0 f \sqrt{\frac{1}{(f-d)^2 + Z_R^2}} \tag{7.3}$$

where w_0 is the initail beam waist, f is the focal length of first focusing mirror (F1), d is the distance between beam waist and lens, Z_R is the rayleigh length $(\pi w_0^2/\lambda)$, and λ is the radiation wavelength. The distance from focusing optical component to new beam waist is given by

$$D = f + [(w_0'/w_0)^2 (d - f)] \tag{7.4}$$

The beam radius from the new beam waist of a Gaussian beam propagating in free space along z-axis is defined as

$$w(z) = w_0' \sqrt{\left[1 + \left(\frac{z}{Z_R'}\right)^2\right]} \tag{7.5}$$

where z is the distance between new beam waist and Z_R' is the rayleigh length of the new beam waist,$(\pi w_0'^2/\lambda)$.

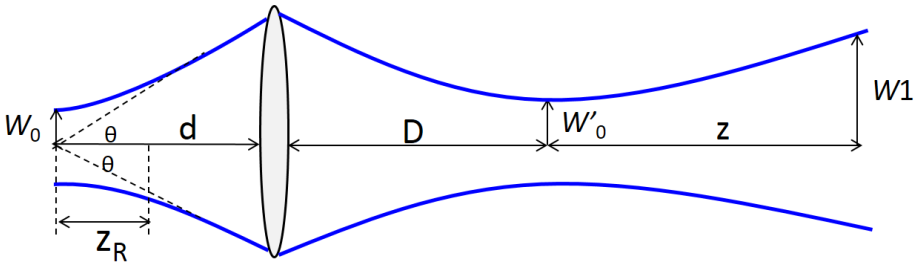

Figure 7.2: Schematic of Gaussian beam propagation in free space.

7.2.2 Design of the transport line of THz-CUR at Kyoto University

The main component for the transport beamline consists of several optical components including focusing mirrors and plane mirrors. To align and focus the THz beam, the focusing optical component such an off-axis parabolic mirror can be provided with reflective optics because the lenses made of any material would reflect and absorb some part of radiation. The THz beam can be guided to the direction as expected by using the plane mirror. Since the optical component of about 15 cm-diameter is available for commercial and easily for installation, this size will be properly used to collect the radiation intensity and guide THz radiation. Assuming the all-optical component working at the incident angle of 45˚, an aperture size should be about 12 cm-diameter for the actual size of about 15 cm-diameter. According to a Gaussian beam, the beam size is defined by $1/e^2$ half-width. Therefore, the beam diameter has to be kept less than 10 cm in the design for the aperture size of 12 cm.

(a) Measurement of spatial distribution for estimating of initial beam parameters

Regarding the design of the THz transport line using the concept of Gaussian beam propagation, we need to investigate the beam divergence used for estimating the beam size. THz radiation from a short electron bunch moving into a periodic magnetic field of undulator was reflected by Ti foil and it was transmitted through a THz window. The THz window of fused silica window has a transmittance of about 75%. The experimental setup to measure the beam profile for estimating beam divergence is illustrated in Fig. 7.3. This measurement was performed with a THz frequency of 0.16 THz. The beam profile was measured by using a pyroelectric detector with a sensitivity diameter of 1 mm (PYD-1/2, PHLUXi) and removing of the built-in lens. The detector position was scanned from −4 cm to 4 cm, with a step size of 0.5 cm. The positions for detector installation were 7.5 cm, 11 cm, 16 cm, and 21 cm from THz window.

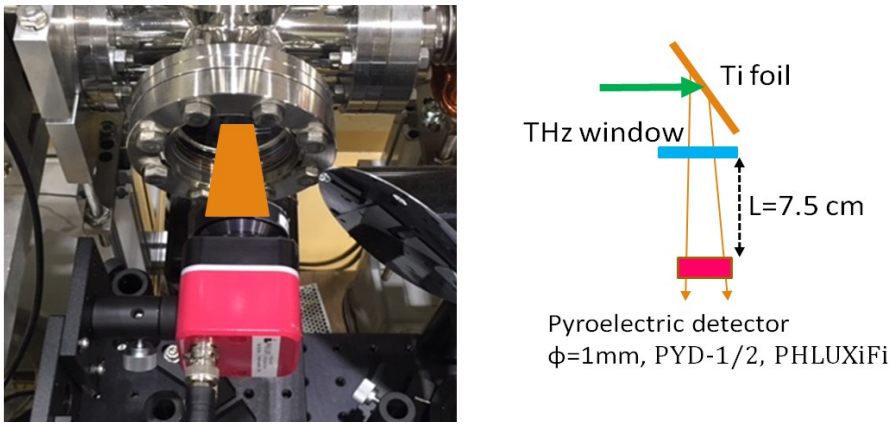

Figure 7.3: Experimental setup for measuring the beam profile.

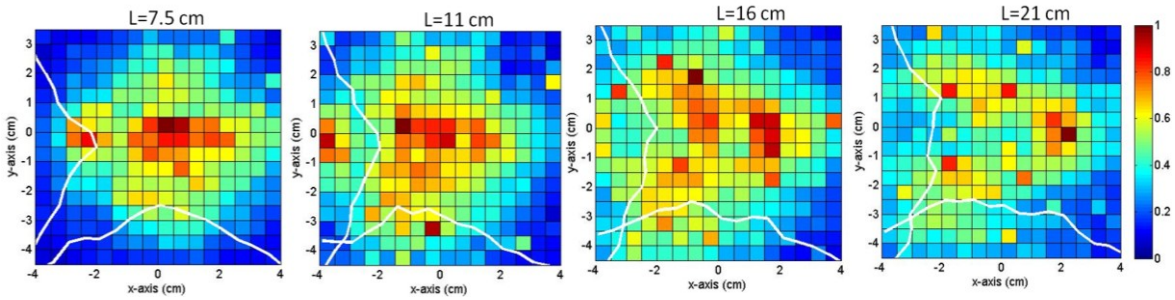

Figure 7.4: Beam profile at downstream THz window, the detector was installed at 7.5 cm, 11 cm, 16 cm, and 21 cm from THz window.

Figure 7.4 shows the dependence of the beam profile on the longitudinal distance from the THz window. From the beam profile result, it indicated that the beam size is wider as a considerable distance is far away from the source because the THz beam travels with beam divergence with making THz beam expansion. In order to estimate beam divergence, the beam profile can be fitted with Gaussian distribution to obtain beam size.

The dependence of beam diameter on the distance from the THz window is plotted in Fig. 7.5. It was found that the beam diameter of the $1/e^2$ point at the distance of 7.5 cm from the THz window is 9.75 cm and 6.36 cm for the horizontal and vertical axis, respectively. Initial beam parameters consisting of the beam waist and beam divergence can be calculated from the measured beam profile at different distance from THz window.

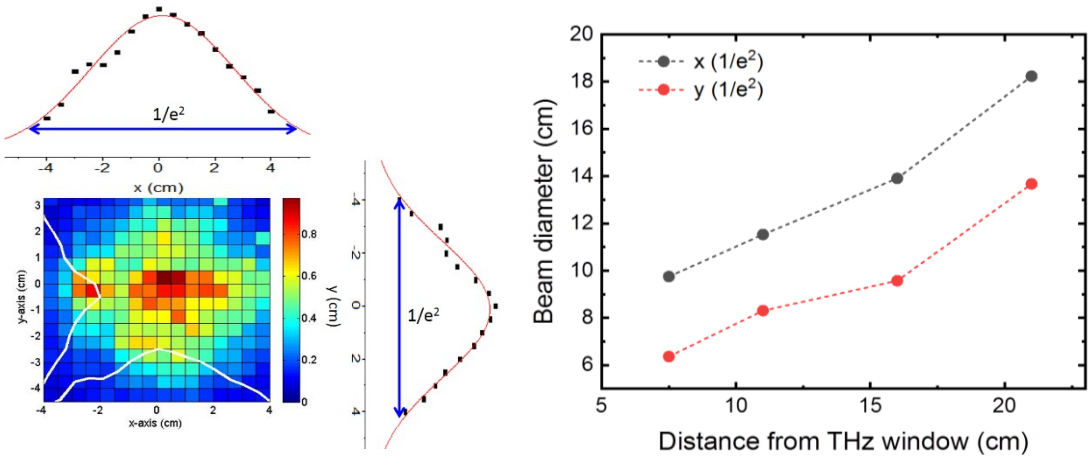

Figure 7.5: Beam diameter (2w) at different distance from THz window.

As a result, we can estimate the beam divergence generated from our source. The slope values from the linear fitting are 0.3442 and 0.2929 for the horizontal and vertical profile, respectively. It was found that the beam divergences were 0.2924 rad and 0.2439 rad for the horizontal and vertical axis, respectively. To simplify the calculation from the equation (7.2), the initial bean waists were 2.0 mm and 2.4 mm for horizontal and vertical directions, respectively. In the process of designing the transport line, we concentrate on the horizontal beam waist because of having larger beam divergence and stronger amount of diffraction.

(b) THz beam expansion

The beam size of THz beam traveling after THz window depends on the radiation wavelength. Therefore, the design has to be started considering the THz beam at the lowest frequency or the longest wavelength, which is where, has the largest diffraction effect. Size of the THz beam is easily expanded. However, the beam expansion along the beamline can be controlled with a suitable focal length of first focusing mirror (F1). Then, the beam divergence will be minimized afterward. The size of THz beam propagation can be estimated by using Equation (7.5) and it depends on focal length and distance from the beam waist. The specification of the F1 component for focusing the beam after THz window is very important for controlling the beam size expanding. The beam size on the surface of the first focusing mirror could be calculated from the beam divergence estimated from the measured beam profile. Under condition at a distance (d) from beam waist less than 200 mm, the beam diameter can be controlled less than 10 cm approximately as illustrated in Fig. 7.6. It is shown that at a distance of 200 mm the beam diameter is over 10 cm then an aperture size of

the optical component has to be larger than 15 cm, which cannot be acceptable. As a result, the distance of 150 mm would be a good candidate for installing the first focusing mirror.

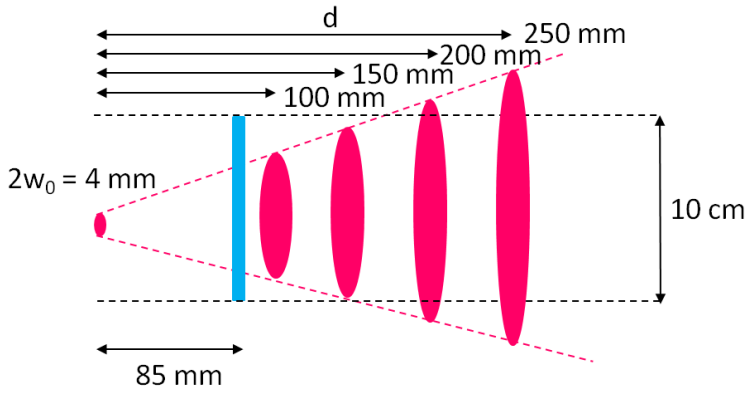

Figure 7.6: Beam diameter on surface of the first focusing mirror.

Figure 7.7(left) shows the beam diameter along a beamline at different the focal length of F1. In case of using two focusing mirrors for focusing the beam, the smallest diameter is 15 cm by using the 200 mm focal length of the 1st focusing mirror with *d*=200 mm from the beam waist. The aperture of focusing optical component has to be larger than 20 cm at least, assuming the focusing mirror working at an incidence angle of 45˚. It is difficult to find a commercially available value of optical components to respond to the requirement of the large size aperture. For the case of F1 = 100 mm, the beam is diverged so fast. Regarding the result, it can be seen that the suitable condition is to use the focusing component with the focal length F1 of 150 mm to obtain the beam diameter of 10 cm approximately.

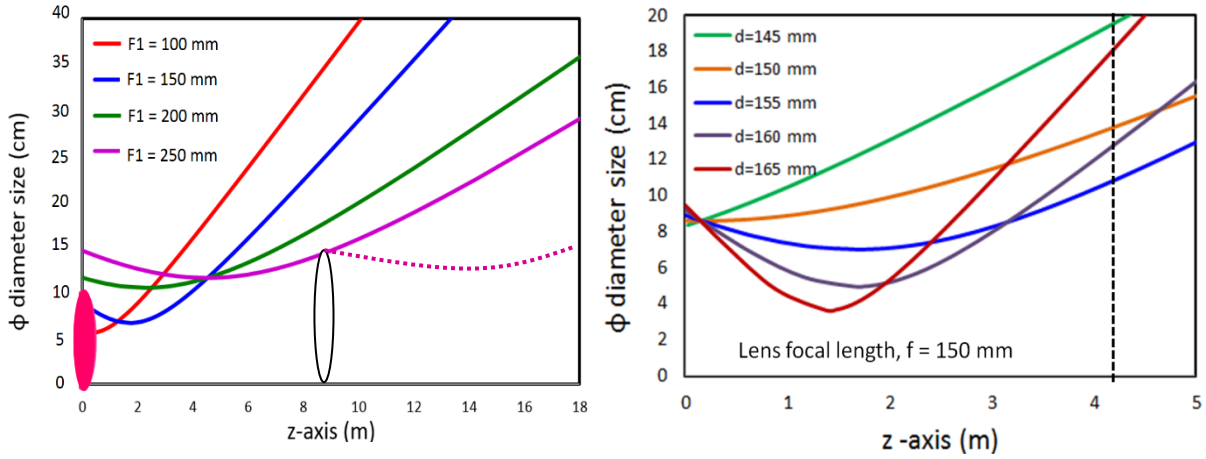

Figure 7.7: (left) Beam diameter along z-axis at frequency of 0.16 THz and (right) dependence of beam diameter on the distance from beam waist to lens with fixed focal length of 150 mm.

In order to control the beam diameter along the beamline, the important parameters are not only the focal length of focusing mirror but also the distance between the beam waist and the first focusing mirror. In Fig. 7.7(right), obviously, d = 155 mm is the best solution with the focal length of 150 mm compared to the use of the other distance. In order to obtain the beam diameter at the first focusing mirror surface about 10 cm, the optimal position of F1 should be located at the distance at 155 mm (about 70 mm from the THz window). The beam diameter is about 10 cm at a distance of 4.4 m, where is the location used to install the second focusing mirror. To be convenient for the user, the specifications of optical components and their locations installed in the transport line would be kept unchanged for the whole operating frequencies (the 0.16 – 0.65 THz frequency range). This would be achieved by using four focusing mirrors along the beamline with a total length of 18 meters approximately.

7.3 Results of beam diameter and intensity transmission ratio

Throughout the beamline, the four focusing mirrors were used to keep the beam diameter within 10 cm. Figure 7.8 shows the calculation of beam diameter along the beamline by using four focusing mirrors at 0.16 THz and 0.65 THz. The focal lengths of the focusing mirrors consist of 150 mm for the first one, and 2500 mm for other focusing mirrors. It was found that the beam diameter can be controlled less than 11 cm at both frequencies of 0.16 THz and 0.65 THz. Therefore, the specification of the focusing mirror used here would be reasonable to obtain our goal for transporting the beam to the user station.

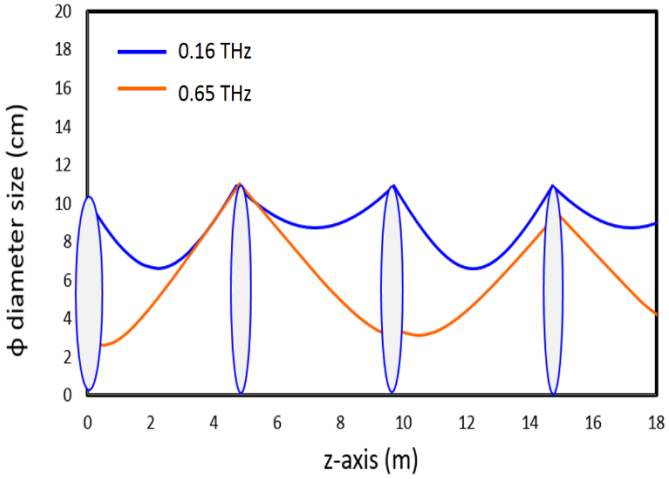

Figure 7.8: Beam diameter with the four focusing mirrors along the THz beamline for 0.16 THz and 0.65 THz.

The focusing mirrors such as off-axis parabolic mirrors were applied to align and focus the THz beam. Plane mirrors made of metals were used to reflect the THz beam. A sketch of the layout of the beamline performed from Zemax optical design program [4] is shown in Fig. 7.9 and the mirror parameters are summarized in Table 7.1. In order to guide beam crossing over the wall, which is the partition between the machine room and user hall, the beam has to be reflected up by using a plane mirror. The angle of the plane mirror can be adjusted freely depending on the direction of the beam. Then the beam was focused again by the parabolic mirror (F2). According to the result in Fig. 7.8, the proper location for the installation of F2 is far from F1 about 4.4 meters with the 2500 mm focal length of F2. The beam was reflected again by using the second mirror M2. To focus and align beam, parabolic mirrors F3 and F4 with the 2500 mm focal lengths were placed at downstream F2 mirror about 4.3 and 8.5 meters, respectively. Let the beam directly to the user station, the final plane mirror M4 is used. Figure 7.10 shows the beam diameter from the Zemax optical simulation. The result is in good agreement with the calculation one performed from Gaussian beam propagation.

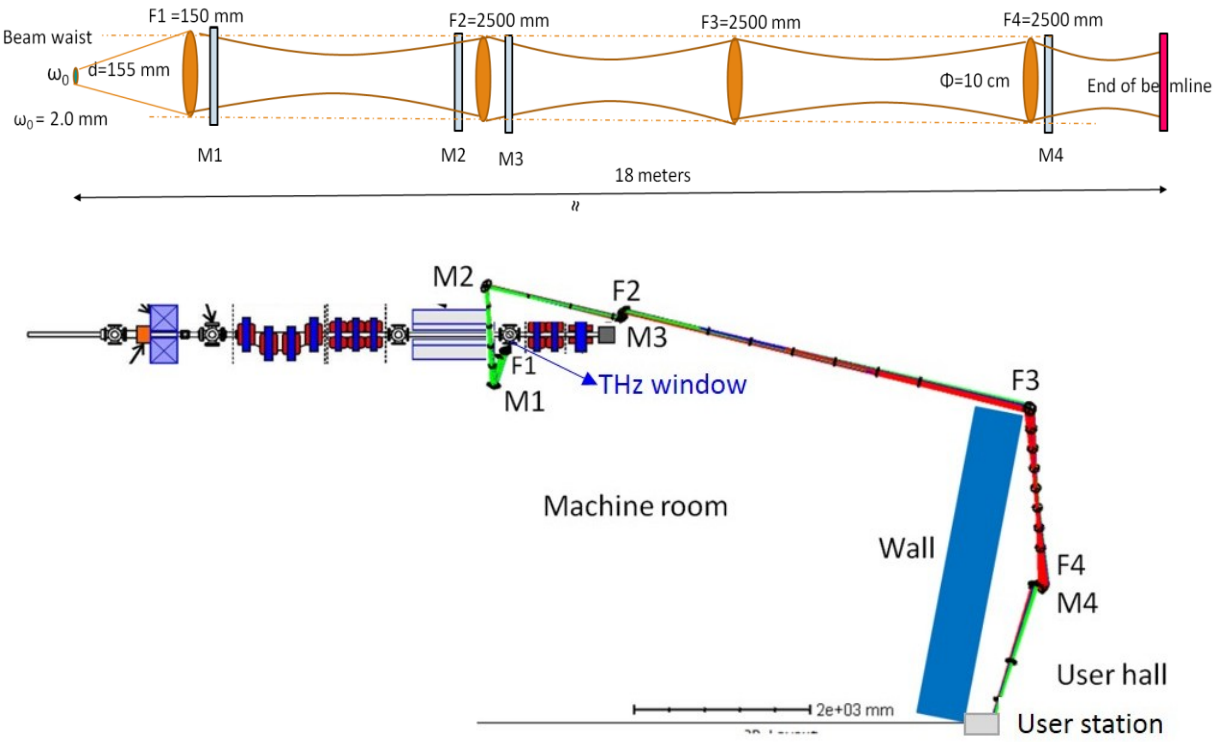

Figure 7.9: Layout of the transport line drawn from Zemax optical program.

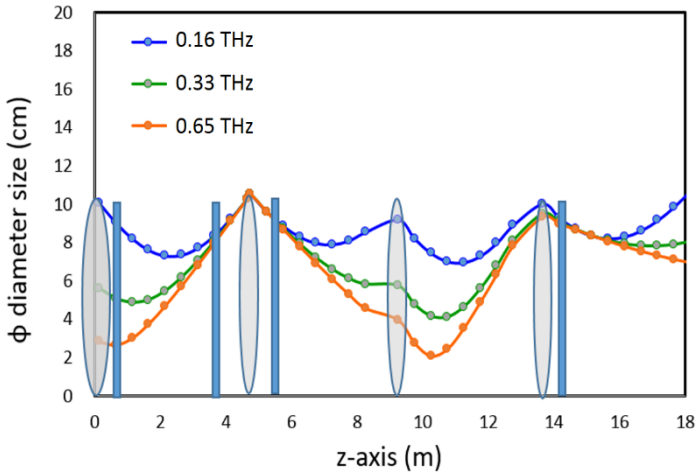

Figure 7.10: Beam diameter along the THz beamline for 0.16 THz, 0.33 THz and 0.65 THz.

Table 7.1: Mirror names, distance from the source, type and focal length for the THz transport beamline.

Mirror	Distance of beam waist (mm)	Mirror type	Focal length (mm)
F1	155 mm	Parabolic mirror	150 mm
M1	1155 mm	Plane mirror	-
M2	3155 mm	Plane mirror	-
F2	4655 mm	Parabolic mirror	2500 mm
M3	6655 mm	Plane mirror	-
F3	10655 mm	Parabolic mirror	2500 mm
F4	12655 mm	Parabolic mirror	2500 mm
M4	14655 mm	Plane mirror	-
Beginning of user station	18000 mm	-	-

The transport of the THz radiation with a minimal intensity loss requires the careful investigation with fixed the position, aperture size (or the surface size for collecting the radiation), and focal length of the optical components. The investigation of the THz intensity transmission ratio was carried out using the numerical simulation named THzTransport [5, 6], which is widely used for the calculation of the spot size and transmission of radiation to compute the propagation of THz radiation through the actual beamline. This code is based on the diffraction theory and calculates the complex electric field of the emitted light

propagating from the source. The aperture size of the optical components used in this calculation is 12 cm-diameter. Based on the design explained, the simulated results of the beam profile on the surface of each optical component are presented in Fig. 7.11. It was found that the beam size on a parabolic mirror F3 is larger than that on other components. The intensity of THz beam would lose when hitting on the surface of optical components because they could not cover the overall of THz beam size.

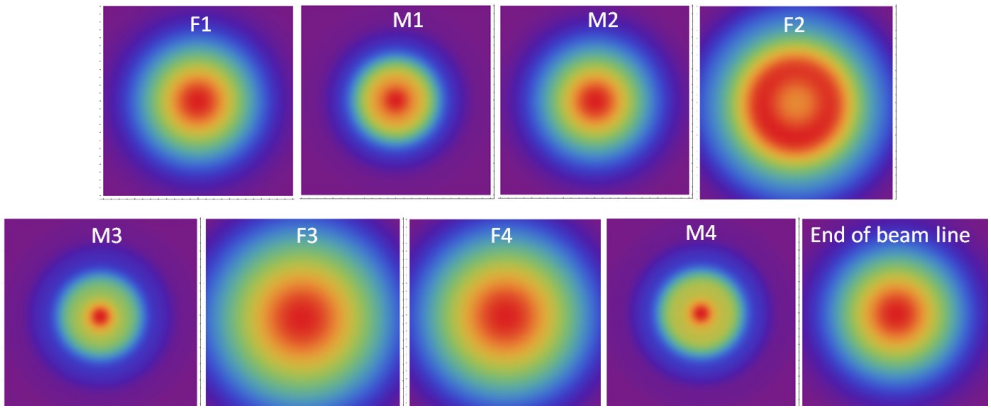

Figure 7.11: Simulated spots at 0.16 THz along the THz-CUR transport line. The aperture size is 12x12 cm.

Figure 7.12 shows the spot size dependence on the radiation frequency at the end of the beamline before traveling to the user station. The beam size of the THz beam is smaller at higher the radiation frequency. Analysis of beam diameter was done by using Gaussian fitting as plotted in Fig. 7.13(left). Figure 7.13(right) presents the beam diameter as a function of radiation frequency. The relation between the beam size and radiation frequency is in good agreement with the calculation. The beam diameter of the $1/e^2$ point of 0.16 THz can be controlled, and its diameter is about 10 cm. The beam diameter before going to user station is less than 6 cm at the frequency higher than 0.33 THz.

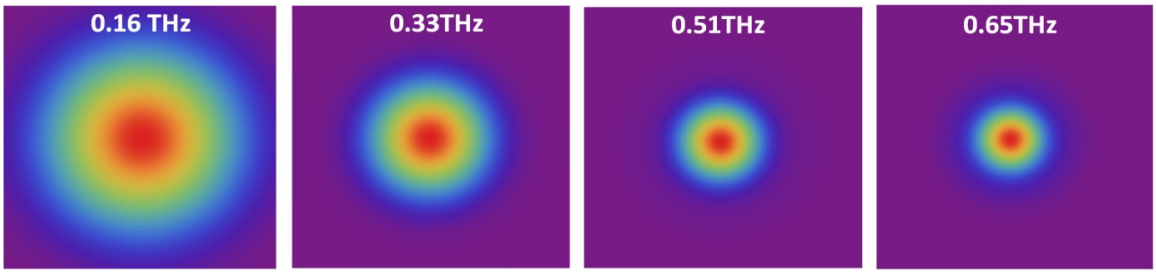

Figure 7.12: Simulated spots at 0.16, 0.33, 0.51, and 0.65 THz at the end of THz-CUR transport line (12x12 cm size of each square image).

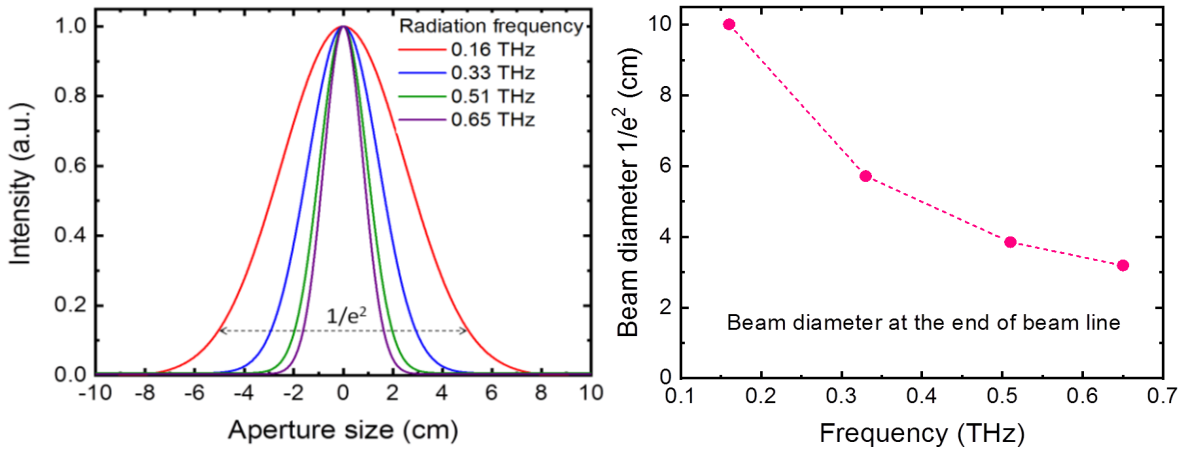

Figure 7.13: Gaussian beam at frequency of 0.16, 0.33, 0.51, and 0.65 THz at the end of THz-CUR transport line from THzTransport code (left) Gaussian beam distribution and (right) beam diameter.

In Table 7.2, we summarize the intensity transmission ratio at different frequencies including 0.16 THz, 0.33 THz, 0.51 THz, and 0.65 THz. The percent of intensity transmission was calculated by comparing with the radiation intensity at a position indicated the beam waist. At the end of the beamline or the beginning of user station, the intensity transmission ratio of radiation at 0.16 THz is about 35% and increases more than 80% in the frequency region higher than 0.33 THz under the condition of using four focusing mirrors with an aperture size of 12 cm-diameter. For radiation frequency at 0.16 THz, the intensity transmission ratio is only 35% on account of the finite aperture sizes of optical component to collect THz radiation during propagating to the user station.

Table 7.2: THz intensity transmission ratio at the beginning of user station (18 meters from THz window) performed from THzTransport code.

Radiation frequency (THz)	THz intensity transmission ratio (%)
0.16 THz	35%
0.33 THz	85%
0.51 THz	> 90%
0.65 THz	> 90%

7.4 Increase of intensity transmission ratio

The intensity transmission ratio of radiation at 0.16 THz can be transmitted only 35% due to the large diffraction. The major cause of the decrease of the transmission is due to the finite sizes of the optical components. The greatest loss of the intensity occurs at the F3 component because the largest size appears on the surface of the optic component as presented in Fig. 7.11. In order to avoid the loss and to increase of THz intensity transmission ratio, the rearrangement of optical component is necessary. In order to collect the THz radiation with higher transmission ratio at 0.16 THz, there are two options to obtain higher efficiency of the transport line. The first one is to increase the aperture size of the optical components from 12 cm to 15 cm. If aperture size of all-optical components is larger than 15 cm-diameter, the transmission raises up to about 70% when passing through all optical components. However, the large size of optical components may be not available for commercial because the actual size of components may be larger than 20 cm-diameter and it is difficult for construction and alignment.

Another way is to add one more the focusing mirror to focus beam size with keeping an aperture size of 12 cm. The good condition of the optical component arrangement is to employ five focusing mirrors and three plane mirrors for controlling and guiding the THz beam to the user station. Figure 7.14 shows the beam diameter along transport beamline for THz radiation at 0.16 THz and 0.65 THz. The focal lengths of 2^{nd}, 3^{rd}, 4^{th}, and 5^{th} focusing mirrors are 1800 mm. Figure 7.15 presents the comparison of the percentage of intensity transmittance at different frequencies between using four focusing mirrors and five focusing mirrors. Since the beam diameter of the frequency of 0.16 THz can be controlled less than 9 cm approximately with five focusing components, the intensity can be transferred with the percentage of transmission higher than 60% under the condition with the aperture size of optical components of 12 cm-diameter. The scheme of optical design presented here allows controlling the THz radiation in low frequency less than 10 cm-diameter and also providing THz radiation with the high transmission ratio.

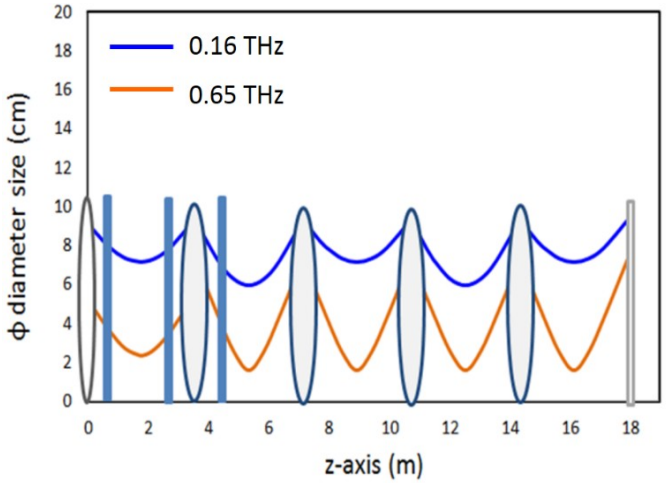

Figure 7.14: Beam diameter for 0.16 THz and 0.65 THz along the THz beamline with the five focusing mirrors.

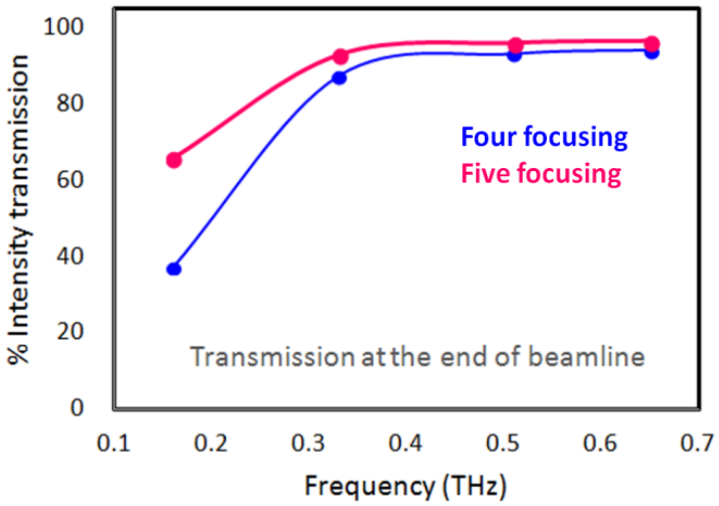

Figure 7.15: Intensity transmission ratio of THz beam at the beginning of user station compared between the case of using four focusing components and five focusing components with aperture size of 12 cm.

7.5 Conclusions

This study reveals the possibility in the transportation of the radiation propagation with high transmission ratio over the total length of 18 meters. The details of the calculation and optical component arrangement presented here allow achieving high transmission ratio. The intensity transmission ratio from the THz window to user station was about 60% at the frequency of 0.16 THz and more than 90% for the frequency higher than 0.33 THz. Using the optical design of THz-CUR transport line presented here, the THz radiation with a peak

power in ten kW-class, and tunable frequency range of 0.16 - 0.65 THz can propagate to the user station. It will be as a potential technique for the design of transport beamline for propagating radiation in the low-frequency region. Further, the transport beamline consisting of a set of the plane and focusing mirrors will be constructed to serve to THz radiation, which has great potential in the study of the vibration and rotation of the molecule for materials science.

7.6 References

[1] A. Rogalski and F. Sizov, "Terahertz detectors and focal plane arrays", *Opto-Electron. Rev.* **19**(3), pp. 346–404 (2011).

[2] E. J. Galvez, "Gaussian Beams", Department of Physics and Astronomy Colgate University (2014). Available online: https://www.colgate.edu/media/5371/download.

[3] Y. Kyohei, *et al*., "Optimization of the new designed FEL beam transport line", *Zero-Carbon Energy Kyoto*, pp 205-216 (2012).

[4] Radiant ZEMAX, Zemax 13, Optical Design Program, User's Manual (2014). ZEMAX Development Corporation, http://www.zemax.com.

[5] "Terahertz Transport code", http://www. desy.de/~schmidtb/THz-Transport.

[6] S. Casalbuoni, *et al.*, "Ultrabroadband terahertz source and beamline based on coherent transition radiation", *Phys. Rev. Spec. Top. Accel. Beams* **12**, 030705 (2009).

Chapter 8

Conclusions

8.1 Summary

Properties of THz-CUR and the impact on the enhancement of THz-CUR power

In this thesis, the investigations of the properties of THz-CUR including the total radiation energy, spatial distribution, and power spectrum were proposed. Also, the effects of degradation of electron beam quality on the generation of THz radiation were studied and discussed.

- The total radiation energy of THz-CUR in the micropulse with a bunch charge of 160 pC was about 1 μJ (～20 kW peak power) at 0.16 THz and gradually reduced at higher frequency region.
- The frequency of THz-CUR from a bunch charge of 60 pC was tuned between 0.16 and 0.65 THz by changing the magnetic field of the undulator. When increasing the bunch charge to 160 pC, the radiation power spectrum at a frequency of 0.65 THz could not be observed.
- Based on the results presented above, we can find the limitations of the generation of THz-CUR from our source due to the influence of the space-charge forces in a high charge region.

- When increasing the bunch charge, the bunch lengthening occured and the electron beam qualities were degraded.
- The qualities of electron beam have a significant influence on the THz radiation generation
- Using a high-quality electron beam with the parameters of σ_z < 0.2 ps-FWHM, $\delta\gamma/\gamma$ < 0.5% and ε < 0.5 mm-mrad, the peak power with 160 pC bunch charge would be increased to more than 100 kW at a radiation frequency of 0.16 THz.

The manipulation of transverse and longitudinal laser distributions

Since our source has been developed as a compact accelerator with a low beam energy of 4.6 MeV, an electron bunch is easily disturbed by the influence of the space-charge force. A potential way to mitigate the space-charge effect in a short electron bunch for THz-CUR source at Kyoto University is presented. The laser pulse distribution used in the cathode illumination has been manipulated both in transverse and longitudinal directions. The study enabled to improve the source performance for providing the higher power of THz radiation.

- Simulation performed by GPT code
  - The longitudinal phase space without space-charge effect at the entrance of the chicane seemed to be linear and it had a high chirp of energy–time. The electron bunch can be compressed to reach a higher peak current and short bunch length after passing through a chicane magnet.
  - To reduce the nonlinear space-charge force, and decrease the charge density, the longitudinal phase space provides a suitable energy chirp for bunch compression to obtain shorter electron bunch by using the truncated-Gaussian profile and enlarging the laser pulse width.
  - The optimum aperture size to make truncated-Gaussian was the radius of 0.5 mm for laser radius of 0.5 mm-rms in the Gaussian distribution.
  - With keeping the charge constant at 160 pC using the transverse profile of truncated-Gaussian, the simulated bunch length can be compressed to 1.45 ps-FWHM.
  - By expanding the laser pulse width from 5.8 ps-FWHM to 10 ps-FWHM, the electron bunch was compressed to 0.82 ps-FWHM and shorter than 0.5 ps-FWHM with using the laser pulse width of 20 ps-FWHM.
  - According to the increase of bunch form factor, the generated radiation power of the CUR at 0.16 THz with 160 pC bunch charge was expected to rise up to 127% using

truncated-Gaussian profiled and more than 300% by enlarging the laser pulse width larger than 10 ps-FWHM.

- Measurements
  - The experimental setups for the manipulation of the transverse and longitudinal laser distribution were set up in order to mitigate the space-charge effect.
  - The examinations of the transverse truncated-Gaussian distribution as well as the enlargement of the laser pulse width to generate the higher radiated power of THz-CUR, were performed experimentally.
  - The transverse laser profile was modified and changed from Gaussian to the truncated-Gaussian distribution by clipping the drive laser with an aperture before irradiating the cathode.
  - Due to the bunch charge fluctuation, the aperture size of 0.75 mm-radius was efficient more than 0.5 mm-radius in this situation.
  - The longitudinal laser distribution was shaped to a flat-top and enlarged the pulse width to 10 ps-FWHM and 20 ps-FWHM by using a single stage and double stages of laser pulse stacking (LPS), respectively.
  - Although the use of 20 ps-FWHM of flat-top laser distribution, the bunch form factor was higher than that using 10 ps-FWHM, the other electron beam properties such as energy spread and emittance got worse in quality.
  - At the bunch charge of 80 pC, the bunch length was compressed shorter than 1 ps-FWHM using truncated-Gaussian profile with 10 ps-FWHM laser pulse width.
  - With the laser pulse of 10 ps flat-top, the radiation energy using truncated-Gaussian laser profile increased by 70%, compared to Gaussian distribution at the same bunch charge of 80 pC.
  - The total radiation intensity with using 10 ps-FWHM laser pulse was higher than that with 20 ps-FWHM under the condition at the bunch charge of 80 pC. However, the result indicated that the saturation of total radiation intensity disappeared in the bunch charge region of lower than 115 pC.
  - The use of a truncated-Gaussian laser profile with a laser pulse width of 10 ps-FWHM would be a good candidate for preventing the trouble of space-charge and RF effects on the generation of THz radiation.

The optical design of the transport beamline to the user station

This study revealed the possibility in the transportation of the radiation over long distance and in obtaining the high transmission ratio to the user station.

- In the low-frequency region below 1 THz, the radiation easily diverges due to a large amount of diffraction.
- The beam divergences at 0.16 THz were about 0.29 rad and 0.24 rad in horizontal and vertical planes, respectively, estimated from the beam profile after THz window.
- The beam sizes in horizontal and vertical planes were about 10 cm and 6 cm-diameter ($1/e^2$ half-width), respectively at a distance of 7.5 cm from the THz window.
- The optical design of THz-CUR transport beamline using five focusing mirrors can be used to collect and control the radiation size with 10 cm-diameter along the distance of 18 meters from the THz window to user station.
- Using the optical design reported here, the THz-CUR intensity would be transmitted more than 60% at a frequency of 0.16 THz and more than 90% for the frequency higher than 0.33 THz.

8.2 Recommendations and suggestions for future development of THz-CUR system

- With the laser shape under the condition of truncated-Gaussian profile and 10 ps-FWHM pulse width, the preliminary results of electron beam properties and THz radiation were observed in the region of bunch charge lower than 100 pC. The properties of electron beam and THz radiation at the bunch charge higher than 100 pC are necessary to be examined for the next step of improvement.
- Since General Particle Tracer (GPT) version 3.10 used in this study includes only a space-charge model but without wakefields and Coherent Synchrotron Radiation (CSR) effects, the use of the other numerical simulation including the CSR effect is recommended.
- The optical components to guide the THz radiation to user station will be constructed, and the remote controller for the undulator gap adjustment is needed to be installed.
- Since the optimization of beam optics in real measurement is complicated and takes a long time to obtain a good condition, the automatic online algorithm such as Robust Conjugate Direction Search (RCDS) algorithm [*X. Huang, et al., Nucl. Instrum. Methods Phys. Res 86 (2013)*] is necessary to be studied and used for the actual machine operation.
- Regarding the increase in the power of THz radiation after successfully mitigating the space-charge effect, the THz source including a seed light is attractive to amplify THz radiation power. A THz-wave parametric generator such as an adopted parametric generator is required to produce the seed light.

8.3 Lists of Journals and publications

Journals with peer reviewed publication

1. S. Krainara, *et al*., "Study of the saturation of radiation energy caused by the space charge effect in a compact THz coherent radiation source", *J. Phys.: Conf. Ser.* **1067**, 032022, (2018).
2. S. Krainara, *et al*., "Manipulation of laser distribution to mitigate the space-charge effect for improving the performance of a THz Coherent Undulator Radiation source", *Particles* **1**(1), pp. 238-252 (2018**)**.
3. S. Krainara, *et al.*, "Properties of THz Coherent Undulator Radiation (THz-CUR) at Kyoto University", *Review of scientific instruments,* Status: Publish after revisions (2019).

Award

1. Best oral presentation award of "Achieved Excellent Results" in the 14th Japan Atomic Energy Society Kansai (14 回若手研究者による研究発表会), OSTEC, Osaka, Japan (31 August 2018).

Proceeding publications

1. S. Krainara, *et al*., "Observation of THz radiation from THz Coherent Undulator Radiation Source", in *Proc.* of AESJ annual meeting, Hokkaido, Japan (2017).
2. S. Krainara, *et al*., "THz coherent undulator radiation generated from compact accelerator based on photocathode RF gun", in *Proc.* of PASJ Conf., WEOM02, (2017).
3. S. Krainara, *et al*., "Development of compact THz coherent undulator radiation source at Kyoto University", in *Proc.* of FEL conf., USA, MOP049, pp. 0-3, (2017).
4. S. Krainara, *et al.,* "Study on space charge effect in a compact THz Coherent Undulator Radiation (THz-CUR) source at Kyoto University", in *Proc.* of AESJ annual meeting, Osaka, Japan (2018).
5. S. Krainara, *et al*., "Study of the saturation of radiation energy caused by the space charge effect in a compact THz coherent radiation source", in *Proc.* of IPAC conf., THPMF074, (2018).
6. S. Krainara, *et al*., "Mitigation of the space charge effect for improving the performance of THz-CUR source", in *Proc.* of PASJ Conf., WEP007, (2018).

Oral presentations

1. S. Krainara, *et al*., “Study of Undulator Characteristics for generating THz Radiation at Kyoto University”, FEL and RF-GUN workshops, Sendai, Japan (February 2017).
2. S. Krainara, *et al*., “THz coherent undulator radiation generated from compact accelerator based on photocathode RF gun”, PASJ’17, Hokkaido, Japan (Auguest 2017).
3. S. Krainara, *et al*., “Observation of THz radiation from THz Coherent Undulator Radiation Source”, AESJ annual meeting, Hokkaido, Japan (September 2017).
4. S. Krainara, *et al*., “Investigation of the performance of THz-CUR Source at Kyoto University”, Workshop on CSR and Free Electron Lasers from Ultra Short Bunch Electron Beam, Sendai, Japan (September 2017).
5. S. Krainara, *et al*., “Development of Compact THz Coherent Undulator Radiation Source at Kyoto University”, Workshop on Generation and Application of High Brightness Quantum Beam, Uji, Japan (2017).
6. S. Krainara, *et al.,* “Study on space charge effect in a compact THz Coherent Undulator Radiation (THz-CUR) source at Kyoto University”, AESJ annual meeting, Osaka, Japan (January 2018).
7. S. Krainara, *et al*., “Study on space charge effect in a compact THz Coherent Undulator Radiation (THz-CUR) source at Kyoto University”, FEL workshop, Uji, Japan (February 2018).
8. S. Krainara, *et al*., “Effect of space charge in short electron bunch on THz Coherent Undulator Radiation at Kyoto University”, Workshop on CSR and Free Electron Lasers from Ultra Short Bunch Electron Beam, Hefei, China (March 2018).
9. S. Krainara, *et al*., “Mitigation of the space charge effect for improving the performance of THz-CUR source”, Workshop on CSR and Free Electron Lasers from Ultra Short Bunch Electron Beam, Uji, (30 August 2018).
10. S. Krainara, *et al*., “Mitigation of the space charge effect for improving the performance of THz-CUR source”, in the 14th Japan Atomic Energy Society Kansai (第１４回若手研究者による研究発表会), Osaka, Japan (31 August 2018).
11. S. Krainara, *et al*., “Impact of the photocathode excitation laser distribution on the generation of THz Coherent Undulator Radiation at Kyoto University”, 第 25 回 FEL と

High-Power Radiation 研究会, Spring8, Japan (14-15 February 2019).

Poster presentations

1. S. Krainara, *et al*., “Development of compact THz coherent undulator radiation source at Kyoto University”, in *Proc.* of FEL conf., Santa Fe, USA, (25-31 August 2017).
2. S. Krainara, *et al*., “Improving efficiency of THz coherent radiation generated from a compact linac system at Kyoto University, in *Proc.* of EMSES’18, Uji Japan, (1-4 April 2018).
3. S. Krainara, *et al*., “Study of the saturation of radiation energy caused by the space charge effect in a compact THz coherent radiation source”, in *Proc.* of IPAC conf., Vancouver, Canada, THPMF074, (1-5 May 2018).
4. S. Krainara, *et al*., “Mitigation of the space charge effect for improving the performance of THz-CUR source", in *Proc.* of PASJ Conf., WEP007, Nagaoka, japan (1-5 August 2018).
5. S. Krainara, *et al*., “Electron beam optimization of THz Coherent Undulator Radiation source at Kyoto University”, Beam Physics workshop, Tokyo, (21-23 November 2018).
6. S. Krainara, *et al*., “Impact of the transverse and longitudinal distributions of the photocathode excitation laser distribution on the generation of THz Coherent Undulator Radiation at Kyoto University”, in *Proc.* of PASJ Conf., FRPI021, Kyoto, Japan (31 July-3 August 2019).